Instituut voor
Kern- en Stralingsfysica
Departement Natuurkunde en Sterrenkunde
Faculteit Wetenschappen

KATHOLIEKE UNIVERSITEIT
LEUVEN

From ^{27}Mg to ^{33}Mg: transition to the Island of inversion

Promotor:
Prof. Dr. G. Neyens

Proefschrift ingediend tot het behalen van de graad van doctor in de wetenschappen door

Deyan Todorov Yordanov

2007

Contents

List of Tables

List of Figures

Chapter 1

Introduction

Every atomic nucleus is associated with a unique set of macroscopic properties: mass, angular momentum, excitation energies, electromagnetic moments, etc. Studies of these observables led to discoveries of global phenomena, such as the zero angular momentum of even-even nuclei or the increase in binding energy per nucleon at certain, " magic ", numbers of protons and neutrons. In a phenomenological sense this implies that the nuclei have intrinsic structure, which is something that the early models, like the liquid drop model, could not account for. The modern theories consider the nucleus as a many-boby quantum system, providing insights into the *nuclear structure* through studying macroscopic observables - nuclear moments in particular. A phenomenological approach to the problems in nuclear physics is an alternative to a complete fundamental theory as well as its natural precursor. It is the better understanding of the nuclear structure in neutron rich Magnesium (Mg) isotopes, that is the main objective of this doctoral dissertation.

1.1 Physics motivation

The nuclear shell model has been successful in reproducing the magic numbers as well as predicting spins of odd-mass nuclei, especially in the light and intermediate mass regions. However, properties of nuclei with $150 < A < 190$ or $A > 230$ are not correctly described by the spherical shell model, since in these regions collective phenomena associated with nuclear shapes departing from spherical take place. The Nilsson model [1] is dealing with the problem of single-particle motion in a deformed potential. Many odd-mass nuclei are properly described by coupling the odd-particle motion to the rotations of a deformed core [2]. A natural question is: " does deformation play a role in light nuclear systems? ". A positive answer has been acquired with the early

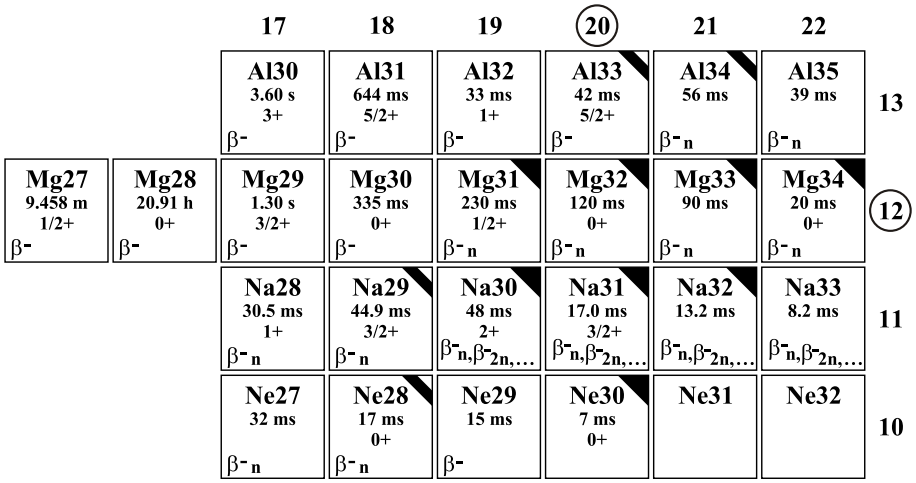

Figure 1.1: Nuclear chart in the region of the Island of inversion.
Experimental evidence for pure intruder ground states are indicated with blackened corners. Mixed wave functions are noted with a black strip. Unmarked boxes indicate a lack of conclusive experimental data or belonging outside the island. The results from the present work concerning ^{27,29,31,33}Mg are taken into account.

investigation of the stable ^{19}F, ^{20}Ne, ^{23}Na and ^{24}Mg. It has been shown that the deficiency of both protons and neutrons in a major shell is causing strong α-type correlations, resulting in well-defined prolate deformations, for instance ^{20}Ne and ^{24}Mg in the *sd* shell [2] (vol. 2, p. 99). When one or both types of particles are filling to the middle or the end of a major shell there is a competition between prolate and oblate shapes [3], as it is in the cases of the stable ^{28}Si, ^{32}S and ^{36}Ar. Advances in technology in the last two decades made available many exotic nuclear species, enabling studies of systems with a filled neutron *sd* shell, while maintaining the proton *sd* shell almost unoccupied. The mass measurements of ^{31,32}Na [4] indeed showed an increase in their binding energies, unexpected within the frame of the *sd* shell model. Constrained Hartree-Fock calculations [5] reproduced these irregularities by allowing neutron promotion from the $\nu\, 1d_{3/2}$ orbit to the $\nu\, 1f_{7/2}$ orbit, which resulted in prolate deformations in these two isotopes. The ground-state spin of ^{31}Na [6] was another parameter incompatible with theoretical predictions, which gave reasons to discuss a " collapse of the conventional shell-model ordering in the very neutron-rich isotopes " [7]. The necessity of taking into account the $\nu\, 1f_{7/2}$ [8] and the $\nu\, 2p_{3/2}$ [9] orbitals, which are being populated before the *sd* shell is full, indicated the disappearance of the $N = 20$ shell closure and gave rise to

the expression *Island of inversion*. Two mechanisms have been justified to play an important role in the inversion of the "normal" $0\,\hbar\omega$ (0p-0h) and *intruder* $n\,\hbar\omega$ (np-nh) states [3]: (i) A reduction of the shell gap; (ii) An increase in the neutron-neutron and proton-neutron interactions; The diminishing predictive power of the nuclear models in the island have stimulated extensive experimental studies, providing inputs for the theoretical modeling of the region. It was originally thought that the Island of inversion initiates with the $N = 20$ isotones of Ne, Na and Mg and extends up to $N = 22$ or beyond. However, experimental studies determined that $^{28}\mathrm{Ne}_{18}$ [10, 11], $^{29}\mathrm{Na}_{18}$ [12–14] and $^{31}\mathrm{Mg}_{19}$ [15, 16] mark the beginning of the island. The maximum Z borderline also needs to be modified, since g-factor measurements [17, 18] detected a considerable amount of intruder components into the ground-state wave functions of ^{33,34}Al. The available experimental facts are summarized in Fig. 1.1. The collectivity of the even-even ^{32,34}Mg is presently well established [19–24], whereas the nuclear structure of the odd-mass ^{33}Mg is rather unknown. A β-decay study [25] suggests a 1p-1h configuration with spin and parity $I^\pi = 3/2^+$ in contrast to $I^\pi = 5/2^+$ (1p-1h) from intermediate energy Coulomb excitation [26] and proton inelastic scattering [27] experiments. The systematics of the region, on the other hand, is evident for 2p-2h ground states [10, 22, 24, 28, 29]. Due to the close competition between different particle-hole excitations, only experimental studies can reveal the true ground-state configuration of ^{33}Mg.

1.2 This work

Measurements of nuclear moments are highly beneficial for studies of the nuclear structure, since these are extremely sensitive to the composition of the nuclear wave function. The establishment of the nuclear spin and magnetic moment of ^{31}Mg indicates the disappearance of the $N = 20$ shell closure for Mg, extends the Island of inversion to $N = 19$ and provides evidence for a nuclear deformation. These findings are essential for the development of the shell model in the vicinity of the island. The results on ^{31}Mg are published in Ref. [15, 30, 31], the full texts of which are included at the end of this dissertation. While the first paper is focused on the interpretation of the result in terms of large-scale shell-model calculations, the latter two concentrate on the experimental technique, describing the apparatus and the reference measurements on ^{8}Li. A comprehensive discussion on the establishment of the sign of the magnetic moment is given in Ref. [30]. This discussion further extends on studying the nature of the low-lying excited states. Preparatory work for the measurements on ^{31}Mg is described in Ref. [31], namely the studies of the experimental β asymmetry in different hosts (Au, Pt and MgO) and as a function of the laser intensity. The latter paper concentrates on the atomic physics, more specifically on understanding the relative intensities of the hy-

perfine structure components. The present thesis presents additional studies of ^{31}Mg. The physics case is discussed in terms of nuclear-structure evolution over the Mg chain and transition to the Island of inversion. The magnetic moments of ^{29,31}Mg [15, 16, 30, 31] are reevaluated. The optical transition strengths and the process of optical pumping for Mg II are understood, based on the pioneering work described in Ref. [12]. Computer codes simulating optical and β-asymmetry spectra are published for the first time (open source).

The main objective of this dissertation is to unambiguously determine the ground-state spin and magnetic moment of ^{33}Mg by means of laser spectroscopy in combination with nuclear magnetic resonance. Large-scale shell-model calculations are outlined and used to draw conclusions through a comparison with the experimental results. An alternative interpretation of former experimental studies is given within the frame of the Nilsson and particle plus rotor models. Additional research is done in order to understand the generated NMR lineshapes with modulation. The essence of the present studies on ^{33}Mg is summarized in a preliminary version of a publication [32], the full text of which is included at the end of this thesis.

The hyperfine parameters of the stable ^{25}Mg II in the D_1 and D_2 lines are obtained by means of fluorescence spectroscopy. The magnetic moment of ^{27}Mg and an estimate of the quadrupole moment of ^{29}Mg, extracted from the hyperfine structure of their singly-ionized atoms, are reported for the first time. The case of ^{27}Mg is also a central topic in a publication in preparation [33].

Chapter 2

Measurement of nuclear moments and radii

2.1 Electromagnetic moments

The electromagnetic moments are defined by the general expression:

$$\mathscr{M}_{\lambda\mu=0} = \langle I, M = I | \sum_{k=1}^{A} \hat{T}_{\lambda\mu=0}(k) | I, M = I \rangle, \tag{2.1}$$

where $\hat{T}_{\lambda\mu}$ is a one-body tensor operator of rank λ, describing the interaction of the nucleus with an external electromagnetic field. It stands for either $\hat{Q}_{\lambda\mu}$ when giving rise to the electric moments associated with the static charge distribution, or $\hat{M}_{\lambda\mu}$ when giving rise the magnetic moments associated with the charge currents. The multipole operators $\hat{Q}_{\lambda\mu}$ and $\hat{M}_{\lambda\mu}$ can be expressed with the spherical harmonics $Y_{\lambda\mu}(\theta, \phi)$ [34] (p. 583). Their parities are $(-)^{\lambda}$ and $(-)^{\lambda+1}$, thus requiring λ-even for the static moments and λ-odd for the magnetic moments due to the parity conservation. For spherical tensor operators the M-state dependence of the matrix elements reduces to a dependence on the Clebsch-Gordan[A] or $3j$ coefficient via the Wigner-Eckart theorem:

$$\langle IM | \hat{T}_{\lambda\mu} | IM \rangle = (-1)^{I-M} \begin{pmatrix} I & \lambda & I \\ -M & \mu & M \end{pmatrix} \langle I || \hat{T}_{\lambda} || I \rangle, \tag{2.2}$$

where $\langle I || \hat{T}_{\lambda} || I \rangle$ is the reduced matrix element. According to the properties of the $3j$ coefficients, $\mu = 0$ and λ must satisfy the triangle condition $\Delta(II\lambda)$

[A] The relation between the Clebsch-Gordan and the $3j$ coefficients (A.14), together with their numerical implementation, is given in Appendix A.4.

(A.6), where I is the nuclear spin. The maximum value of λ is therefore $\lambda_{\max} = 2I$. The only moment for $I = 0$ is the *electric monopole moment* $\sum_{k=1}^{A} e_k$ ($\lambda = 0$), which represents the total charge of the nucleus. The *magnetic dipole moment* ($\lambda = 1$) is defined for $I \geq 1/2$ and the *electric quadrupole moment* ($\lambda = 2$) for $I \geq 1$.

The *magnetic dipole moment* operator for a single nucleon in a static binding field is:

$$\boldsymbol{\mu} = \mu_N \left(g_l^{t_z} \boldsymbol{l} + g_s^{t_z} \boldsymbol{s} \right) / \hbar, \tag{2.3}$$

where $g_l^{t_z}$ and $g_s^{t_z}$ are the orbital and spin gyromagnetic ratios of the nucleon in terms of nuclear magnetons $\mu_N = e\hbar/2m_p = 5.05078317(20) \times 10^{-27}$ J/T [35]. The index t_z represents the isospin of the particle, $t_z(p) = -1/2$ for protons (π) and $t_z(n) = 1/2$ for neutrons (ν). Since the nuclear magneton is defined with e and m_p, the proton charge and rest mass, the orbital g factors become:

$$g_l^{\pi} = 1\,, \qquad\qquad g_l^{\nu} = 0\,. \tag{2.4}$$

The latest experimental proton and neutron g factors, taken from Ref. [35], are:

$$g_s^{\pi} = 5.585694675(57)\,, \qquad\qquad g_s^{\nu} = -3.82608545(90)\,. \tag{2.5}$$

The fact that g_s of the uncharged neutron is different from zero and that of the proton is far from two, the expectation value from the Dirac equation for a point particle with spin 1/2, is an indication that they are not elementary point particles but have an internal structure. The observable magnetic moment of a single nucleon in a shell-model orbit is the expectation value of the magnetic moment operator (2.3) in the state with maximum projection of angular momentum, as defined in (2.1). According to the projection theorem [36] (p. 7):

$$\langle jj|\boldsymbol{\mu}|jj\rangle = \frac{\langle jj|\boldsymbol{\mu}\cdot\boldsymbol{j}|jj\rangle}{\langle jj\,|\boldsymbol{j}^2|\,jj\rangle}\langle jj|\boldsymbol{j}|jj\rangle \tag{2.6}$$

the components of the vector $\boldsymbol{\mu}$ perpendicular to $\boldsymbol{j}$ average out. Thus, the projection on the third axis is $\langle jj|\hat{\mu}_z|jj\rangle = \langle jj|\boldsymbol{\mu}\cdot\boldsymbol{j}|jj\rangle\langle jj|\boldsymbol{j}_z|jj\rangle/\langle jj|\boldsymbol{j}^2|jj\rangle$. Since $\langle jj|\boldsymbol{j}_z|jj\rangle = j\,\hbar$, $\langle jj|\boldsymbol{j}^2|jj\rangle = j(j{+}1)\hbar^2$ and using the squaring of $\boldsymbol{j} = \boldsymbol{l}{+}\boldsymbol{s}$ to express the product operators one finds:

$$\langle jj|\boldsymbol{\mu}\cdot\boldsymbol{j}|jj\rangle = \mu_N \left\langle jj \,\middle|\, g_l^{t_z}\boldsymbol{j}^2 + \left(g_s^{t_z} - g_l^{t_z}\right)\left(\boldsymbol{j}^2 - \boldsymbol{l}^2 + \boldsymbol{s}^2\right)/2 \,\middle|\, jj\right\rangle / \hbar\,.$$

It is now straightforward to evaluate the single-particle magnetic moments:

$$\mu = j\left(g_l^{t_z} \pm \frac{g_s^{t_z} - g_l^{t_z}}{2l+1}\right)\mu_N,\ j = l \pm \frac{1}{2}. \tag{2.7}$$

The latter are also known as the *Schmidt values*. In the extreme shell-model picture the ground states of odd-mass nuclei are considered to be determined mainly by the odd particle, which alone gives rise to the nuclear magnetic moment. Comparison with experiments shows that the Schmidt values are generally larger in magnitude. One explanation for this could be that g_s for a bound nucleon is different than the free-nucleon value. A common approach is to consider *effective g factors* derived by fitting to experimental data in the precise region of interest. In general $g_s^{t_z}{}_{\text{effective}} \approx 0.7\, g_s^{t_z}{}_{\text{free}}$ yields reasonable results. The nuclear gyromagnetic ratio of a state with an angular momentum $\boldsymbol{I}$ is defined with:

$$\langle \boldsymbol{\mu}_I \rangle = g_I \, \boldsymbol{I} \, \mu_N / \hbar \quad \Rightarrow \quad \mu_I = g_I \, I \, \mu_N \, . \tag{2.8}$$

The *electric quadrupole moment* operator of a point particle is defined as:

$$e\, Q_{zz} = e^{t_z} e \left(3z^2 - r^2\right) = e^{t_z} e \sqrt{\frac{16\pi}{5}} r^2 Y_{20}(\boldsymbol{r}) \, , \tag{2.9}$$

where e^{t_z} is the charge of the carrier, a proton (π) or a neutron (ν), in units e. This definition is based on the third diagonal component of the tensor: $\hat{Q}_{ij} = q(3r_i r_j - r^2 \delta_{ij})$, known from the Classical Electrodynamics. For a free nucleon it is expected to have $e^\pi = g_l^\pi = 1$ and $e^\nu = g_l^\nu = 0$. Experimental quadrupole moments of nuclei with an odd neutron are indeed smaller than those with an odd proton, but are definitely different from zero. One can account for such effects by introducing proton and neutron *effective charges*, denoted here with e^{t_z}. The operator defined with (2.9) does not include the elementary charge e and therefore has the dimension of a surface[A]. All quadrupole moments in this thesis will be given in units b (barn[B]). The single-particle quadrupole moments are given with the expression:

$$eQ = \langle jj | e\, Q_{zz} | jj \rangle = \mp \frac{2j-1}{2j+1} \left\langle r^2 \right\rangle e^{t_z} e \, , \tag{2.10}$$

where $\langle r^2 \rangle$ is the mean-square radius of the nucleon. A derivation can be followed for instance in Ref. [37–39]. The sign corresponds to a particle ($-$) or a hole ($+$). The more general expression:

$$\langle jm | e\, Q_{zz} | jm \rangle = \pm \frac{j(j+1) - 3m^2}{2j(j+1)} \left\langle r^2 \right\rangle e^{t_z} e \, , \tag{2.11}$$

can be obtained with the use of (2.2). By summing (2.11) over all m states[C] one

[A] The quantity Q defined with (2.9) still contains the same information on the nuclear structure as the quadrupole moment eQ, namely the geometrical distribution of the charge. In order to avoid the inclusion of e in the value of eQ the elementary charge is embedded in the units (e mb or e fm^2). By doing so the actual values become identical: $Q(\text{mb}) = eQ(\text{e mb})$ or $Q(\text{fm}^2) = eQ(\text{e fm}^2)$.

[B] 1b $= 10^{-28}$m^2. Commonly used are mb or fm^2 (1mb $= 10^{-31}$m^2, 1fm^2 $= 10^{-30}$m^2).

[C] Use the relation $\sum_{m=-j}^{j} m^2 = j(j+1)(2j+1)/3$.

finds that the total quadrupole moment of a full orbit vanishes. Furthermore, since a pair of nucleons couple to a zero angular momentum they have no preferential orientation in space in which case their wavefunction has a spherical symmetry $|\psi(\boldsymbol{r})|^2 = |\psi(r)|^2$. Hence the expectation values of the coordinates are one third of the mean-square radius $\langle x^2\rangle = \langle y^2\rangle = \langle z^2\rangle = \langle r^2\rangle/3$ in which case the quadrupole moment (2.9) vanishes.

2.2 Nuclear deformations

The observation of very large quadrupole moments, far from the single-particle estimates, is attributed to collective phenomena resulting in deformation of the nuclear core. In the case of quadrupole deformations ($\lambda = 2$) the nuclear shape is parametrized with:

$$R_{\substack{k\\k=1,\,2,\,3}} = R_0 \left[1 + \sqrt{\frac{5}{4\pi}}\,\beta\,\cos\!\left(\gamma - \frac{2k\pi}{3}\right)\right], \tag{2.12}$$

where β and γ are the Hill-Wheeler coordinates [40]. The parameter β determines the quadrupole deformation and γ the deviation from axial symmetry. In the axially symmetric case ($\gamma = 0 \Leftrightarrow R_1 = R_2 = R_\perp$) the following relation exists:

$$\frac{R_3 - R_\perp}{R_0} = \frac{3\beta}{4}\sqrt{\frac{5}{\pi}}\,. \tag{2.13}$$

The quadrupole moment[A] in the reference frame of the nucleus is given by:

$$Q_0 = \frac{4}{3}\Big\langle \sum_{k=1}^{Z} r_k^2 \Big\rangle \delta\,, \tag{2.14}$$

where δ is the *distortion parameter*, which for a uniformly charged spheroidal nucleus with a sharp surface is given by:

$$\delta = \frac{3}{2}\frac{R_3^2 - R_\perp^2}{R_3^2 + 2R_\perp^2} \approx \frac{\Delta R}{R} + \frac{1}{6}\left(\frac{\Delta R}{R}\right)^2 + \dots\,, \tag{2.15}$$

with $\Delta R = R_3 - R_\perp$ and $R \approx R_0$. Equations (2.12) and (2.14), (2.15) are justified in Ref. [34] (p. 7) and Ref. [2] (vol. 2, p. 47), respectively. Using (2.13), (2.14) and (2.15) one finds a relation, between the intrinsic quadrupole moment and the deformation, based on the shape (2.12) with axial symmetry:

$$Q_0 = Z\,\langle r^2\rangle\,\beta\sqrt{\frac{5}{\pi}}\left(1 + \frac{\beta}{8}\sqrt{\frac{5}{\pi}}\right), \tag{2.16}$$

[A] Attention must be paid since "quadrupole moment" is used for either Q or eQ.

where the second radial moment is related to the mass number as:

$$\langle r^2 \rangle = \frac{3}{5}\left(1.12A^{1/3}\right)^2\left(1 + 3.84A^{-2/3} + \dots\right) \approx \frac{3}{5}\left(1.2A^{1/3}\right)^2 \,(\mathrm{fm}^2)\,, \qquad (2.17)$$

according to Ref. [2] (vol. 1, p. 161).

Extensive studies in the regions of deformation reveal that the low-energy states in odd-A nuclei, despite the complexity of the spectra, can be classified as a number of rotational bands characterized by an intrinsic angular momentum[A] K and a parity π. A typical example is the case of ^{25}Mg. A summary of the experimental data and an interpretation, as well as references to the original work can be found in Ref. [2] (vol. 2, p. 284). The band with $K^\pi = 1/2^+$, based on the Nilsson $1/2\,[200]$ orbital, is of a particular interest, since the ground state of ^{31}Mg was found to be $1/2^+$ [15], based on the same orbital, hence making it a candidate for one of the low-lying states observed in ^{33}Mg [20, 25]. The energy levels of a rotational band in an odd-A nucleus with a strong deformation (*strong coupling limit*) are described by:

$$E_K(I) = E_K^0 + \frac{\hbar^2}{2\mathscr{I}}\left[I(I+1) + a\,(-1)^{I+1/2}(I+1/2)\delta_{K,1/2}\right]\,, \qquad (2.18)$$

where $\mathscr{I}$ is the moment of inertia, E_K^0 is the bandhead and a is the decoupling parameter associated with the odd particle. The explicit form of a is given in Ref. [34] (p. 112). A table with calculated a values for different orbitals in $sd-pf$ nuclei at a prolate deformation $\beta = 0.4$ can be found in Ref. [2] (vol. 2, p. 290). The magnetic dipole moment of an odd-A nucleus has two contributions, g_R representing the gyromagnetic ratio of the rotor ($\boldsymbol{\mu_R} = g_R\,\boldsymbol{R}\,\mu_N$) and g_K, rising from the single-particle motion:

$$\mu = g_R I + (g_K - g_R)\frac{K^2}{I+1}\,. \qquad (2.19)$$

This equation is valid only for bands with $K \neq 1/2$. In the case of $K = 1/2$ one must use:

$$\mu = g_R I + \frac{g_K - g_R}{4(I+1)}\left[1 + b\,(2I+1)(-1)^{I+1/2}\right]\,, \qquad (2.20)$$

where b is the *magnetic decoupling parameter*[B]. The reduced transition probabilities for magnetic dipole radiation, can be obtained from Ref. [2] (vol. 2, p. 56, 57). In the strong coupling limit the projection Ω of the total momentum of the odd nucleon on the symmetry axis equals the projection K of the total

[A] The angular momenta quantum numbers are referred to as *angular momenta*. The Planck's constant $\hbar$ in such sentences is implicit.

[B] The parameters a and b are related: $(g_K - g_R)\,b = -(g_l - g_R)\,a - (-1)^l(g_s + g_K - 2g_l)/2$ [see Ref. [2] (vol. 2, p. 303)].

angular momentum I ($\Omega = K$). The single-particle g factor can be calculated as:

$$g_K = \frac{1}{K}\langle K|\hat{\mu}_3|K\rangle \,, \tag{2.21}$$

where $\hat{\mu}_3 = \mu_N(g_l^{t_z}\boldsymbol{l}_3 + g_s^{t_z}\boldsymbol{s}_3)$ is the magnetic moment operator in the body-fixed frame and $|K\rangle$ are the Nilsson wave functions. The g factor of a solid rotor is approximately equal to the density of protons $g_R \approx Z/A$ [2] (vol. 2, p. 54). The observable or spectroscopic quadrupole moment and the intrinsic quadrupole moment (2.14) are related as:

$$Q = \langle IK20|IK\rangle\langle II20|II\rangle\, Q_0 = \frac{3K^2 - I(I+1)}{(I+1)(2I+3)}\, Q_0 \,. \tag{2.22}$$

Knowledge on the deformation of even-even nuclei, ^{30,32,34}Mg being of a particular interest in this thesis, can be obtained through the reduced transition probabilities, either from Coulomb excitation cross sections, or from lifetime measurements:

$$\begin{aligned} B(E2; KI_i \to KI_f) &= \frac{1}{2I_i+1}\,|\langle KI_f||\mathscr{M}(E2)||KI_i\rangle|^2 \\ &= \frac{5}{16\pi}\, e^2 Q_0^2\, \langle I_i K20|I_f K\rangle^2 \,, \end{aligned} \tag{2.23}$$

where I_i and I_f are the initial and the final angular momenta and the operator $\mathscr{M}(E2) = \int \rho(\boldsymbol{r})\, r^2\, Y_{20}(\boldsymbol{r})\, d\tau$ is the general form of (2.9) with $\rho(\boldsymbol{r})$ representing the charge density. The treatment leading to (2.22) and (2.23) can be followed in Ref. [2] (vol. 2, p. 45). The Clebsch-Gordan coefficients involved can be calculated with the tools given in Appendix A.4.

2.3 Atomic hyperfine structure

The *hyperfine structure* (HFS) observed in atomic spectra results from the interaction of the nuclear multipole moments with the charge and current distributions associated with the moments of the electron environment. The Hamiltonian in the most general form is:

$$H_{\mathrm{HFS}} = H(M1) + H(E2) + \ldots \tag{2.24}$$

The hyperfine interaction couples the angular momenta of the nucleus and the electrons $\boldsymbol{I}$ and $\boldsymbol{J}$, being no longer integrals of motion, to the total angular momentum operator $\boldsymbol{F} = \boldsymbol{I} + \boldsymbol{J}$. Thus the quantum number F is used to describe the quantum states $|JIFM_F\rangle$. F satisfies the triangle condition (A.6)

and therefore the number of states in a hyperfine multiplet is $2I+1$ for $J > I$ and $2J+1$ for $I > J$. The magnetic dipole term in (2.24) is:

$$H(M1) = -\langle \boldsymbol{\mu}_I \rangle \cdot \langle \boldsymbol{B}_J \rangle = A \, \frac{\boldsymbol{I} \cdot \boldsymbol{J}}{\hbar^2} \,, \tag{2.25}$$

where $\langle \boldsymbol{\mu}_I \rangle$ is given by (2.8) and $\boldsymbol{B}_J$ is the magnetic field, associated with the total magnetic moment of the electrons $\boldsymbol{\mu}_J$:

$$\langle \boldsymbol{\mu}_J \rangle = -g_J \, \boldsymbol{J} \, \mu_B / \hbar \quad \Rightarrow \quad \mu_J = -g_J \, J \, \mu_B \,. \tag{2.26}$$

The Bohr magneton is defined as $\mu_B = e\hbar/2m_e = 927.400899(37) \times 10^{-26}$ J/T [35] and g_J is given by the Landé formula:

$$\begin{aligned} g_J = g_L \, \frac{J(J+1) + L(L+1) - S(S+1)}{2J(J+1)} \\ + g_S \, \frac{J(J+1) - L(L+1) + S(S+1)}{2J(J+1)} \,. \end{aligned} \tag{2.27}$$

The g factors $g_L = 1$ and $g_S = 2.0023193043617(15)$ [41] are associated with the magnetic moments of the orbital and spin motions of the electrons

$$\boldsymbol{\mu}_L = -g_L \, \boldsymbol{L} \, \mu_B / \hbar \,, \qquad\qquad \boldsymbol{\mu}_S = -g_S \, \boldsymbol{S} \, \mu_B / \hbar \,, \tag{2.28}$$

the coupling of which gives rise to the atomic *fine structure* (FS). One can write:

$$\langle \boldsymbol{B}_J \rangle = -\langle B(0) \rangle \, \boldsymbol{J} / \hbar J \,, \tag{2.29}$$

where $\langle B(0) \rangle$ is a scalar quantity representing the average flux density of the magnetic field at the nucleus. For a single electron or an electron outside a closed shell (alkali-like atoms) the general direction of $\boldsymbol{\mu}_J$, and so the one of $\boldsymbol{B}_J$ at the nucleus, is antiparallel to the angular momentum $\boldsymbol{J}$, as can be concluded from (2.26) and (2.27). Thus in alkali-like atoms $\langle B(0) \rangle > 0$. Calculated values of $\langle B(0) \rangle$ due to the alkalies valence electrons are presented in Ref. [42] (p. 132). The energy levels depend on the product $\boldsymbol{I} \cdot \boldsymbol{J}$, which can be expressed as a function of $\boldsymbol{J}^2$, $\boldsymbol{I}^2$ and $\boldsymbol{F}^2$ by squaring $\boldsymbol{F} = \boldsymbol{I} + \boldsymbol{J}$. Using (2.8) and (2.29) the *magnetic dipole hyperfine parameter* becomes:

$$A = \frac{g_I \, \mu_N \, \langle B(0) \rangle}{J} \,. \tag{2.30}$$

A formal expression for the term $H(E2)$ in (2.24) is given by (2.55). However, a more complex treatment is required in order to extract the contribution of the quadrupole interaction to the atomic energies. A detailed description can

be followed in Refs. [42, 43]. The energy levels of the hyperfine structure, according to Ref. [42] (p. 15), are given with:

$$\begin{aligned} E_F &= E_J + A\,\frac{\xi}{2} + B\,\frac{3\xi(\xi+1) - 4I(I+1)J(J+1)}{8I(2I-1)J(2J-1)}\,, \\ \xi &= F(F+1) - I(I+1) - J(J+1)\,, \end{aligned} \tag{2.31}$$

where E_J represents the energy of the fine-structure level. The parameter B, called the *electric quadrupole hyperfine parameter*, has the form:

$$B = e\,Q\,\langle V_{JJ}(0)\rangle\,, \tag{2.32}$$

where $e\,Q$ is the nuclear spectroscopic quadrupole moment and $\langle V_{JJ}(0)\rangle$ is the average field gradient at the nucleus induced by the electrons, having a cylindrical symmetry about the $\boldsymbol{J}$ axis [43] (p. 13). The quadrupole hyperfine parameter B, and therefore the second term in (2.31), vanishes for either $J = 1/2$ or $I = 1/2$. If one neglects the volume changes along an isotopic chain one can approximate that the average magnetic field $\langle B(0)\rangle$ and electric field gradient $\langle V_{JJ}(0)\rangle$ are identical for all the atoms in the chain. Thus using (2.30) and (2.32) for two isotopes one arrives with:

$$A_1/A_2 = g_1/g_2\,, \tag{2.33}$$

$$B_1/B_2 = Q_1/Q_2\,. \tag{2.34}$$

The above equations are used for extraction of nuclear moments through atomic spectroscopy. However, these have as important application if used in the opposite direction. Measurements of nuclear moments with other techniques allow the determination of A and B. Equation (2.33) is, in this respect, essential for the extraction of nuclear spins from the hyperfine structure, as demonstrated in Section 5.3.

While the atomic hyperfine structure originates from the interaction of the nucleus with the natural electromagnetic field associated with the charge and current distributions of the atomic electrons, many experimental techniques require the employment of external fields. It is important for measurements based on the hyperfine structure to understand the influence of these fields. The Hamiltonian (2.25) in the presence of an applied magnetic field $\boldsymbol{B}_0$ takes the form:

$$H(M1) = A\,\frac{\boldsymbol{I}\cdot\boldsymbol{J}}{\hbar^2} - \langle\boldsymbol{\mu}_I\rangle\cdot\boldsymbol{B}_0 - \langle\boldsymbol{\mu}_J\rangle\cdot\boldsymbol{B}_0\,, \tag{2.35}$$

where $\langle\boldsymbol{\mu}_I\rangle$ and $\langle\boldsymbol{\mu}_J\rangle$ are the magnetic moments given with (2.8) and (2.26), respectively. The effect on the energy levels is referred to as the *Zeeman effect*. In the case with $\mu_J\,B_0 \ll A$ the magnetic components of the F states ($M_F = -F\,,\ -F+1\,,\ \ldots\,,\ F-1\,,\ F$) obtain different energies proportional to the external field:

$$E_{M_F} = E_F + g_F\,\mu_B\,B_0\,M_F\,. \tag{2.36}$$

The corresponding g factor in analogy with (2.27) is given with the expression:

$$\begin{aligned} g_F = g_J \, \frac{F(F+1) + J(J+1) - I(I+1)}{2F(F+1)} \\ - g_I \, \frac{\mu_N}{\mu_B} \, \frac{F(F+1) - J(J+1) + I(I+1)}{2F(F+1)} \, . \end{aligned} \tag{2.37}$$

The second term describing the nuclear contribution is often neglected due to the factor $\mu_N/\mu_B = m_e/m_p = 5.446170232(12) \times 10^{-4}$ [35]. In a strong magnetic field $\boldsymbol{I}$ and $\boldsymbol{J}$ are decoupled and the proper description of the states is no longer given by F and M_F, but by I, M_I, J and M_J:

$$E_{M_I \, M_J} = A \, M_I \, M_J + g_J \, \mu_B \, B_0 \, M_J - g_I \, \mu_N \, B_0 \, M_I \, . \tag{2.38}$$

The Zeeman effect in this limit is called the *Paschen-Back effect*. At intermediate fields the energy levels follow the rule that two states never cross if they have the same magnetic number M, where $M = M_F$ for low fields and $M = M_I + M_J$ for high fields. A detailed treatment of the Zeeman effect for all fields can be found for instance in Ref. [42] (p. 19-27).

The selection rules for dipole transitions between hyperfine-structure components of two different multiplets, rising directly from the triangle condition (A.6), are:

$$\Delta F = 0 \, , \, \pm 1 \, ; \qquad F + F' \geq 1 \, . \tag{2.39}$$

Electric-dipole radiation within the same multiplet is forbidden by the parity selection rule.

2.4 Isotope shifts and charge radii

The *isotope shift* is defined as the difference between the fine-structure splitting of two isotopes of the same element:

$$\delta\nu_i^{AA'} = \nu_i^A - \nu_i^{A'} \, . \tag{2.40}$$

The index i denotes the atomic transition, for instance $i : 3^2S_{1/2} \rightarrow 3^2P_{3/2}$. The short spectroscopic notation $n^{2S+1}L_J$ is being used throughout this thesis. A and A' in (2.40) are the mass numbers of the two isotopes. The isotope shift has two contributions:

$$\delta\nu_i^{AA'} = \delta\nu_{i\,,\,\mathrm{MS}}^{AA'} + \delta\nu_{i\,,\,\mathrm{FS}}^{AA'} \, , \tag{2.41}$$

where $\delta\nu_{i\,,\,\mathrm{MS}}^{AA'}$ represents the mass shift (MS), rising from the motion of the nucleus in the center of mass system, and $\delta\nu_{i\,,\,\mathrm{FS}}^{AA'}$ stands for the field shift (FS), corresponding to changes in the nuclear volume and shape and therefore

influencing the Coulomb attraction. The field effect is largest in transitions involving s electrons since their density at the nucleus is the highest. In the center of mass system the total momentum is:

$$\boldsymbol{P} + \sum_k \boldsymbol{p}_k = 0\,, \tag{2.42}$$

where $\boldsymbol{P}$ and $\boldsymbol{p}_k$ are the momenta of the nucleus and the electrons, respectively. The total kinetic energy is given by:

$$\begin{aligned} E_K &= \frac{\boldsymbol{P}^2}{2M} + \sum_k \frac{\boldsymbol{p}_k^2}{2m_e} \\ &= \sum_k \frac{\boldsymbol{p}_k^2}{2M} + \sum_{k\neq l} \frac{\boldsymbol{p}_k \cdot \boldsymbol{p}_l}{2M} + \sum_k \frac{\boldsymbol{p}_k^2}{2m_e}\,. \end{aligned} \tag{2.43}$$

Since the nuclear mass M is much larger than the mass of the electrons, in a first approximation the nucleus can be considered as stationary and later account for its motion by perturbation theory [43]. With this approach, changes of M do not influence the electron momenta $\boldsymbol{p}_k$. According to the *virial theorem* the average total energy of an atom equals the average kinetic energy with the opposite sign: $\langle E\rangle = -\langle E_K\rangle$. The mass shift with the use of (2.43), becomes:

$$\delta\nu_{i,\,\mathrm{MS}}^{AA'} = \frac{1}{2h}\,\frac{M-M'}{MM'}\left[\left\langle \sum_k \boldsymbol{p}_k^2 \right\rangle_i + \left\langle \sum_{k\neq l} \boldsymbol{p}_k \cdot \boldsymbol{p}_l \right\rangle_i\right]. \tag{2.44}$$

The first and the second term in (2.44) are called *normal mass shift* (NMS) and *specific mass shift* (SMS):

$$\delta\nu_{i,\,\mathrm{MS}}^{AA'} = \delta\nu_{i,\,\mathrm{NMS}}^{AA'} + \delta\nu_{i,\,\mathrm{SMS}}^{AA'}\,. \tag{2.45}$$

The transition $h\nu_i$ for a nucleus with an infinite mass, with the aid of (2.43), becomes $h\nu_i = \left\langle \sum_k \boldsymbol{p}_k^2 \right\rangle_i / 2m_e$. Making this substitution in (2.44) and approximating the nuclear with the atomic masses $M = M_A$ and $M' = M_{A'}$ one finds the normal mass shift:

$$\delta\nu_{i,\,\mathrm{NMS}}^{AA'} = \nu_i\, m_e\, \frac{M_A - M_{A'}}{M_A\, M_{A'}}\,. \tag{2.46}$$

This formula is usually rearranged in order to use the dimensionless atomic masses[A]:

$$\delta\nu_{i,\,\mathrm{NMS}}^{AA'} = \nu_i\, \frac{m_e}{u}\, \frac{m_A - m_{A'}}{m_A\, m_{A'}}\,, \tag{2.47}$$

[A] $m_A = M_A/u$, $u = 1.66053873(13) \times 10^{-27}$ kg [35].

where u is the *unified atomic mass*. Correlations between the electrons, contributing in the second term in (2.44), need a more sophisticated approach. A detailed description can be found in Refs. [42, 44]. The field shift is given by:

$$\delta\nu_{i,\,\mathrm{FS}}^{AA'} = F_i \left(\delta \left\langle r^2 \right\rangle^{AA'} + \frac{c_2}{c_1}\, \delta \left\langle r^4 \right\rangle^{AA'} + \frac{c_3}{c_1}\, \delta \left\langle r^6 \right\rangle^{AA'} + \ \ldots \right) , \tag{2.48}$$

with the convention that $\delta\langle r^n\rangle^{AA'} = \langle r^n\rangle^{A} - \langle r^n\rangle^{A'}$ and the radial moments:

$$\langle r^n \rangle = \frac{\int \rho(r)\, r^n d\tau}{\int \rho(r)\, d\tau} , \tag{2.49}$$

as described in Ref. [45]. The quantity F_i in (2.48) is the *electronic factor*, which is proportional to the change of the electronic charge density at the nucleus for the transition of interest i, $\rho(r)$ represents the nuclear charge distribution density and $\langle r^2\rangle$ is called the *mean-square charge radius*, giving the largest contribution to the field shift in (2.48). For most applications the isotope shift (2.40) is written as:

$$\delta\nu_i^{AA'} = K_i\, \frac{m_A - m_{A'}}{m_A\, m_{A'}} + F_i\, \delta \left\langle r^2 \right\rangle^{AA'} , \tag{2.50}$$

where K_i is the *total mass-shift coefficient*. Note that the quantities m_A and $m_{A'}$ are dimensionless and therefore K_i has the dimension of a frequency[A]. The linear dependence $\delta\nu_i^{AA'}\big(\delta\langle r^2\rangle^{AA'}\big)$ (2.50) allows the determination of mean-square charge radii through isotope shift measurements. The coefficients K_i and F_i must be obtained, either from reference measurements on at least three isotopes with known mean-square charge radii, or based on theory or other experimental data. A common approach to improve the precision of K_i and F_i is to perform measurements on the reference isotopes in two transitions i and j, for instance $i : 3^2S_{1/2} \rightarrow 3^2P_{1/2}$ and $j : 3^2S_{1/2} \rightarrow 3^2P_{3/2}$. Then by writing (2.50) for both and rearranging in the form:

$$\underbrace{\frac{m_A\, m_{A'}}{m_A - m_{A'}}\, \delta\nu_i^{AA'}}_{Y} = \underbrace{\frac{F_i}{F_j}}_{a}\, \underbrace{\frac{m_A\, m_{A'}}{m_A - m_{A'}}\, \delta\nu_j^{AA'}}_{X} + \underbrace{K_i - K_j\, \frac{F_i}{F_j}}_{b} , \tag{2.51}$$

one obtains additional conditions $a = F_i/F_j$ and $b = K_i - aK_j$, being used to reduce the errors of K_i and F_i. Plots of data according to (2.50) and (2.51) are known as *King plots*. More information can be found in Refs. [44, 45].

[A] If the atomic masses $M_A = m_A\, u$ are used in (2.50) instead of m_A, K_i acquires the dimension $\mathrm{s}^{-1}\mathrm{kg}$, in which case it is usually quoted in units $\mathrm{s}^{-1}\mathrm{u}$, such that the actual value remains the same.

2.5 Nuclear magnetic resonance

The concept of the *nuclear spin* $\boldsymbol{I}$ rests on the fact that the nucleons couple together so strongly, that for most applications the nucleus can be considered as a single spinning particle. Thus an external magnetic field does not have the strength to break the nucleon coupling and results in a nuclear energy splitting according to the normal Zeeman effect. The formalism of the *nuclear magnetic resonance* (NMR) was implicitly introduced in Section 2.3. By substituting (2.30) in (2.38) one obtains the atomic energies in a strong magnetic field in the form:

$$E_{M_I\,M_J} = g_J\,\mu_B\,B_0\,M_J - g_I\,\mu_N\,(B_0 - \langle B(0)\rangle\,M_J/\,J)\,M_I\,, \tag{2.52}$$

and therefore:

$$E_{M_I+1} - E_{M_I} = -g_I\,\mu_N\,B\,, \tag{2.53}$$

where B is the attenuated magnetic field at the nucleus. High precision measurements, as those described in this dissertation, must account for the shielding effects of the electron environment. The energy splitting (2.53) is equidistant. Thus at a resonance frequency, photons with energy:

$$h\,\nu_L = |g_I|\,\mu_N\,B\,, \tag{2.54}$$

will be absorbed by the atom. The absorption frequency ν_L, known as the *Larmor frequency*, describes the precession of the average nuclear magnetic moment, and so the nuclear spin, around the magnetic field axis. Magnetic resonance measurements are often done in solids with a cubic crystal structure, since they provide a homogeneous electric field and hence no quadrupole splitting. However, if the subject of interest is the nuclear quadrupole moment, crystal structures violating the cubic symmetry are the only environments generating large enough electric-field gradients[A] and detectable quadrupole interactions. The latter are described by the second term in (2.24):

$$H(E2) = \frac{h\nu_Q}{4I(2I-1)\,\hbar^2}\,\left[3\boldsymbol{I}_z^2 - \boldsymbol{I}^2 + \eta\,\left(\boldsymbol{I}_x^2 - \boldsymbol{I}_y^2\right)\right], \tag{2.55}$$

where

$$\nu_Q = e\,Q\,V_{zz}/\,h \tag{2.56}$$

is the *quadrupole frequency* and $\eta = (V_{xx} - V_{yy})/\,V_{zz}$ is the *asymmetry parameter* of the electric-field gradient. The energy levels for $\eta = 0$ according to (2.55)

[A] The electric-field gradient tensor is $\hat{V} = \mathrm{Grad}\big[\,\mathrm{grad}\,\varphi(\boldsymbol{r})\,\big] = \nabla\nabla\varphi(\boldsymbol{r})$, where $\varphi(\boldsymbol{r})$ is the electric potential. In the principle axis system (PAS) $V_{ij} = \partial^2\varphi(\boldsymbol{r})/\partial r_i\partial r_j = 0$ for $i \neq j$ and $\mathrm{tr}(\hat{V}) = 0$. Thus $\hat{V}$ is described by only two parameters V_{zz} and $\eta = (V_{xx} - V_{yy})/\,V_{zz}$. In PAS $|V_{zz}| \geq |V_{yy}| \geq |V_{xx}|$ and therefore $\eta \in [0,\,1]$.

are:

$$E_{M_I} = \frac{h\nu_Q}{4I(2I-1)} \left[3M_I^2 - I(I+1)\right] \tag{2.57}$$

and therefore:

$$E_{M_I+1} - E_{M_I} = \frac{3h\nu_Q}{4I(2I-1)} (2M_I + 1). \tag{2.58}$$

The sum of (2.53) and (2.58) fully describes the energy splitting of a nucleus with a spin I in an electromagnetic field, characterized only by B and V_{zz}. More information about magnetic and quadrupole resonance can be found in dedicated texts, for instance Ref. [46].

The magnetic resonance measurements, described in this dissertation, are based on the anisotropy of the β decay of an oriented nuclear ensemble. The angular distribution of the emitted $\beta^{\pm}$ particles, as described in Ref. [47], is:

$$W(\theta) = 1 + \frac{\upsilon}{c} A_\beta P \cos\theta \,, \tag{2.59}$$

where

$$P = \sum_{M_I=-I}^{I} p\,(M_I)\, M_I / \, I \,, \tag{2.60}$$

with $p\,(M_I)$ being the probability for occupation of the M_I state, is the *nuclear polarization*, A_β is the *β-asymmetry parameter*, υ is the velocity of the emitted particles and θ is the polar angle towards the orientation axis. The physical meaning of $W(\theta)$ is that the probability for emission in any direction within the solid angle Ω is given by:

$$\mathcal{P}_\Omega = \int_\Omega \frac{W(\theta)}{4\pi} \, d\Omega \,. \tag{2.61}$$

With other words $W(\theta)/4\pi$ is the probability density associated with one particular direction[A]. The β-asymmetry parameter is a specific property of every

[A] The direction through the elementary solid angle $d\Omega = \sin\theta \, d\theta \, d\varphi$.

Table 2.1: Asymmetry parameter A_β for allowed Gamow-Teller β transitions. The upper sign corresponds to an electron decay.

$I_i \to I_f$	$A_{\beta^\mp}$
$I_f = I_i + 1$	$\pm\dfrac{I_i}{I_i+1}$
$I_f = I_i - 1$	∓ 1
$I_f = I_i$	$\mp\dfrac{1}{I_i+1}$

β-decaying state. In the case of allowed Gamow-Teller transitions it can be calculated as[A]:

$$A_\beta = \sum_f b_{if}\, A_\beta^{if}\ , \tag{2.62}$$

where b_{if} denote the branching fractions and A_β^{if} are the partial β asymmetries from Tab. 2.1. Experimentally the β-decay anisotropy can be monitored with two scintillation detectors placed at 0° and 180° with respect to the orientation axis. The quantity:

$$\mathcal{A} = \frac{N(0^\circ) - N(180^\circ)}{N(0^\circ) + N(180^\circ)} \approx \frac{\upsilon}{c}\, A_\beta P \tag{2.63}$$

is called *experimental β asymmetry*[B] and it has the advantage to be proportional to both, the β-asymmetry parameter and the nuclear polarization (2.60). The approximation sign in (2.63) results from the assumption that the detector surfaces cover small solid angles, for which the assumption $W(\theta) \approx$ const is valid. A proper calculation of the number of counts N would involve the evaluation of (2.61) according to the geometry of the experimental setup. The ratio υ/c, especially for exotic species with Q_β of the order of several MeV, is often substituted with unity.

Finally by monitoring the experimental β asymmetry (2.63) one is sensitive to the amount of nuclear polarization. By applying an external radio-frequency (RF) field, matching the energy splitting given by the sum of (2.53) and (2.58), one induces transitions between the M_I states, equalizing[C] their population. As a result a resonant drop occurs in the polarization $|P|$ and therefore in the observable $|\mathcal{A}|$, yielding the exact energy splitting and thus the nuclear moments of the state.

2.6 NMR lineshapes with modulation

Following from the phenomenological Bloch equations [46], the nuclear absorption profile is described by the Lorentzian function (3.48)[D]. Since the absorbed energy is proportional to the change in the nuclear polarization (2.60),

[A] Equation (2.62) has the more general form $\upsilon A_\beta = \sum_f b_{if}\, \upsilon_{if}\, A_\beta^{if}$ if one accounts for the different particle velocities υ_{if} depending on the energies of the final states. The latter expression for υA_β can be directly substituted in (2.59). Abbreviation: i - initial, f - final.

[B] The magnetic dipole hyperfine parameter, the β-asymmetry parameter and the experimental β asymmetry have been historically denoted with the same letter. Here they are discriminated through the notation A, A_β and $\mathcal{A}$, respectively.

[C] Excitation and induced emission have the same probability. Levels with higher population $p(M_I)$ will be excited or induced to decay, per unit time, proportionally to $p(M_I)$, thus resulting in their depopulation.

[D] The Lorentzian profile (3.48) is given centered around $x = 0$. For the purposes in this section one must make the substitution $x = \nu - \nu_0$.

the NMR lineshapes observed through the experimental β asymmetry (2.63) are also Lorentzian. There are several major mechanisms of broadening and modification of this profile, related to the specific experimental conditions, as described in Ref. [48]. The following text is dedicated to the specific problem of the frequency-modulation effect on the NMR lineshapes.

Lets consider a frequency modulation $\xi = \nu + M\varphi(t)$, where ν is the applied central frequency, M is the modulation amplitude and $\varphi(t) \in [-1, 1]\ \forall t$ is a periodic reversible function. The time spent for each frequency is:

$$\left|\frac{dt}{d\xi}\right| = \left|\frac{d}{d\xi}\left[\varphi^{-1}\left(\frac{\xi-\nu}{M}\right)\right]\right| . \tag{2.64}$$

The total absorption profile is then given, with a precision to a constant coefficient, as:

$$f(\nu;\, \nu_0,\, \Gamma,\, M) \sim \int_{\nu-M}^{\nu+M} L(\xi-\nu_0;\, \Gamma)\left|\frac{dt}{d\xi}\right| d\xi\,, \tag{2.65}$$

where $L(\xi-\nu_0;\, \Gamma)$ is the Lorentzian profile (3.48). One can change the variables with the substitution $\tau = (\xi-\nu)/M$, leading to:

$$f(\nu;\, \nu_0,\, \Gamma,\, M) \sim \int_{-1}^{1} L(M\tau+\nu-\nu_0;\, \Gamma)\left|\frac{d}{d\tau}\left[\varphi^{-1}(\tau)\right]\right| d\tau\,. \tag{2.66}$$

For the purpose of fitting experimental spectra one needs a function with an amplitude of a unity. It is therefore more convenient to consider the function $g(\nu;\, \nu_0,\, \Gamma,\, M) = f(\nu;\, \nu_0,\, \Gamma,\, M)/f(\nu_0;\, \nu_0,\, \Gamma,\, M)$. Thus one can make all the considerations with a precision to a constant parameter, without any loss of generality. Lets consider first the case of a *ramp modulation*:

$$\varphi(t) = \frac{2}{T}\,(t-kT), \quad t \in \left[-\frac{T}{2}+kT,\, \frac{T}{2}+kT\right], \quad \forall k \in \mathbb{Z}\,; \tag{2.67}$$

where T is the period of the modulation. Substituting (2.67) and (3.48) into (2.66), one obtains an analytical expression for the line profile:

$$f(\nu;\, \nu_0,\, \Gamma,\, M) \sim \left[\operatorname{arctg}\frac{2(\nu-\nu_0+M)}{\Gamma} - \operatorname{arctg}\frac{2(\nu-\nu_0-M)}{\Gamma}\right] . \tag{2.68}$$

In the case of a *sinusoidal* modulation $\varphi^{-1}(\tau) = \arcsin(\tau)$, the integral (2.66) reduces to:

$$f(\nu;\, \nu_0,\, \Gamma,\, M) \sim \int_{-1}^{1}\left\{1+\left[\frac{2(M\tau+\nu-\nu_0)}{\Gamma}\right]^2\right\}^{-1}\frac{d\tau}{\sqrt{1-\tau^2}}\,. \tag{2.69}$$

The integral (2.69) is absolutely convergent, despite the singularities at $\tau = \pm 1$. The theoretical profiles (2.68) and (2.69), with $M = \Gamma$, are drawn in

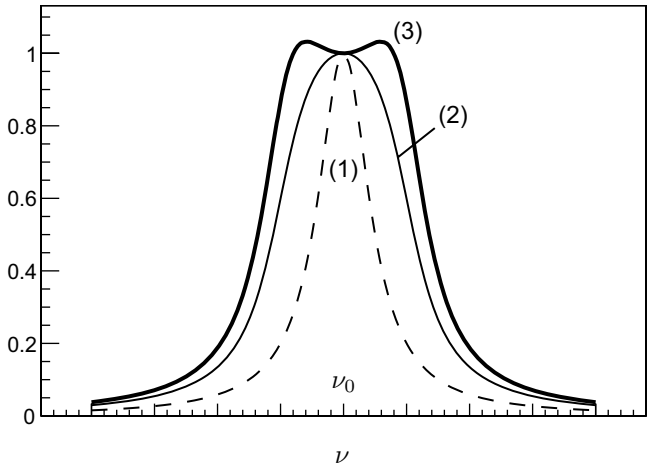

Figure 2.1: Theoretical NMR curves with a frequency modulation $M = \Gamma$. (1) The natural Lorentzian NMR profile; (2) Line profile for a ramp modulation [the normalized function (2.68)]; (3) Line profile for a sin modulation [the normalized function (2.69)];

Fig. 2.1. The second function is treated numerically using Bode's rule from Refs. [49, 50]. Both functions can be used for fitting experimental data. Since the frequency generators available at COLLAPS provide a sinusoidal modulation, (2.69) played an important role in bringing consistency between the NMR spectra of ^{33}Mg, obtained with different frequency modulations. The very first NMR spectrum of ^{33}Mg, detected with a frequency modulation of 20 kHz, much larger than the Lorentzian width of the resonance, is drawn in Fig. A.4 (a).

Chapter 3

Laser spectroscopy

3.1 Collinear laser spectroscopy at ISOLDE

The neutron rich Mg isotopes are produced at ISOLDE - CERN [51] by 1.4 GeV protons impinging on a thick UC_x/graphite target. By maintaining the target at a temperature of $\approx 2000°C$, the diffusion is accelerated and release times of the order of a few hundred milliseconds are achieved, enabling the extraction of short-lived species. Laser ionization is applied to chemically select Mg [52] with partial yields according to Tab. 3.1. The radioactive beams are typically

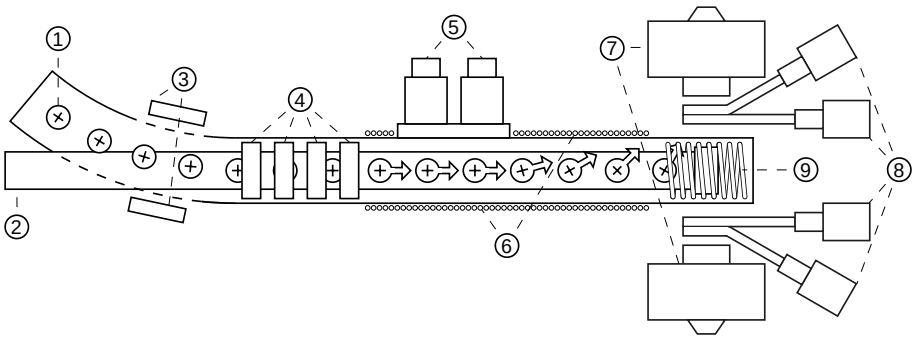

Figure 3.1: Collinear laser spectroscopy setup (COLLAPS) at ISOLDE - CERN 1. Incoming singly ionized atoms; 2. Laser beam overlapped with the ion beam; 3. Electrostatic-deflection plates; 4. Post-acceleration lenses; 5. Photo tubes; 6. Guiding-field coils; 7. Magnet poles; 8. Scintillation detectors; 9. Host crystal and RF coil;

accelerated to 60 keV, mass analyzed with the general purpose separator (GPS) and delivered to the collinear laser spectroscopy setup COLLAPS, drawn in Fig. 3.1.

Optical spectroscopy at COLLAPS involves the first section of the apparatus, up to the optical detection (5) in Fig. 3.1. The singly ionized Mg (Mg II) resonantly interacts with linearly polarized[A] UV (≈ 280 nm) laser radiation. The laser setup consists of an Ar^+ laser, pumping a ring dye laser using Pyrromethene 556 as the lasing medium, which is in turn coupled to a frequency doubler. The hyperfine structure is studied through the atomic fluorescence, detected with the phototubes (5), as a function of the laser frequency in the reference frame of the beam[B]:

$$\nu = \nu_0 \frac{1 \pm \beta}{\sqrt{1-\beta^2}} , \tag{3.1}$$

[A] One must discriminate the *spin polarization* from the *optical polarization*. The latter describes the behavior of the electromagnetic waves intensity vectors in time.

[B] This is a specific case of the *relativistic Doppler effect* $\nu = \nu_0(1 - \beta\cos\phi)/\sqrt{1-\beta^2}$, where ϕ is the angle between the propagation direction of the radiation and the velocity $\vec{v}$ of the observer ($\beta = |\vec{v}|/c$).

Table 3.1: ISOLDE yields and half-lifes of neutron-rich Mg isotopes.
Maximum beam intensities of $^{29,\dots,33}$Mg established with the β detection of the COLLAPS setup. The quoted values represent the number of *particles per proton pulse* (ppp) injected in the apparatus and correspond to bunches of 2.7×10^{13} protons. The β detectors cover $\approx 10\,\%$ of the solid angle and accordingly detect the same fraction of the quoted yields. The half-life of ^{31}Mg is calculated as the weighted mean from the values in Refs. [53, 54]. The one of ^{33}Mg is taken from Ref. [55]. The other half-lifes are according to Ref. [53].

	^{29}Mg	^{30}Mg	^{31}Mg	^{32}Mg	^{33}Mg
$\tau_{1/2}$	1.30(12) s	335(17) ms	233(16) ms	120(20) ms	90.5(16) ms
ppp	$\approx 5 \times 10^6$	$\approx 2 \times 10^6$	$\approx 6.3 \times 10^5$	$\approx 1.8 \times 10^5$	$\approx 2.3 \times 10^4$

The long-lived beams were observed as continuous currents on a Faraday cup at the entrance of the apparatus. These measurements were done with another target, with a factor of ≈ 2 worse performance, than the one used for the measurements above. The beam currents correspond to pulses of 1.5×10^{13} protons, every 1.2 s.

	^{27}Mg	^{28}Mg
$\tau_{1/2}$	9.458(12) m	29.91(3) h
pA	≈ 40	> 10

with ν_0 being the laser frequency in the space-fixed frame. The signs $\langle + \rangle$ and $\langle - \rangle$ pertain to anti-collinear and collinear beam-laser alignment (in our case collinear, therefore the sign $\langle - \rangle$ must be considered). Using the energy increment $E - E_0 = Uq$, one obtains the ratio of the beam velocity over the speed of light:

$$\beta = \frac{|\vec{v}|}{c} = \sqrt{1 - \frac{M_0^2 c^4}{(Uq + M_0 c^2)^2}} \,. \tag{3.2}$$

Here U is the total acceleration voltage, q is the charge of the ions and M_0 is their rest mass[A]. Hence by scanning U, through varying the potential of the electrodes (4) in Fig. 3.1, one observes the fluorescence from the transitions of the hyperfine structure and obtains the energy splittings in accordance with (2.31). The latter enables the extraction of the hyperfine parameters (2.30) and (2.32) and consequently the associated nuclear moments through the use of (2.33) and (2.34).

β-decay spectroscopy and nuclear magnetic resonance demands additional steps. The laser radiation, now circularly polarized, interacts with the atoms, when the Doppler-shifted laser frequency (3.1) coincides with a transition of the hyperfine structure. Optical pumping takes place, polarizing the atomic beam in the direction of the photons momentum, parallel to an applied weak magnetic field of ≈ 0.6 mT. The latter is produced by the coils (6) in Fig. 3.1 and has the purpose of maintaining the atomic orientation. The field is gradually increased by the magnet (7) to ≈ 0.3 T, perpendicular to the propagation axis, causing an adiabatic decoupling of the electron and nuclear spins and resulting in a nuclear polarization (2.60). After an implantation in a crystal (9), the β-decay anisotropy is monitored with two telescopes of ΔE scintillators (8), placed at 0° and 180° with respect to the orientation axis. The experimental β asymmetry (2.63), constructed from the coincidence events, is monitored as a function of the laser frequency in the reference frame of the beam or as a function of an external radio frequency field. In this manner one obtains independently the hyperfine structure, by scanning the total acceleration voltage, and the nuclear moments, by means of nuclear magnetic and quadrupole resonance. The combination of the two techniques is used for direct measurements of ground-state nuclear spins as described in Section 5.3.

3.2 Einstein coefficients

For the purpose of simulating hyperfine-structure spectra, one must calculate the *Einstein coefficients*. First consider a two-level atomic system (Fig. 3.2),

[A] The ion rest mass M_0 can be calculated from the atomic mass M_A by using $M_A c^2 + E_i = M_e c^2 + M_0 c^2$, where $E_i = 7.646238(5)$ eV is the ionization energy of Mg I from Ref. [56] and M_e is the electron rest mass.

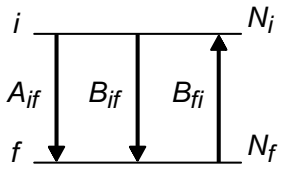

Figure 3.2: Two-level atomic system.

with states denoted by $|i\rangle$ (initial) and $|f\rangle$ (final) and population densities N_i and N_f, respectively. The latter represent the number of atoms in a particular state per unit volume. The probability for a spontaneous decay from $|i\rangle$ to $|f\rangle$ per unit time is called the *spontaneous emission coefficient* or Einstein A coefficient:

$$A_{if} = \frac{d\mathcal{P}\big(\text{spontaneous}: \ |i\rangle \to |f\rangle\big)}{dt} \, . \tag{3.3}$$

If an atom is subjected into a field with a *spectral energy density*[A] $\rho(\nu)$, the probabilities per unit time for absorption or emission are given by:

$$\rho(\nu_{if})\, B_{fi} = \frac{d\mathcal{P}\big(\text{absorption}: \ |f\rangle \to |i\rangle\big)}{dt} \, , \tag{3.4}$$

$$\rho(\nu_{if})\, B_{if} = \frac{d\mathcal{P}\big(\text{induced}: \ |i\rangle \to |f\rangle\big)}{dt} \, . \tag{3.5}$$

The Einstein's B coefficients B_{fi} and B_{if} are referred to as *absorption coefficient* and *induced emission coefficient*. Directly from the definitions (3.3), (3.4) and (3.5) one finds the change in the populations in time:

$$\left| \begin{array}{l} \dfrac{dN_i}{dt} = -A_{if}\, N_i - \rho(\nu_{if})\, B_{if}\, N_i + \rho(\nu_{if})\, B_{fi}\, N_f \\ \dfrac{dN_f}{dt} = -\dfrac{dN_i}{dt} \, , \end{array} \right. \tag{3.6}$$

where the second equation is written shortly with the aid of $N_i + N_f = N = \text{const}$. The relation between the Einstein coefficients can be derived for an arbitrary field, for instance a thermal radiation, and since they are constants that only depend on the atomic properties and not on the field, the result will be valid in general. In a stationary state $dN_i/dt = dN_f/dt = 0$. Thus from (3.6) directly follows:

$$\rho(\nu_{if}) = \frac{A_{if}/B_{if}}{\dfrac{N_f}{N_i}\,\dfrac{B_{fi}}{B_{if}} - 1} \, . \tag{3.7}$$

[A] $\rho(\nu)\, d\nu$ is the energy deposited in a unit volume in the frequency range $d\nu$.

Using the Boltzmann distribution:

$$\frac{N_f}{N_i} = \frac{g_f}{g_i}\, e^{h\nu/kT}\,, \tag{3.8}$$

where g_i and g_f are the degeneracy factors, and identifying (3.7) with the Planck's law:

$$\rho(\nu) = \frac{8\pi\nu^2}{c^3}\frac{h\nu}{e^{h\nu/kT}-1}\,, \tag{3.9}$$

for all ν_{if}, one arrives with:

$$A_{if} = \frac{8\pi h\nu^3}{c^3}\, B_{if}\,, \tag{3.10}$$

$$B_{fi} = \frac{g_i}{g_f}\, B_{if}\,. \tag{3.11}$$

When considering the transitions between the magnetic states $|JIFM_F\rangle$ of the hyperfine structure, the degeneracy factors must be substituted by unity $g_i = g_f = 1$. More information can be found in Ref. [57].

The physical meaning of the A coefficient (3.3) is *the number of spontaneous decays per level per unit time*, with other words $A_{if} = -dN_{if}/(N_{if}\,dt) = 1/\tau_{if}$, where τ_{if}^{-1} is the *decay rate* or the inverse *lifetime*, associated with the transition $|i\rangle \to |f\rangle$. Lets consider now that the state $|i\rangle$ can decay to a number of final states $|f_j\rangle$. In this case, generalizing (3.6), the change in the population density due to the spontaneous decays is $dN_i/dt = -N_i \sum_j A_{ij}$ and so the inverse lifetime of the state $|i\rangle$ for decaying to all the states $|f_j\rangle$ is the sum of the inversed partial lifetimes. In terms of spontaneous emission coefficients this is:

$$A_i = \sum_j A_{ij} = \sum_j 1/\tau_{ij} = 1/\tau_i\,. \tag{3.12}$$

The total decay rate between the magnetic components $|JIFM\rangle$ of the hyperfine structure is given by:

$$A_{if} = \mathcal{C}\nu^3\, |\langle J_f I F_f M_f|\hat{D}_{\lambda\mu}|J_i I F_i M_i\rangle|^2\,, \tag{3.13}$$

where $\hat{D}_{\lambda\mu}$ ($\lambda = 1$, $\mu = M_f - M_i$) represent the spherical components of the electric dipole moment $\boldsymbol{D}$ and $\mathcal{C}$ is a combination of physical constants[A]. Details about polarization and angular distribution of the fluorescence can be found in Ref. [43]. Since the hyperfine structure splitting is many orders in magnitude smaller than the energy of the transitions[B], $\nu_{if} = \nu$ can be considered a constant. Applying the Wigner-Eckart theorem (2.2):

$$\langle J_f I F_f M_f|\hat{D}_{1\mu}|J_i I F_i M_i\rangle = \begin{pmatrix} F_f & 1 & F_i \\ -M_f & \mu & M_i \end{pmatrix} \langle J_f I F_f||\hat{D}_1||J_i I F_i\rangle \tag{3.14}$$

[A] $\mathcal{C} = 4\alpha(2\pi)^3/(3c^2e^2)$ [43] (p. 307), where α is the fine-structure constant.
[B] For Mg II is $\Delta E(3^2S_{1/2})/h\nu \approx 10^{-6}$.

and using the reduced matrix element:

$$\begin{aligned}\langle J_f I F_f||\hat{D}_1||J_i I F_i\rangle &= (-1)^{F_i+J_f+I+1}\sqrt{(2F_i+1)(2F_f+1)} \\ &\times \left\{ \begin{array}{ccc} J_f & F_f & I \\ F_i & J_i & 1 \end{array} \right\} \langle J_f||\hat{D}_1||J_i\rangle\end{aligned} \tag{3.15}$$

from Ref. [43] (p. 91), one finds an expression for A_{if} that can be summed over all final states:

$$\begin{aligned}A_{if} &= \mathcal{C}\nu^3\,|\langle J_f||\hat{D}_1||J_i\rangle|^2 \\ &\times (2F_i+1)(2F_f+1) \left(\begin{array}{ccc} F_f & 1 & F_i \\ -M_f & \mu & M_i \end{array} \right)^2 \left\{ \begin{array}{ccc} J_f & F_f & I \\ F_i & J_i & 1 \end{array} \right\}^2\end{aligned} \tag{3.16}$$

Using (3.12) and following the sum rules (A.17) and (A.22) one finds the decay rate of the initial state:

$$\frac{1}{\tau_i} = \sum_{M_f \mu F_f} A_{if} = \mathcal{C}\nu^3\,\frac{|\langle J_f||\hat{D}_1||J_i\rangle|^2}{(2J_i+1)}\,. \tag{3.17}$$

Remarkably, this result does not depend on F_i and M_i and therefore all the states in the $|J_i\rangle$ multiplet are associated with the same lifetime $\tau = \tau_i$. Experimental values for Mg II can be found in Ref. [58]:

$$\tau(3^2P_{1/2}) = 3.854(30)\,\text{ns}\,, \qquad \tau(3^2P_{3/2}) = 3.810(40)\,\text{ns}\,.$$

Substituting (3.17) into (3.16) yields a final expression for the spontaneous emission coefficient:

$$\begin{aligned}A_{if} &= \tau^{-1}(2J_i+1)(2F_i+1)(2F_f+1) \\ &\times \left(\begin{array}{ccc} F_f & 1 & F_i \\ -M_f & M_f-M_i & M_i \end{array} \right)^2 \left\{ \begin{array}{ccc} J_f & F_f & I \\ F_i & J_i & 1 \end{array} \right\}^2\end{aligned} \tag{3.18}$$

From the properties of the $3j$ and $6j$ symbols immediately follow the selection rules for electric dipole radiation:

$$|J_f - J_i| \le 1 \le J_i + J_f \quad \Rightarrow \quad \Delta J = 0\,,\ \pm 1 \ \wedge\ J_i + J_f \neq 0 \tag{3.19}$$

$$|F_f - F_i| \le 1 \le F_i + F_f \quad \Rightarrow \quad \Delta F = 0\,,\ \pm 1 \ \wedge\ F_i + F_f \neq 0 \tag{3.20}$$

$$\Delta M = 0\,,\ \pm 1 \tag{3.21}$$

3.3 Simulation of optical spectra

The *absorption cross section* equals the absorbed energy per unit time divided by the intensity[A] of the incoming radiation:

$$\sigma(\nu) = \frac{B_{fi}\,\rho(\nu)\,h\nu}{I}\,. \tag{3.22}$$

[A] The intensity I is the power of the radiation source per unit area.

An expression for $\sigma(\nu)$ can be derived from the *optical Bloch equations* [59] (p. 137-140). It is of the form:

$$\sigma(\nu) = A_{if}\,\frac{c^2}{8\pi\nu_0^2}\,\frac{1}{\pi}\,\frac{\Gamma/4\pi}{(\nu-\nu_0)^2+(\Gamma/4\pi)^2}\,, \tag{3.23}$$

where $\Gamma/2\pi = \tau^{-1}/2\pi$ is the *natural linewidth* of the decaying state and ν_0 is the transition frequency. Having the coefficients A_{if} (3.18) and

$$D_{if(fi)} = B_{if(fi)}\,\rho(\nu)\,, \tag{3.24}$$

through (3.22) and (3.23), one can write the rate equations (3.6) for the multitude of initial and final states $|J_iIF_iM_i\rangle$ and $|J_fIF_fM_f\rangle$:

$$\left|\begin{array}{l} \dot{N}_i = -N_i\sum\limits_{j=g'}^{g-1}(A_{ij}+D_{ij}) + \sum\limits_{j=g'}^{g-1}N_jD_{ji}\,, \quad \forall\, i = 0\,,\,1\,,\ldots,\,g'-1 \\ \dot{N}_i = \sum\limits_{j=0}^{g'-1}N_j(A_{ji}+D_{ji}) - N_i\sum\limits_{j=0}^{g'-1}D_{ji}\,, \quad \forall\, i = g'\,,g'+1\,,\ldots,\,g-1 \end{array}\right. \tag{3.25}$$

The degeneracy factors[A] of the two states are $g' = (2I+1)(2J_i+1)$ and $g'' = (2I+1)(2J_f+1)$. The total number of states is $g = g'+g''$. The notation $|i\rangle$ and $|f\rangle$ is abandoned in (3.25), since the aim is to write this system of *linear differential equations with constant coefficients* in the form:

$$\dot{N} = \hat{M}\cdot N\,, \tag{3.26}$$

where N is the vector of the population densities, $\dot{N} = dN/dt$ and $\hat{M}$ is a $g\times g$ matrix. Electric dipole radiation within any of the multiplets is forbidden by the parity selection rule. Thus one can formally write:

$$\left|\begin{array}{l} 0\le i\le g'-1 \\ 0\le j\le g'-1 \end{array}\right. \quad\vee\quad \left|\begin{array}{l} g'\le i\le g-1 \\ g'\le j\le g-1 \end{array}\right. \quad\Rightarrow\quad A_{ij} = D_{ij} = 0 \tag{3.27}$$

Using (3.27), the more general form of (3.25) becomes:

$$\left|\begin{array}{l} \dot{N}_i = -N_i\sum\limits_{j=0}^{g-1}(A_{ij}+D_{ij}) + \sum\limits_{j=0}^{g-1}N_jD_{ji}\,, \quad 0\le i\le g'-1 \\ \dot{N}_i = \sum\limits_{j=0}^{g-1}N_j(A_{ji}+D_{ji}) - N_i\sum\limits_{j=0}^{g-1}D_{ji}\,, \quad g'\le i\le g-1\,. \end{array}\right. \tag{3.28}$$

[A] The degeneracy factor represents the number of magnetic states in a hyperfine multiplet $g = \sum_{F=|J-I|}^{J+I}(2F+1) = (2I+1)(2J+1)$.

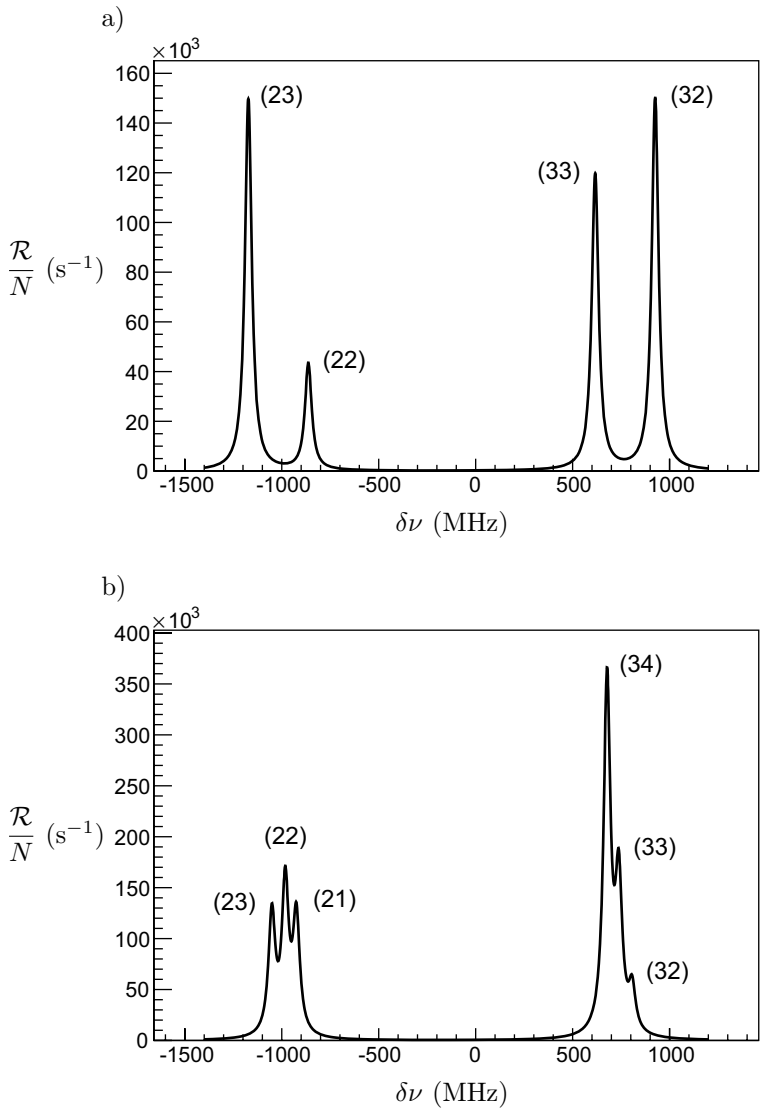

Figure 3.3: Total decay rate of ^{25}Mg II ($I = 5/2$, $A < 0$) in the D_1 and D_2 lines, (a) and (b) respectively.

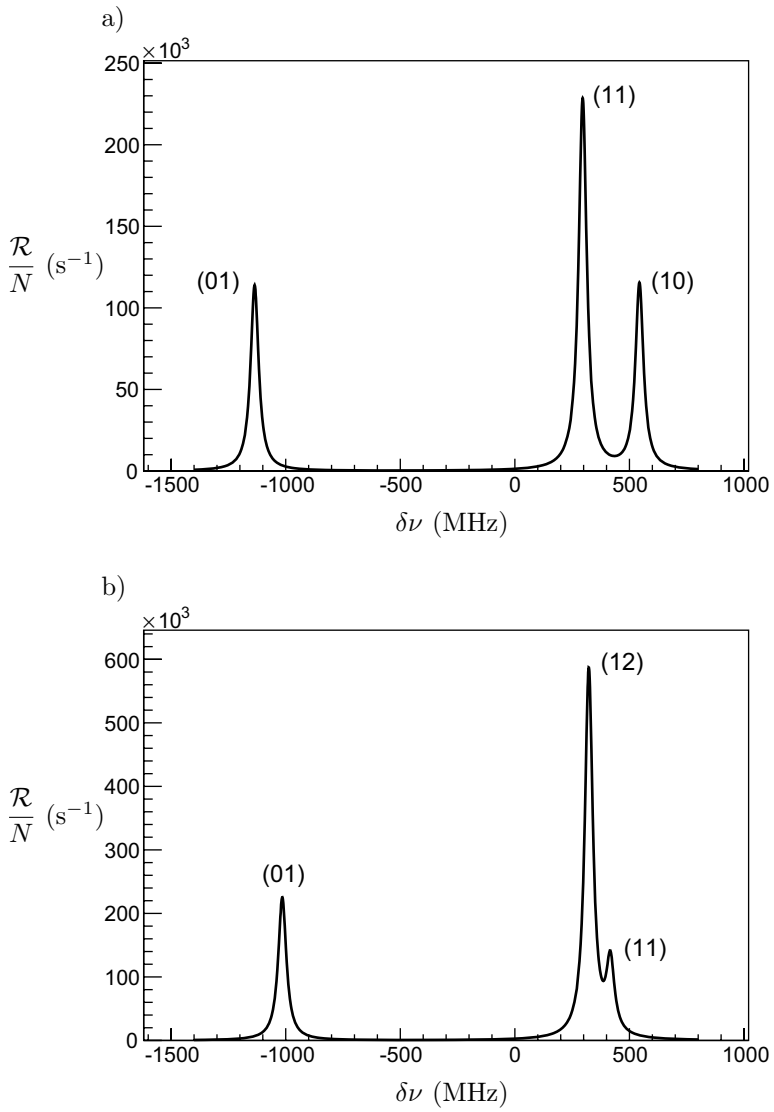

Figure 3.4: Total decay rate of ^{27}Mg II ($I = 1/2$, $A < 0$) in the D_1 and D_2 lines, (a) and (b) respectively.

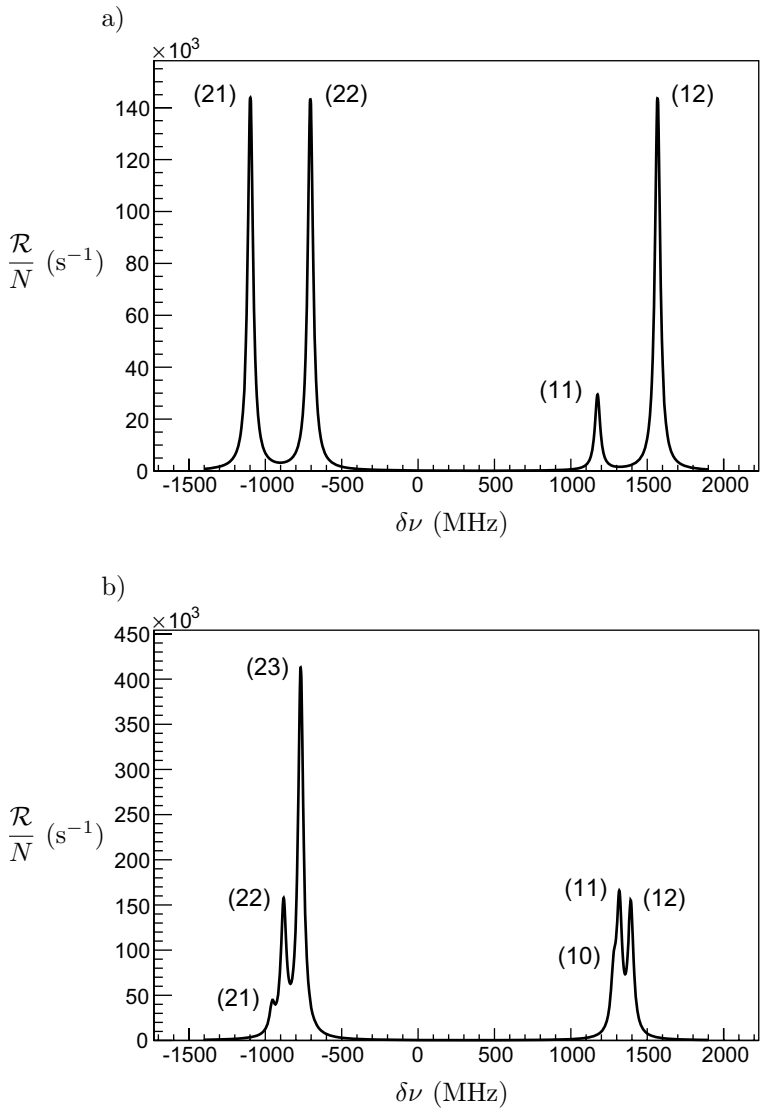

Figure 3.5: Total decay rate of ^{29}Mg II ($I = 3/2$, $A > 0$) in the D_1 and D_2 lines, (a) and (b) respectively.

The only difference with (3.25) is that the summing now goes over the total number of states. Hence, the matrix $\hat{M}$ has the explicit form:

$$\begin{aligned} \underset{0\le i\le g'-1}{M_{ij}} &= \begin{cases} D_{ji}\ , & j\neq i \\ D_{ji}-\sum_{k=0}^{g-1}(A_{ik}+D_{ik})\ , & j=i \end{cases} \\ \underset{g'\le i\le g-1}{M_{ij}} &= \begin{cases} A_{ji}+D_{ji}\ , & j\neq i \\ A_{ji}+D_{ji}-\sum_{k=0}^{g-1}D_{ki}\ , & j=i \end{cases} \end{aligned} \tag{3.29}$$

One can solve the system of differential equations (3.26) and find the population densities, which finally enables the calculation of the total decay rate per unit volume, regardless of the polarization and the angular distribution of the fluorescence:

$$\mathcal{R}=\sum_{\substack{0\le i\le g'-1\\ g'\le j\le g-1}} N_i\,A_{ij}\ . \tag{3.30}$$

The solution of the system differential equations (3.26) can be obtained numerically. A procedure for calculating the population densities has already been implemented in a computer code and outlined in Ref. [12]. Following similar procedure, the code presented in Appendix B.1 is developed independently. It provides for the first time facilities to perform realistic simulations of fluorescence spectra. The hyperfine parameters for the simulated spectra of ^{25,27}Mg II in Figs. 3.3 and 3.4 are taken from Tab. 4.1 and Tab. 4.3. The parameters of ^{29}Mg II are calculated with the aid of (2.33) and the g factors from Tab. 5.2 and Ref. [60]. The B factor is substituted with the lower value given in Section 5.5. The other parameters in (B.1), apart from the quantum numbers, are given the following values: ν_0 from Ref. [56], τ - from Ref. [58], $B=0$, $I_l=80$ W/m^2 and $\Delta M=0$ - linear polarization. The most valuable application of the realistic rate function (B.1) is that it correctly accounts for the effect of simultaneously pumping in two different transitions, which is of significant importance for Mg II in the D_2 line ($3^2S_{1/2}\rightarrow 3^2P_{3/2}$), where the transitions are not completely resolved - Fig. 3.3 (b), Fig. 3.4 (b) and Fig. 3.5 (b). Furthermore it automatically yields the transition strengths and the effect of the laser intensity. These are considered in details in Section 3.4 and Section 3.5, respectively.

3.4 Transition strengths

Looking at Figs. 3.3, 3.4 and 3.5 one makes a notice that the strongest transition in the D_2 line ($3^2S_{1/2}\rightarrow 3^2P_{3/2}$) is stronger, with the same factor for the different spins, than the strongest transition in the D_1 ($3^2S_{1/2}\rightarrow 3^2P_{1/2}$) line. It is often useful to know the transition strengths without doing the time-consuming calculations described in Section 3.3. Lets consider now that

the optical lines are resolved, so that one can neglect the effect of pumping simultaneously several transitions. Consider also that the external radiation is polarized. Then the excitation of only one magnetic state $M_f = M_i - p$, where $p = -1,\ 0,\ 1$ is the laser polarization, will cause a population of the state M_i. Hence one can write the rate equation for this state in the following way:

$$\underbrace{\dot{N}_i}_{0} = -N_i \underbrace{\sum_{M_f\,\mu\,F_f} \underbrace{(A_{if} + D_{if})}_{\approx A_{if}}}_{=1/\tau} + N_f D_{fi}\,, \tag{3.31}$$

where there is no summing over the term the most to the right. In a steady state $\dot{N}_i = 0$. The final, but most important consideration is that $A_{if} \gg D_{if} = D_{fi}$, which enables the transformation of the second term to just $-N_i/\tau$. This quantity, taken with the opposite sign, gives the decay rate per unit volume of the M_i state. Finally summing over all M_i states, effectively summing on both M_i and M_f, since they are locked together by the laser polarization ($M_f = M_i - p$), one finds the total decay rate per unit volume:

$$\mathcal{R} = N_f \sum_{M_i\,M_f} \gamma A_{if}\,. \tag{3.32}$$

The dimensionless quantity γ is the ratio, between induced and spontaneous emission $D_{fi} = D_{if} = \gamma A_{if}$. It can be calculated explicitly from equations (3.22), (3.23) and (3.24):

$$\gamma = \frac{Ic^2}{8\pi h \underbrace{\nu\nu_0^2}_{\approx\nu_0^3}} \frac{1}{\pi} \frac{\Gamma/4\pi}{(\nu-\nu_0)^2 + (\Gamma/4\pi)^2}\,. \tag{3.33}$$

According to the Boltzmann distribution, the population densities N_f are almost equal. Since the degeneracy of the state is $g'' = (2I+1)(2J_f+1) \Rightarrow N_f = N/g''$. Finally, using the sum rule (A.17), one arrives with the decay rate per atom:

$$\frac{\mathcal{R}}{N} = \frac{\gamma}{3\tau} \frac{(2J_i+1)(2F_i+1)(2F_f+1)}{(2I+1)(2J_f+1)} \begin{Bmatrix} J_f & F_f & I \\ F_i & J_i & 1 \end{Bmatrix}^2\,. \tag{3.34}$$

Take a note that everywhere in this thesis $|i\rangle$ is the excited state. The indexes i (initial) and f (final) are given relative to the spontaneous emission (A_{if} : $i \to f$). One can comprehend the transition intensities in Figs. 3.3, 3.4 and 3.5 based on the expression (3.34). It can easily be calculated with the tools given in Appendix A.4.

3.5 Power broadening

The line shape of the optical lines is governed by the *Lorentzian profile* of the absorption cross section (3.23). It was considered in Section 3.4 that the spontaneous emission is much faster than the induced emission. Thus, whenever a state is populated a quick spontaneous decay brings the atom to a lower state, maintaining the population of the excited state negligible. Lets consider a two-level system again Fig. 3.2. In a steady state the amounts of emission and absorption are equal:

$$\underbrace{\dot{N}_i}_{\approx 0} = -N_i(A_{if} + D_{if}) + N_f D_{fi} \,. \tag{3.35}$$

If one substitutes (3.22) and (3.24) into (3.35) one obtains the relation:

$$\mathcal{R} = N_i A_{if} = \frac{I\sigma(\nu)}{h\nu}(N_f - N_i) \,. \tag{3.36}$$

If one eliminates N_f with the aid of $N_i + N_f = N$, after some rearrangements one arrives with the decay rate per atom:

$$\frac{\mathcal{R}}{N} = \frac{I\sigma(\nu)}{h\nu} \frac{1}{1 + \dfrac{2I\sigma(\nu)}{A_{if}h\nu}} \,. \tag{3.37}$$

There are two Lorentzian profiles in this formula entering through $\sigma(\nu)$. The quantity $I_{\mathrm{sat}}(\nu) = A_{if}h\nu/2\sigma(\nu)$ is called *saturation intensity*, although this term is more often used for the saturation intensity at resonance $I_0 = I_{\mathrm{sat}}(\nu_0)$. One can rearrange (3.37) in the final form:

$$\frac{\mathcal{R}}{N} = \frac{I\sigma(\nu_0)}{h\nu_0} \frac{(\Gamma/4\pi)^2}{(\nu - \nu_0)^2 + \left(\dfrac{\Gamma}{4\pi}\sqrt{1 + \dfrac{I}{I_0}}\right)^2} \,. \tag{3.38}$$

Outside the Lorentzian the substitution $\nu \approx \nu_0$ is made. One now realizes that the profile (3.38) is again a Lorentzian profile, but its *full width at half maximum* (FWHM) is increased by a factor of $\sqrt{1 + I/I_0}$. Thus, performing experiments at a low intensity $I \ll I_0$ ensures spectral linewidths equal to the *natural linewidth* $\Gamma/2\pi$. If the amount of power becomes considerable, one can still use the Lorentzian profile as the best approach to experimental data. The power broadening (3.38) has been confirmed experimentally [61].

3.6 Doppler broadening

The decay rate (3.38) was derived regardless of the motion of the atoms. If there is a velocity distribution along the axis of propagation $f(v_z)$, the resonant frequency will be different for every velocity fraction (3.1), causing an additional broadening. In such a case (3.38) must be written in a differential form:

$$d\mathcal{R} = L(\nu - \nu_0)\, dN\,, \tag{3.39}$$

where the function $L(\nu - \nu_0)$ represents the line profile (3.38) and

$$dN = N f(v_z)\, dv_z\,. \tag{3.40}$$

In this case N represents the particle density in the atomic beam. Here it was already pointed out that a way of removing the broadening due to the velocity spread is by producing an atomic beam, accelerated to speeds much larger than those associated with the thermal atomic motion. Since the function $f(v_z)$ represents the density of particles with the same speed, it will be the same before and after the acceleration. Thus one can write $f(v_z) = f'(v_z) + f'(-v_z)$, where $f'(v_z)$ is the Maxwell distribution for one velocity component, which is basically a Gaussian distribution, leading to:

$$f(v_z) = 2\sqrt{\frac{m}{2\pi kT}}\, e^{-\dfrac{m(v_z^2 - v_0^2)}{2kT}}\,. \tag{3.41}$$

Here the energy conservation $mv_z^2/2 = mv_z'^{\,2}/2 + Uq$ was used to express the velocity component v_z' in the target with the minimum beam velocity $v_0 = \sqrt{2Uq/m}$ and v_z $(0 \le v_0 \le v_z)$. Using the classical limit of (3.1):

$$\nu = \nu_L(1 - v_z/c) \tag{3.42}$$

and substituting (3.40) into (3.39) one arrives with:

$$\frac{\mathcal{R}}{N} = 2\sqrt{\frac{m}{2\pi kT}}\; e^{\dfrac{mv_0^2}{2kT}} \int_{v_0}^{\vartheta \ll c} L\left[\nu_L\left(1 - \frac{v_z}{c}\right) - \nu_0\right]\; e^{-\dfrac{mv_z^2}{2kT}}\; dv_z\,. \tag{3.43}$$

With the substitution (3.42) one can write this integral in the form:

$$\frac{\mathcal{R}}{N} = 2\frac{c}{\nu_L}\sqrt{\frac{m}{2\pi kT}}\; e^{\dfrac{mv_0^2}{2kT}} \int_{\xi \gg 0}^{\nu_L(1 - v_0/c)} L(\nu - \nu_0)\, e^{-\dfrac{mc^2(\nu - \nu_L)^2}{2kT\nu_L^2}}\; d\nu\,. \tag{3.44}$$

$\mathcal{R}/N$ must be considered as a function of either v_0 or ν_L. FWHM of the Gaussian under the integral (3.44) for $\nu_L = \nu_0$ is called the *Doppler width*:

$$\Gamma_D = 2\sqrt{2\ln 2}\, \frac{\nu_0}{c}\, \sqrt{\frac{kT}{m}}\,. \tag{3.45}$$

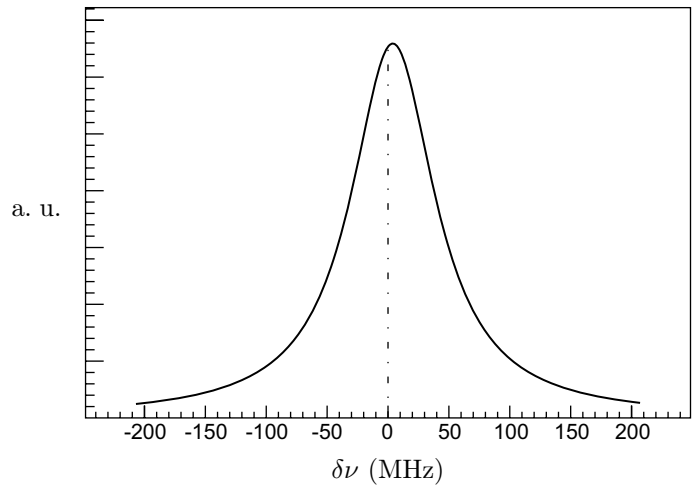

Figure 3.6: Simulated lineshape for ^{24}Mg II in the D_1 line with Doppler effect according to (3.43) and (3.44). Target temperature $T = 2000°$C. Acceleration tension $U = 60$ kV.

The Doppler width is much larger than the natural linewidth ($\Gamma_D \gg \tau^{-1}/2\pi$). However, by looking at (3.43) one realizes that since the Gaussian is centered at $v_z = 0$ and the integral is in the interval $[v_0, \vartheta \ll c)$ it will only be influenced by the tail of the Gaussian, which is almost flat close to v_0, and thus the two Gaussian factors will cancel out to a large extent. With other words, the larger the beam velocity the smaller the Doppler contribution. One must make a note that the lineshapes (3.43) and (3.44) are asymmetric due to the fact that $v_z \geq v_0$. The integral (3.43) is numerically solved, using Bode's rule [49, 50], and plotted in Fig. 3.6 as a function of the Doppler-shifted laser frequency relative to the transition frequency in ^{24}Mg II [56]. The laser frequency was taken such that ^{24}Mg II, with an energy of 60 keV, would have maximum absorption (would be in resonance). Fig. 3.6 ilustrates several facts. (i) The lineshape is Lorentzian-like; (ii) At acceleration voltage and target temperature $U = 60$ kV and $T = 2000°$C, typical for the ISOLDE facility, the asymmetry in the line is small; (iii) There is a considerable shift of a few MHz of the resonance frequency; However since all the components of the hyperfine structure shift by a similar amount, this is not crucial for the determination of their relative distances. Furthermore, broadening occurs in the opposite direction as well, since a considerable fraction of atoms is ionized outside the target-line cavity at a lower potential. Thus the best approach to experimental data is the Voigt profile, which is considered in Section 3.7.

3.7 Voigt profile

A motivation for using the *Voigt profile* for describing the optical lineshapes was laid out in Section 3.6. A normalized Voigt:

$$V(x;\,\sigma,\,\Gamma_L) = \int_{-\infty}^{+\infty} G(t;\,\sigma)\,L(x-t;\,\Gamma_L)\,dt\,, \tag{3.46}$$

is a convolution of normalized Gaussian and Lorentzian profiles:

$$G(x;\,\sigma) = \frac{1}{\sigma\sqrt{2\pi}}\,e^{-x^2/2\sigma^2}\,, \qquad \Gamma_G = 2\sigma\sqrt{2\ln(2)}\,; \tag{3.47}$$

$$L(x;\,\Gamma_L) = \frac{1}{\pi}\,\frac{\Gamma_L/2}{x^2+(\Gamma_L/2)^2}\,. \tag{3.48}$$

The integral (3.43) would indeed have been a Voigt function if the integration limits were extending from $-\infty$ to $+\infty$. The numerical handling of (3.46) is time-consuming, thus triggering the development of numerical methods for approaching the Voigt with a superposition of other symmetric single-peak functions as described in Refs. [62, 63]. The FWHM, according to Ref. [62], is given with the expression:

$$\begin{aligned}\Gamma_V = (&\Gamma_G^5 + 2.69269\,\Gamma_G^4\Gamma_L + 2.42843\,\Gamma_G^3\Gamma_L^2 \\ &+ 4.47163\,\Gamma_G^2\Gamma_L^3 + 0.07842\,\Gamma_G\Gamma_L^4 + \Gamma_L^5)^{1/5}\,,\end{aligned} \tag{3.49}$$

The analysis of the optical spectroscopy data, described in this thesis, involved the use of the *extended pseudo-Voigt* function. It approximates (3.46) with a superposition of Gaussian, Lorentzian, irrational and hyperbolic functions. The numerical procedure is described in Ref. [63]. A numerical implementation of this procedure is given in Appendix B.2.

3.8 Nuclear polarization with optical pumping

The process of *optical pumping* is based on the fact that polarized radiation is associated with a specific selection rule for the increment of the magnetic quantum number. The two orientations of the circular polarization, referred as $\sigma^{\pm}$ radiation, induce excitations with $\Delta M = \pm 1$. A specific example is drawn in Fig. 3.7. The thick arrows represent the process of excitation with $\Delta M = 1$ (σ^+) in a transition $F_f = 1 \rightarrow F_i = 2$, between the hyperfine component of two multiplets. The laser power is assumed to be small, such that the induced emission can be neglected. The deexcitation under this assumption is completely governed by the spontaneous emission, with relative rates determined by the squared $3j$ symbol in (3.18). The population of the excited states can be

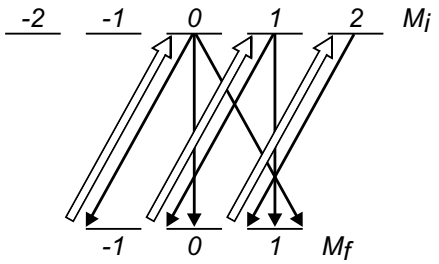

Figure 3.7: Optical pumping in a transition $F : 1 \rightarrow 2$ with σ^+.

neglected compared to the population of the lower state. The process described in Fig. 3.7 leads to the depopulation of the states with $M_f = -1$, 0 and filling the state $M_f = 1$, thus producing an atomic orientation. In the case of considerable power density there would be an induced emission $M_i = 0 \rightarrow M_f = 1$, competing with the spontaneous decay, but only increasing the effect on the atomic orientation. However the disadvantage of working in this mode is the resolution deterioration due to the power broadening.

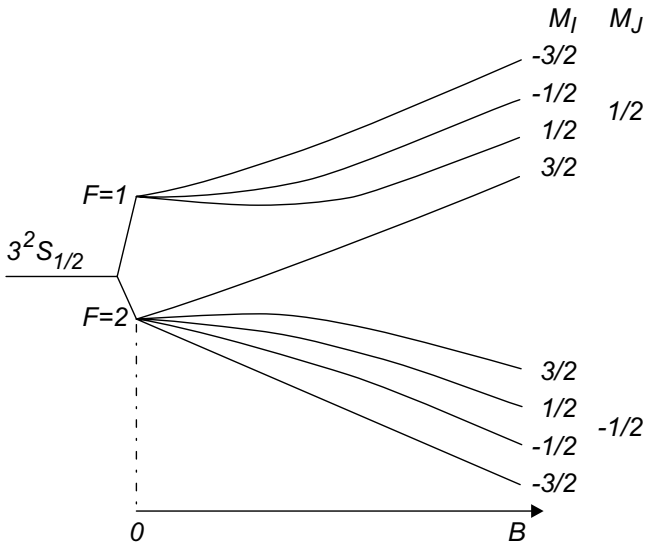

Figure 3.8: Magnetic field effect on the hyperfine structure magnetic substates in $3^2S_{1/2}$ for $I = 3/2$, $A < 0$ and $0 \leq B \ll |A|/\mu_N$.

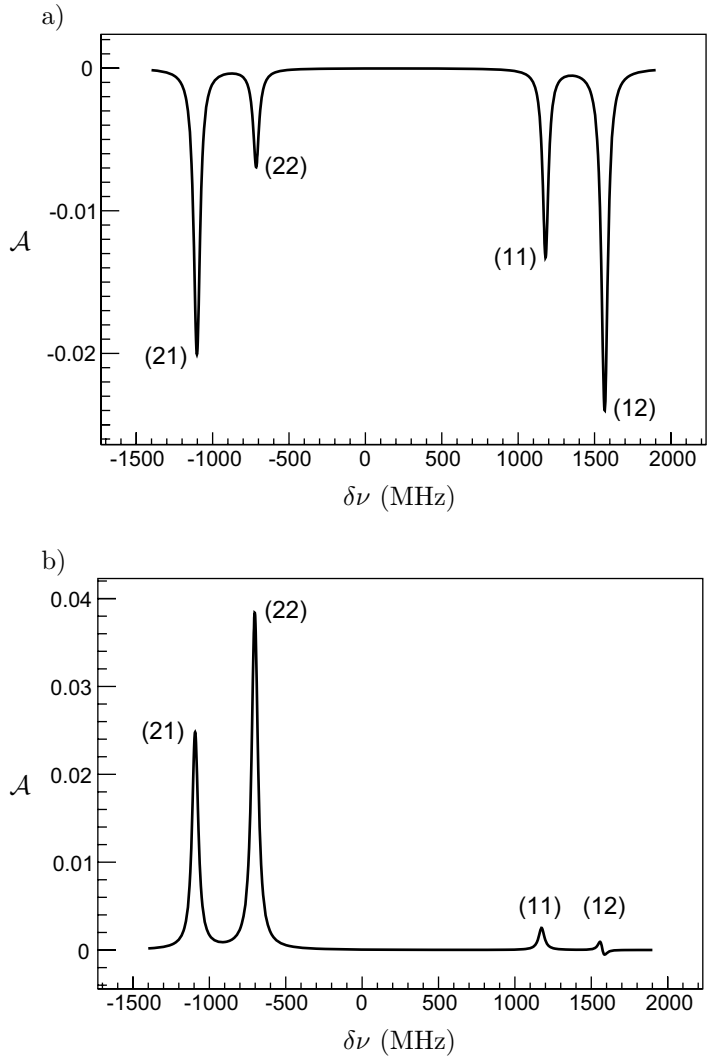

Figure 3.9: Simulated hyperfine structure of ^{29}Mg II ($I = 3/2$, $A > 0$), with σ^- (a) and σ^+ (b) laser polarization, in the D_1 line. Plotted is the experimental β asymmetry $\mathcal{A}$ with $A_\beta = 0.15$.

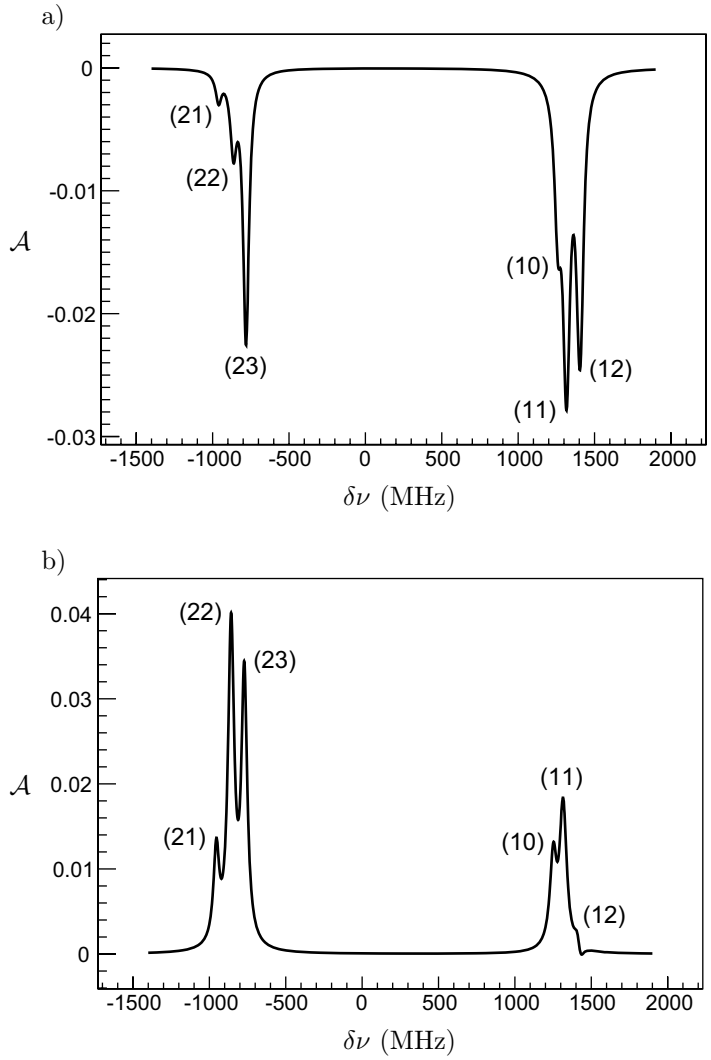

Figure 3.10: Simulated hyperfine structure of ^{29}Mg II ($I = 3/2$, $A > 0$), with σ^- (a) and σ^+ (b) laser polarization, in the D_2 line. Plotted is the experimental β asymmetry $\mathcal{A}$ with $A_\beta = 0.15$.

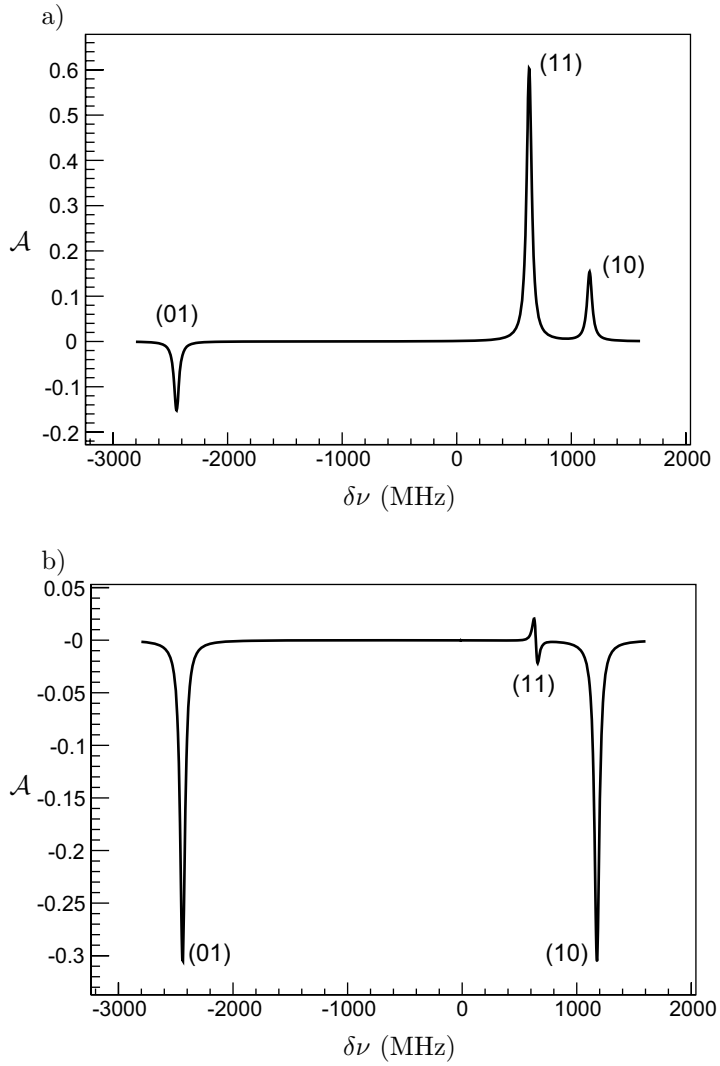

Figure 3.11: Simulated hyperfine structure of ^{31}Mg II ($I = 1/2$, $A < 0$), with σ^- (a) and σ^+ (b) laser polarization, in the D_1 line. Plotted is the experimental β asymmetry $\mathcal{A}$ under the assumption that $A_\beta = -1$.

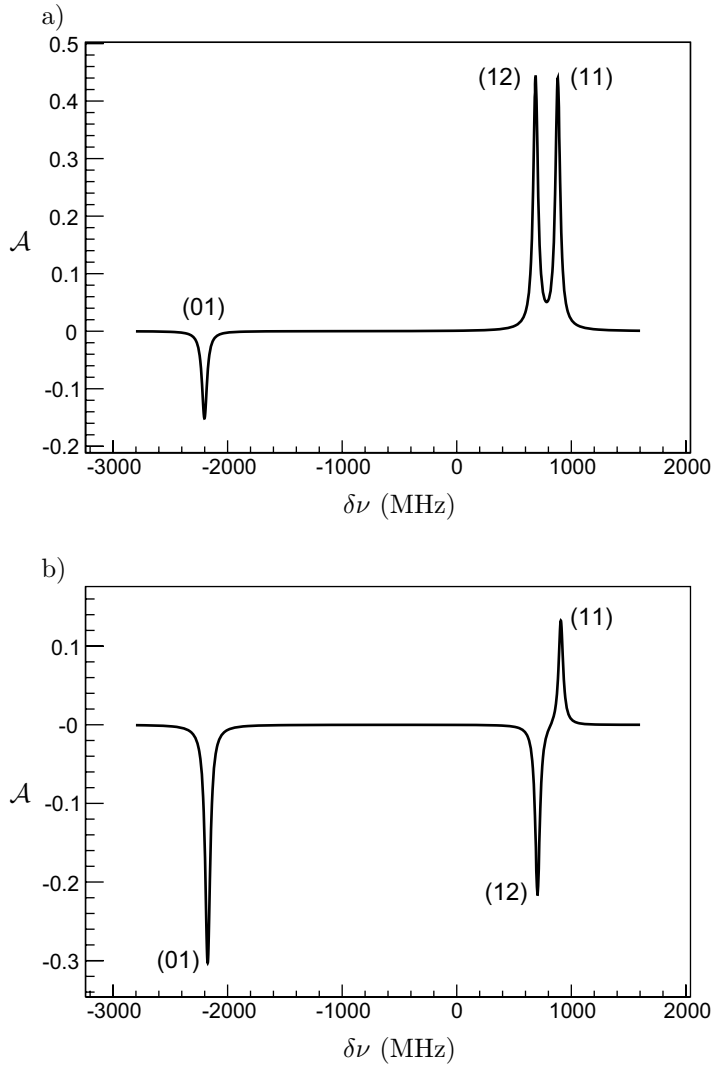

Figure 3.12: Simulated hyperfine structure of ^{31}Mg II ($I = 1/2$, $A < 0$), with σ^- (a) and σ^+ (b) laser polarization, in the D_2 line. Plotted is the experimental β asymmetry $\mathcal{A}$ under the assumption that $A_\beta = -1$.

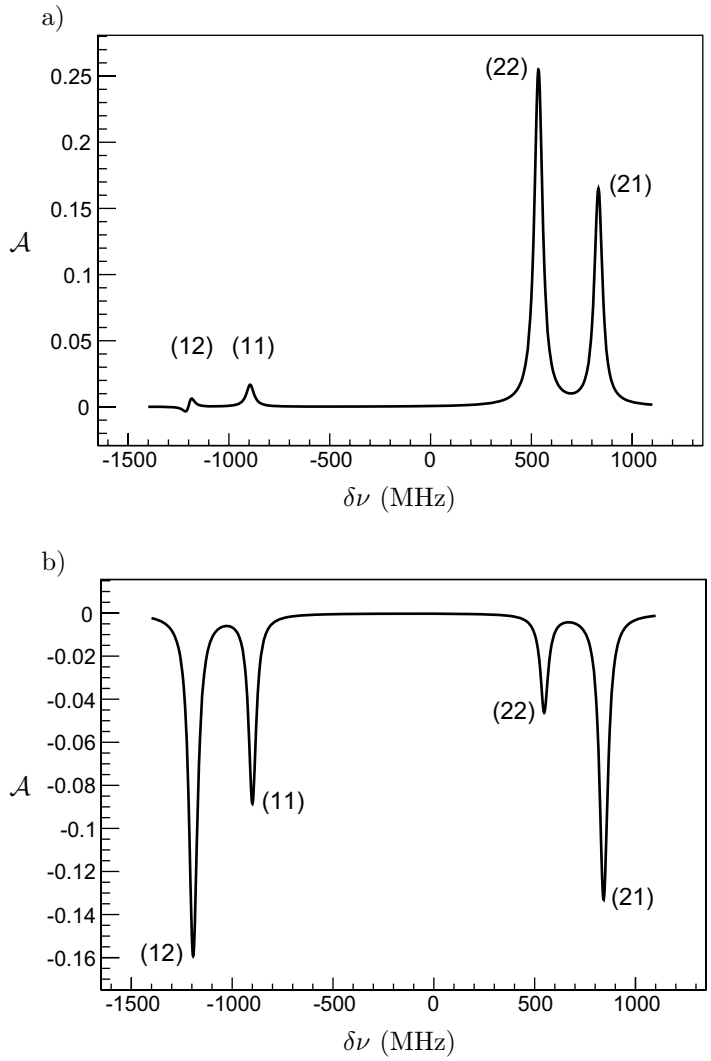

Figure 3.13: Simulated hyperfine structure of ^{33}Mg II ($I = 3/2$, $A < 0$), with σ^- (a) and σ^+ (b) laser polarization, in the D_1 line. Plotted is the experimental β asymmetry $\mathcal{A}$ under the assumption that $A_\beta = -1$.

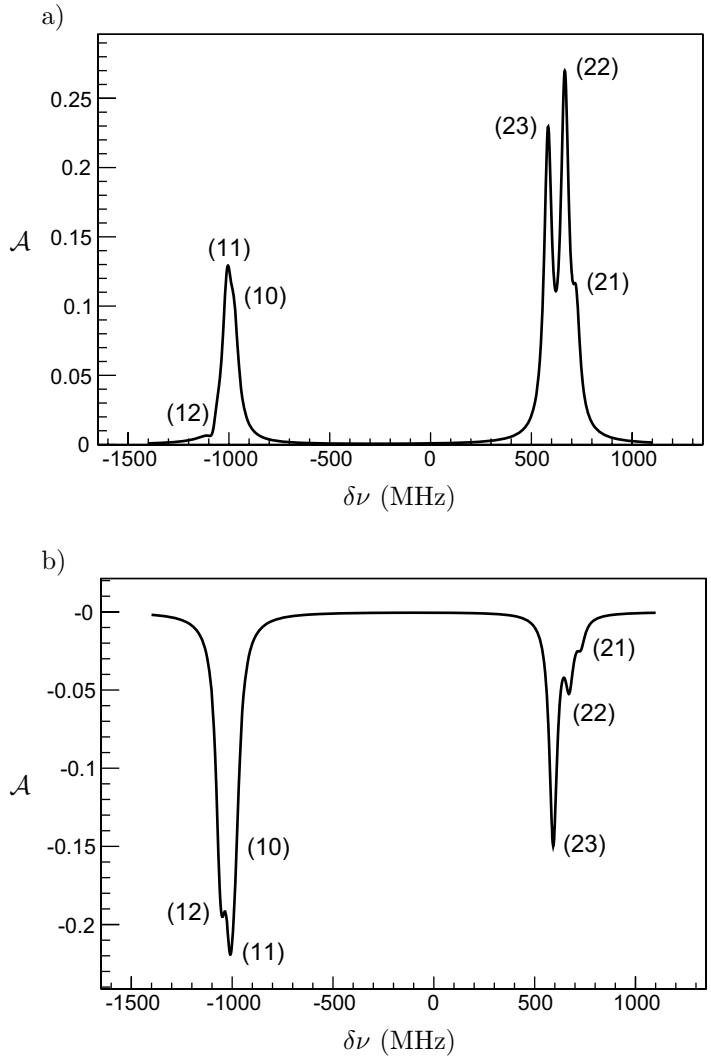

Figure 3.14: Simulated hyperfine structure of ^{33}Mg II ($I = 3/2$, $A < 0$), with σ^- (a) and σ^+ (b) laser polarization, in the D_2 line. Plotted is the experimental β asymmetry $\mathcal{A}$ under the assumption that $A_\beta = -1$.

When performing spectroscopy based on the β-decay anisotropy and NMR, as explained in Sections 2.5 and 3.1, the amplitudes of the resonances are determined by the amount of nuclear polarization (2.60). The procedure for calculating the population of the magnetic components of the hyperfine levels was described in Section 3.3. After such a calculation one needs to translate the atomic into nuclear level populations, in order to calculate the polarization. The effect on the atomic energies, caused by the increment of the magnetic field in sections (6) and (7) of the apparatus (Fig 3.1), is demonstrated in Fig. 3.8. Since the natural linewidth is smaller than the energy shifts, shortly after approaching the section with the strong magnetic field the optical pumping is interrupted, due to the change in the resonance frequency. Since the decoupling of the nuclear and atomic angular momenta is relatively quick, no relaxation process will cause any considerable change in the population of the atomic states. Thus the population of a M_F state is exactly equal to the population of the corresponding M_I state, describing the level at high fields (Fig. 3.8). Make a note that in Fig. 3.8 the energy levels in the strong field limit, described by (2.38), are drawn with the assumption $|A| \gg B\mu_N$, such that the nuclear splitting is neglected. The latter is done for the simplification of the figure and does not have an effect on the considerations above.

The first code for simulating polarization spectra was developed by M. Keim for Na I and outlined in Ref. [12]. The code presented in Appendix B.3 is developed independently, based on the same formalism. The realistic polarization function (B.3) was used to simulate the spectra of ^{29,31,33}Mg II in Figs. 3.9, 3.10, 3.11, 3.12, 3.13 and 3.14. The magnetic hyperfine parameters are calculated with the aid of (2.33) from the parameters of ^{25}Mg II (Tab. 4.1) and the g factors from Tabs. 5.2, 5.2 and 5.4. The quadrupole hyperfine constant of ^{33}Mg II in the D_2 line is neglected for the simulations. In the case of ^{29}Mg II the B parameter is substituted with the lower value established in Section 5.5 and the β-asymmetry parameter is calculated from the branching fractions in Ref. [53] with the use of Tab. 2.1. The guiding field in the optical pumping section and the laser intensity are taken to be 6×10^{-4} T and 80 W/m^2.

The initial work on Mg II is described in the thesis of M. Kowalska [16]. It has not been realized at that time that the M_F and M_I states must be associated in a different way for $A < 0$ and $A > 0$. The inconsistencies in the $\sigma^{\pm}$ assignments and the sign of the β-asymmetry parameter of ^{31}Mg between this dissertation and Ref. [16] are due to omitting this fact in the latter work.

Chapter 4

Optical spectroscopy

The theoretical basis of optical spectroscopy is developed in Chapter 3, together with some specific problems concerning the appropriate lineshapes for data analysis, simulations of optical spectra, etc. The content of this chapter is restricted to the experimental results and their interpretation.

4.1 Hyperfine structure of stable Mg II

This section considers ^{25}Mg II, whose experimental hyperfine parameters are latter used for the investigation of the radioactive Mg isotopes. A discussion on the isotope-shifts between the stable ^{24,25,26}Mg II, extracted from the same set of data, is given in the thesis of M. Kowalska [16].

The transitions: $3^2S_{1/2} \rightarrow 3^2P_{1/2}$ and $3^2S_{1/2} \rightarrow 3^2P_{3/2}$, known as the D_1 and D_2 lines, are studied. Their excitation energies, corresponding to 280.353(79) nm and 279.635(78) nm [56], are in the ultraviolet region. ^{24}Mg II ($I = 0$), being the most abundant of the three isotopes 78.99 %, is the natural choice for a frequency reference. Typical spectra of ^{25}Mg II ($I = 5/2$), which is the only stable atom in the chain with a hyperfine structure, are presented in Fig. 4.1. There is a remarkable agreement with the theoretical simulations in Fig. 3.3. A sophisticated procedure for fitting experimental data can be based on the realistic rate function, developed in Section 3.3. The latter would

Table 4.1: Hyperfine parameters of ^{25}Mg II ($I = 5/2$) in MHz.

$A(3^2S_{1/2})$	$A(3^2P_{1/2})$	$A(3^2P_{3/2})$	$B(3^2P_{3/2})$
−596.54(26)	−102.65(45)	−18.99(32)	23.7(10)

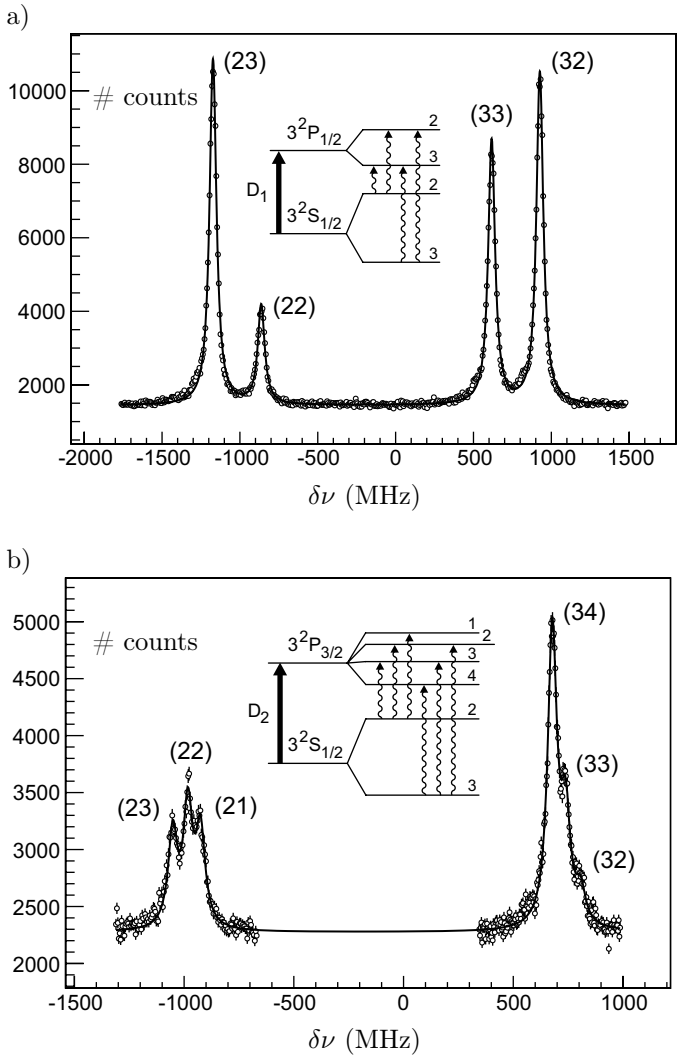

Figure 4.1: Hyperfine structure of ^{25}Mg II ($I = 5/2$) in the D_1 and D_2 lines, (a) and (b) respectively. The fitted curves consist of Lorentzian profiles (3.48).

Table 4.2: Magnetic hyperfine parameters ratios for Mg II.

$A(3^2P_{1/2})/A(3^2S_{1/2})$	$A(3^2P_{3/2})/A(3^2S_{1/2})$
0.17208(43)	0.03183(53)

have been beneficial mostly in the D_2 line, where the transitions are not resolved. However, using conventional Lorentz lineshapes (3.48) was considered the most adequate way of fitting numerous spectra with a good precision. In the D_2 line $A(3^2S_{1/2})$ was fixed to the value extracted in the D_1 line, in order to obtain reliable results on the hyperfine parameters of the excited state. The experimental values are presented in Tab. 4.1. The magnetic moment of ^{25}Mg must be negative, since the ratio A/g is positive for alkali-like atoms [42]. This sign has been confirmed by a measurement with another technique [64]. The ratios of the magnetic hyperfine parameters, which are important inputs to the problems of fitting unresolved or low-statistics spectra, are given in Tab. 4.2.

4.2 Magnetic moment and hyperfine structure of ^{27}Mg II

The hyperfine structure of ^{27}Mg II was studied in the D_1 line. A spectrum, representing one third of the total statistics, is plotted in Fig. 4.2. A comparison with the theoretical curves in Figs. 3.3 (a) ($I = 5/2$), 3.4 (a) ($I = 1/2$) and 3.5 (a) ($I = 3/2$) provides a clear evidence that the nuclear spin of ^{27}Mg is $I = 1/2$. Not only the lack of a fourth transition, but also the transition strengths unambiguously point to the latter spin assignment, hence confirming the value from the literature [65]. The solid line in Fig. 4.2 represents a fitting function consisting of three Voigt profiles (3.46). The latter was handled numerically with the procedure from Section 3.7. The Doppler width was extracted from the spectra of the reference ^{24}Mg II and corrected with the factor $\sqrt{m_{24}/m_{27}}$, according to (3.45). The ratio of the A factors was fixed to the value from Tab. 4.2 in order to involve both weak transitions in the determination of the ground-state splitting. The results from the individual measurements are

Table 4.3: Hyperfine parameters of ^{27}Mg II ($I = 1/2$) in MHz.

$A(3^2S_{1/2})$	$A(3^2P_{1/2})$
−1432.0(46)	−246.4(10)

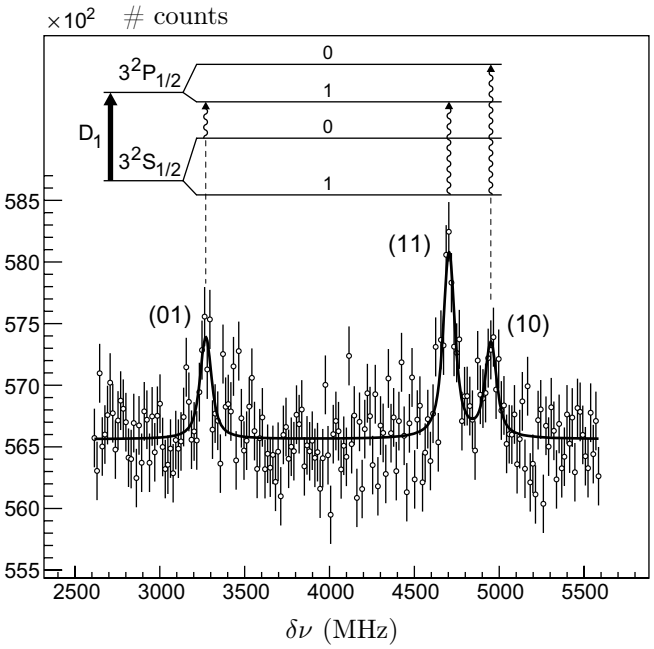

Figure 4.2: Hyperfine structure of ^{27}Mg II ($I = 1/2$) in the D_1 line. The scale is relative to the resonance frequency of ^{24}Mg II.

presented in Tab. A.4. The hyperfine structure of ^{27}Mg II in the D_1 line is characterized by the parameters given in Tab. 4.3. The uncertainties are mainly statistical. Using the A factor of ^{25}Mg II from Tab. 4.1, which is in agreement with the precise value $-596.254376(54)$ MHz [66], one obtains the magnetic moment of the ^{27}Mg ground state through the use of (2.33). The doublet of lines in Fig. 4.2 are on the higher-frequency side of the spectra, revealing that the sign of the A factor is negative. As a result the sign of the magnetic moment is also negative, since the A/g ratio for alkali-like atoms is positive [42]. The results on the nuclear properties of ^{27}Mg are summarized in Tab. 4.4.

In the extreme shell-model picture, the ground-state properties of $^{27}_{12}\mathrm{Mg}_{15}$ are determined by an odd neutron in the $\nu\, 2s_{1/2}$ orbital, with a single-particle

Table 4.4: Nuclear ground-state properties of ^{27}Mg.

$I = 1/2$	$g = -0.8214(26)$	$\mu = -0.4107(13)\,\mu_N$

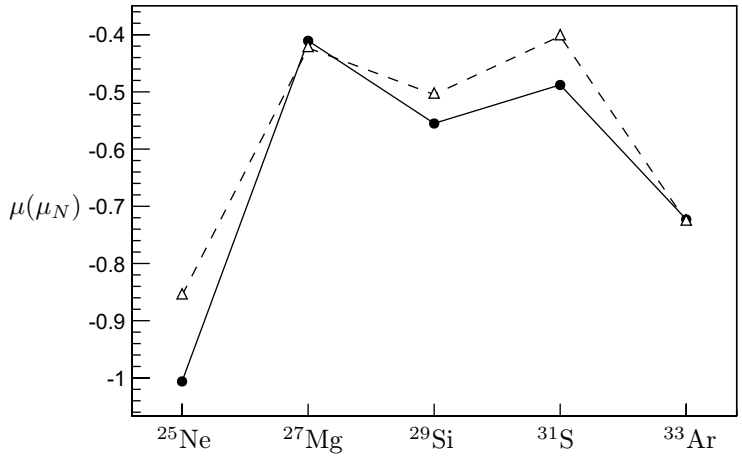

Figure 4.3: Magnetic moments of the even-odd $N = 15$ isotones ($I = 1/2$). The solid line connects the experimental values. The uncertainties are smaller than the dots. The dashed line follows the theoretical predictions. The exact values are given in Tab. 4.5.

magnetic moment $\mu(\nu\, 2s_{1/2}) = -1.91\,\mu_N$, according to (2.7). The experimental spin and sign of the magnetic moment, given in Tab. 4.4, are consistent with the suggested configuration. However, the magnitude of the magnetic moment is significantly smaller, indicating that the ground-state configuration is rather mixed, including a considerable contribution from the positive Schmidt value orbitals $\nu\, 1d_{3/2}$, $\pi\, 1d_{5/2}$, $\pi\, 2s_{1/2}$ and $\pi\, 1d_{3/2}$. The present result completes the set of experimental magnetic moments of the even-odd $N = 15$ isotones ($I = 1/2$) from ^{25}Ne to ^{33}Ar [60, 67, 68]. Complex shell-model calculations are carried out for the entire sequence in the *sd* model space with the code

Table 4.5: Experimental ($\mu_{\rm exp}$) and theoretical ($\mu_{\rm th}$) magnetic moments of the even-odd $N = 15$ isotones ($I = 1/2$).

	$\mu_{\rm exp}(\mu_N)$	$\mu_{\rm th}(\mu_N)$
^{25}Ne	$-1.0062(5)$ [a]	-0.85
^{27}Mg	$-0.4107(13)$ [b]	-0.42
^{29}Si	$-0.55529(3)$ [c]	-0.50
^{31}S	$-0.48793(8)$ [c]	-0.40
^{33}Ar	$-0.723(6)$ [d]	-0.72

[a] From Ref. [67]; [b] Tab. 4.4 - this work; [c] From Ref. [60]; [d] From Ref. [68];

Oxbash [69], using the USD Hamiltonian [70]. The results are presented in Tab. 4.5 and in Fig. 4.3. The agreement theory-experiment is satisfactory in all cases. The increase in the magnitude of the ^{25}Ne and ^{33}Ar moments is due to the fact that there are only two protons (proton holes) in the *sd* shell, leading to less mixed configurations and hence moments closer to the neutron Schmidt value for the $\nu\, 2s_{1/2}$ orbital ($-1.91\,\mu_N$). The experimental spin-parity assignments $1/2^+ \rightarrow 3/2^+ \rightarrow 5/2^+ \rightarrow 5/2^+$ corresponding to the states at $0 \rightarrow 984.66 \rightarrow 1698 \rightarrow 1940$ keV [53] in ^{27}Mg are in good agreement with the calculations, predicting these levels at $0 \rightarrow 895 \rightarrow 1667 \rightarrow 1978$ keV. Experimentally the first negative-parity state in ^{27}Mg is at 3559.5 keV [53], signifying that the *pf* shell plays a role in the energy spectrum close to 3 MeV and above. The results of this chapter will be discussed in Ref. [33].

Chapter 5

β-decay spectroscopy and nuclear magnetic resonance

The theoretical basis of laser spectroscopy is laid down in Chapter 3, with the specific subject of nuclear polarization with optical pumping described in Section 3.8. Information on the topic of NMR lineshapes in the presence of a frequency modulation can be found in Section 2.6. This chapter is dedicated to the β spectroscopy of the odd-mass ^{29,31,33}Mg, concentrating the discussion mainly on the experimental results and their interpretation.

5.1 Magnetic moments of ^{29,31}Mg

The magnetic moments of ^{29,31}Mg are essential quantities for the nuclear-structure understanding in the region of the Island of inversion. The case of ^{31}Mg is presented in a number of publication [15, 30, 31], which are included at the end of this dissertation. Both cases are discussed in the PhD thesis of M. Kowalska [16]. A reevaluation of the magnetic moments is performed here, after an offset in the frequency scale by one channel was recently discovered. The improvement of the results precision has no influence on the conclusions in the above publications.

Polarized beams of ^{29,31}Mg and ^{8}Li were implanted into a MgO crystal during a period of 82 hours and NMR measurements were performed. Typical spectra can be found in Refs. [15, 16, 30, 31]. ^{8}Li with its well-known magnetic moment[A] [71] is used to calibrate the magnetic field. The reevaluated Larmor frequencies are presented in Tab. 5.1. A source of systematic uncertainty is

[A] Ref. [71] provides the ratio: $\nu(^{8}\mathrm{Li})/\nu(^{1}\mathrm{H}) = 0.1480045(21)$, which combined with the proton magnetic moment $\mu(^{1}\mathrm{H}) = 2.792847337(29)\,\mu_N$ from [35] yields $\mu(^{8}\mathrm{Li}) = 1.653547(29)\,\mu_N$. Diamagnetic corrections are taken into account according to Ref. [60].

Table 5.1: NMR frequencies of ^{8}Li and ^{29,31}Mg (weighted mean of the individual measurements for each isotope).

	^{8}Li	^{29}Mg	^{31}Mg
ν (kHz)	1806.940(12)	1423.98(86)	3859.624(42)

the possible magnetic-field drift over the time period mention above. The electric current through the poles of the magnet was monitored with a high-precision voltmeter measuring the tension over a calibrated resistance. The difference between the minimum and maximum voltage recorded during the measurements over the average voltage yields a relative error $\Delta U/U = 5.5 \times 10^{-5}$. Another source of systematic uncertainty is the inhomogeneity of the magnetic field within the area of implantation. If considerable, this effect would result in a change in the Lorentzian NMR lineshape. The resonances of ^{31}Mg and ^{8}Li are of high quality (Fig. 5.1, [30]) allowing lineshape analysis. The latter showed that there is no detectable Gaussian component in the spectra, making a strong argument that the effect of the inhomogeneity is much smaller than the width of the resonances. The drift on the other hand, which is within the relative error of 5.5×10^{-5}, is a significant fraction of the FWHM (as much as 15 % compared to the narrowest resonances), making it the dominant source of systematic uncertainty in the NMR measurements. The final results for ^{29,31}Mg are presented in Tab. 5.2. The error in the square brackets is the systematic uncertainty, which is comparable with the statistical error only for the high-precision moment of ^{31}Mg and negligible in the case of ^{29}Mg. The matter of finding the total probability density distribution rising from the statistical and systematic uncertainties is extensively discussed in Appendix A.1. Tab. A.1 contains confidence levels associated with a total error on the ^{31}Mg magnetic moment of up to $5 \times 10^{-5}\,\mu_N$. The spin-parity assignments to the ground states of ^{29,31}Mg are presented in Tab. 5.2. These are based on the β-decay work from Refs. [19, 20, 72], in the case of ^{29}Mg, and hyperfine structure and nuclear magnetic resonance measurements on both isotopes [16], which confirm

Table 5.2: Nuclear ground-state properties of ^{29,31}Mg.

	^{29}Mg	^{31}Mg
I^π	$3/2^+$	$1/2^+$
g	0.6520(4)	$-1.76710(3)[10]$
$\mu\,(\mu_N)$	0.9779(6)	$-0.88355(2)[5]$

the spin of ^{29}Mg and establish spin 1/2 for the ground state of ^{31}Mg. The case of ^{31}Mg is extensively discussed in the publications attached at the end of this dissertation [15, 30, 31]. Typical HFS and NMR spectra are presented in Fig. 5.1.

5.2 ^{31}Mg: transition to the Island of inversion

While the neutron rich Mg isotopes up to ^{30}Mg are well understood in their ground states within the *sd* shell model[A], ^{31}Mg is the first one in the chain with ground-state properties incompatible with that description. Having four protons and eleven neutrons above the core of ^{16}O, ^{31}Mg was originally expected to have a ground-state configuration according to the subsequent filling of the orbitals forming the *sd* shell - $\nu\, 1d_{5/2}$, $\nu\, 2s_{1/2}$ and $\nu\, 1d_{3/2}$. In this picture the ground-state is largely determined by the odd neutron in the $\nu\, d_{3/2}$ orbital, demanding spin and parity $I^\pi = 3/2^+$ and a single-particle magnetic moment close to the Schmidt value $\mu = 1.15\,\mu_N$. Contrary to this concept the experimental spin is $I = 1/2$ [15][B]. Moreover, the magnetic moment has the opposite sign (see Tab. 5.2). The spherical shell model could account for such behavior only by promoting two neutrons to the *pf* shell. Large-scale shell-model calculations described in Ref. [15] show that the lowest 2p-2h configuration does indeed have the correct spin and magnetic moment close to the experimental value, making a strong argument that the ground state of ^{31}Mg is a pure intruder state. Under this description the largest fraction of the wave function involves a single neutron on the $\nu\, s_{1/2}$ orbital with Schmidt value $\mu = -1.91\,\mu_N$, which gives a simplified explanation of why the spin is 1/2 and the magnetic moment is negative. However, the magnitude of the magnetic moment can only be understood within the full calculations, since the wave function is rather mixed being considerably influenced also by the positive single-particle g factor of the $\nu\, d_{3/2}$ orbital. Another qualitative picture comes from the fact that the calculated g factor of the $1/2^+$ state in ^{29}Mg with the USDB interaction (Tab. 5.10) is very close to the experimental value for the ^{31}Mg ground state (Tab. 5.2), giving an indication that the two neutrons in the *pf* shell are mostly coupled to zero angular momentum and it is mainly the proton-neutron arrangement within the *sd* shell that determines the ground-state properties of ^{31}Mg. The fact that in the calculations presented in [15] the 2p-2h states are higher in energy than the 0p-0h and 1p-1h configurations is directly related to the size of the $N = 20$ shell gap, which appears to be strongly reduced for the Mg isotopes. In the Nilsson model pic-

[A] The cases of ^{27,29}Mg are developed in Sections 4.2 and 5.5, respectively. These will be the main subjects of Ref. [33]. ^{29}Mg is extensively described in Ref. [16]. ^{30}Mg is placed outside the Island of inversion according to Ref. [73].

[B] Included at the end of this dissertation.

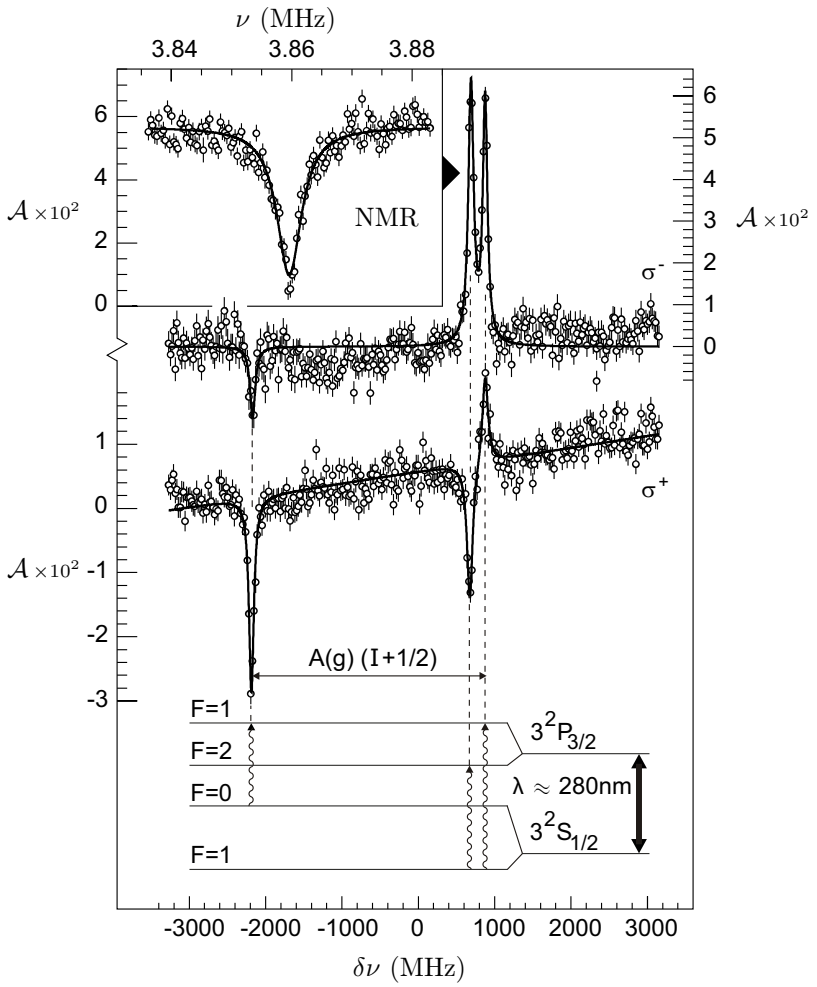

Figure 5.1: HFS of ^{31}Mg II in the D_2 line and NMR in the strongest transition. Notice that the labels $\sigma^{\pm}$ are inverted compared to those in Refs. [15, 16, 31], where they are wrongly assigned.

ture the ground state of ^{31}Mg is associated with a large prolate deformation based on the 1/2 [200] orbital. The odd-neutron occupation is represented by the segment (a) in Fig. 5.4.

The complete resemblance of the experimental spectra of ^{31}Mg in Fig. 5.1 with the theoretical simulations in Fig. 3.12 proves that the β-asymmetry pa-

rameter of ^{31}Mg is negative. This conclusion is based on the fact that the theoretical procedure described in Section 3.8 yields the nuclear polarization, which in turn must be multiplied by the β-asymmetry parameter A_β to obtain the observable experimental β asymmetry (2.63). The simulated spectra are drawn under the condition $A_\beta = -1$, thus proving that the polarization must be inverted in order to reproduce the experimental spectra. From the measured branching ratios for populating excited states in ^{31}Al via the β decay of ^{31}Mg [54], using the rules in Tab. 2.1 one calculates $A_\beta = -23\,\%$, which is consistent with the considerations above. However, the latter calculation strongly depends on the spin assignments to the states in ^{31}Al, which are partly established through a comparison with shell-model calculations.

^{31}Mg is the first isotope in the chain with an intruder ground state. The strong impact on the nuclear structure understanding in the vicinity of the Island of inversion, drawn from data of exceptional quality, highlights ^{31}Mg as one of the emblematic cases in the region.

5.3 Spin and magnetic moment of ^{33}Mg

The central results of the present doctoral dissertation, namely the spin and magnetic moment of ^{33}Mg, are discussed in this section. The following text contains a description of the analysis procedures and an interpretation of the results, consistent with all available studies of this nucleus. An alternative discussion is presented in a publication in preparation [32] the full text of which is included at the end of this thesis.

Inside the Island of inversion different particle-hole excitations coexist at low energies, making it difficult to predict which configuration will become the ground state. This information needs to be obtained experimentally. A β-decay study of ^{33}Na [25] suggests a 1p-1h configuration for the ^{33}Mg ground state with spin and parity $I^\pi = 3/2^+$ in contrast to $I^\pi = 5/2^+$ (also 1p-1h) from intermediate energy Coulomb excitation [26] and proton inelastic scattering [27] experiments. The systematics of the nuclear moments in the region [28], on the other hand, is consistent with 2p-2h ground states. Theoretical and experimental studies of the neighboring even-even Mg isotopes [9, 10, 21, 24] support this observation. The above discrepancy in the ground-state spin assignment of ^{33}Mg and the diminishing predictive power of the shell model in the Island of inversion serve as a primary motivation for the experimental investigations described below.

The experimental studies are realized in the D_2 line (279.635(78) nm for Mg [56]), which involves the transitions from $3^2S_{1/2}$ to $3^2P_{3/2}$ hyperfine multiplets, shown in Figs. 5.2 (a) and (e). The experimental spectra of ^{33}Mg II, obtained with $\sigma^\mp$ laser polarization are displayed in Figs. 5.2 (b) and (c), respectively. The frequency scale is given relative to the fine-structure splitting of the refer-

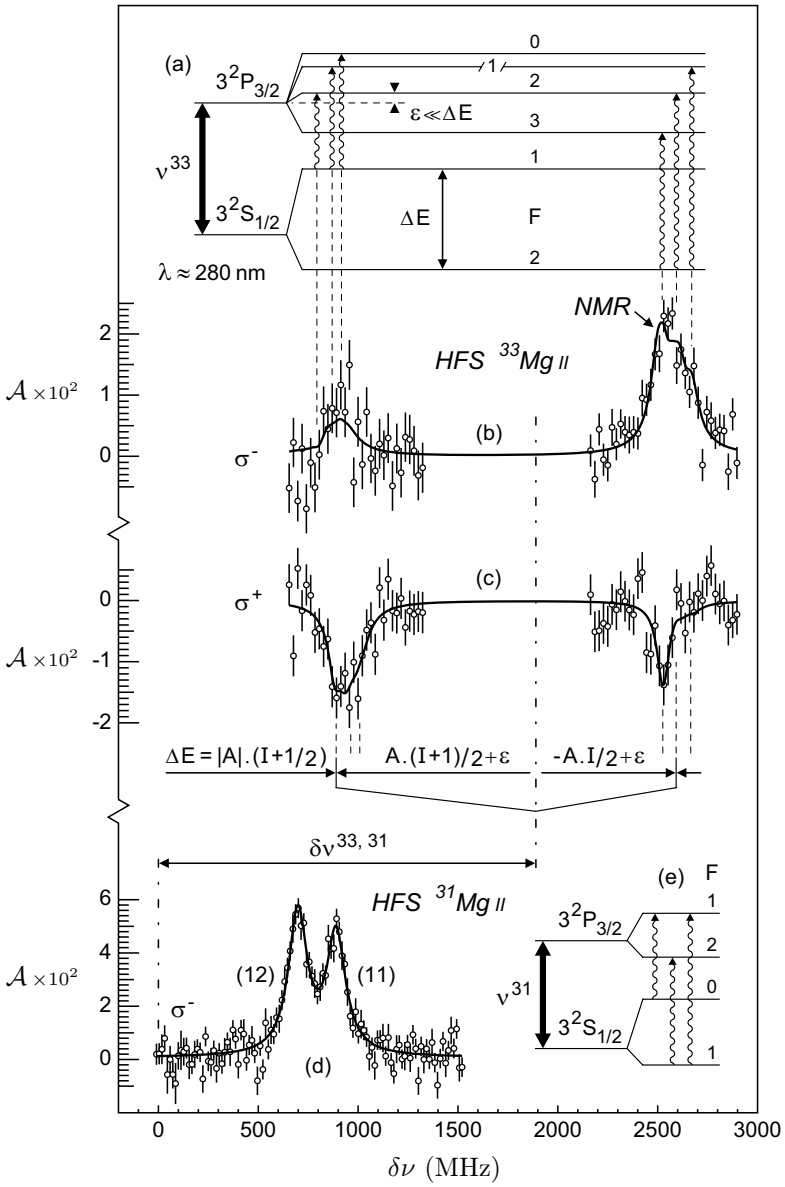

Figure 5.2: (a) Principle hyperfine structure in the D_2 line for $I = 3/2$ and $A < 0$; (b), (c) Realistic fits of the β-asymmetry spectra of $\sigma^{\mp}$ polarized ^{33}Mg II after implantation into MgO; (d) β-asymmetry spectrum of σ^- polarized ^{31}Mg II in D_2 implanted into MgO; (e) HFS scheme corresponding to (d);

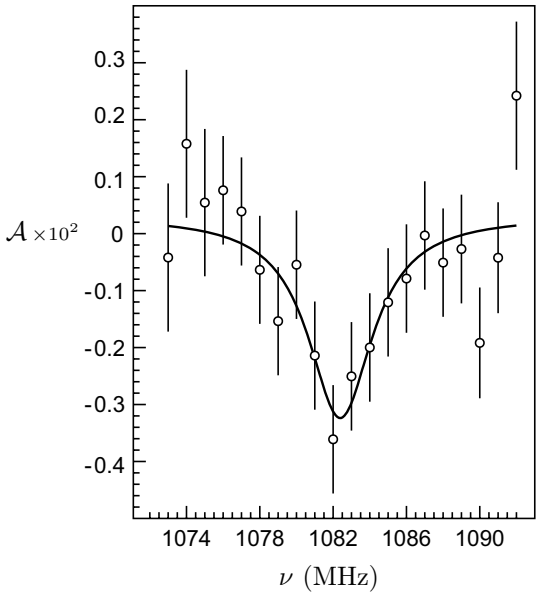

Figure 5.3: NMR spectrum of ^{33}Mg in MgO (zoom of Fig. A.3 (b)).

ence ^{31}Mg II ($I = 1/2$) [15]. The distance between the two groups of resonances in ^{33}Mg II is determined by the splitting ΔE in the $3^2S_{1/2}$ multiplet. This direct observable is a function of the nuclear spin and the magnetic dipole hyperfine parameter: $\Delta E = |A|\,(I + 1/2)$. Neglecting the hyperfine anomaly, the ratio A/g, where g is the nuclear g factor, is constant for all the isotopes in the chain. This ratio can be calculated from the experimental A and g available for the stable ^{25}Mg II ($I = 5/2$) [64, 66]. A g-factor measurement is therefore sufficient to extract the hyperfine parameter of ^{33}Mg II and unambiguously determine the nuclear spin from the measured hyperfine splitting. Magnetic resonance measurements are carried out with σ^- laser polarization in the higher frequency triplet of transitions, as indicated in Fig. 5.2 (b), after implantation in the cubic crystal lattice of MgO (fcc)[A] or Pt (ccp)[B]. The produced experimental asymmetry is $\approx 2\,\%$. A radio-frequency field of a few tenths of a mT is applied perpendicular to the static magnetic field $B \approx 0.3$ T. An example NMR spectrum of ^{33}Mg in MgO obtained with a small circular frequency modulation with an amplitude of 1 kHz is presented in Fig. 5.3. The total statistics includes spectra of similar quality in Pt. All independent measurements are presented

[A] fcc - face centered cubic.
[B] ccp - cubic close packed.

Table 5.3: NMR frequencies of ^{33}Mg in Pt and MgO, corresponding to the magnetic field during the reference measurements from Tab. 5.7, and the g-factor ratio $g(^{33}\mathrm{Mg})/g(^{31}\mathrm{Mg}) = \nu(^{33}\mathrm{Mg})/\nu(^{31}\mathrm{Mg})$.

	Pt	MgO
$\nu(^{33}\mathrm{Mg})$ (kHz)	1084.22(76)	1082.41(42)
$g(^{33}\mathrm{Mg})/g(^{31}\mathrm{Mg})$	0.28159(20)	0.28121(11)

in Appendix A.2 together with detailed information on the analysis procedure. The reference probe ^{31}Mg [15] was implanted in both hosts in order to extract the ratio of the Larmor frequencies (2.54), which is independent of the chemical and Knight shifts. The results are presented in Tab. 5.3, which contains two independent values of the ratio $g(^{33}\mathrm{Mg})/g(^{31}\mathrm{Mg})$. Their weighted mean is used to calculate the g factor of ^{33}Mg based on the reference ^{31}Mg (Tab. 5.2). The g factor in combination with the hyperfine splitting determines nuclear spin $I = 3/2$. The ground-state properties of ^{33}Mg are summarized in Tab. 5.4. Since the systematic uncertainty is significantly smaller than the statistical error, the total error is formed as the sum of the two, yielding the final result $|\mu| = 0.7456(5)\,\mu_N$. The confidence level associated with the latter uncertainty is $\approx 76\,\%$, as presented in Tab. A.2.

The experimental HFS spectra in Figs. 5.2 (b) and (c) are fitted with the theoretical polarization function, described in Section 3.8. The actual fitting has the main purpose of demonstrating the consistency between theory and experiment. Due to the low resolution and power broadening, the nuclear quadrupole moment and β-asymmetry parameter can not be extracted. However, there are important conclusions to be drawn from the realistic polarization function, namely the negative signs of the magnetic hyperfine parameter and the β-asymmetry parameter. The latter is perhaps easier to comprehend by comparing the experimental with the simulated spectra in Fig. 3.14 ($A < 0$, $A_\beta < 0$). A change in the sign of A would invert left and right and a sign change of A_β inverts up and down.

There is an independent way to confirm the negative sign of the hyperfine parameter. With the use of the total mass shift from Ref. [16] one estimates the isotope shift $\delta\nu^{33,31} = 1867$ MHz. The uncertainty on this number, including

Table 5.4: Nuclear ground-state properties of ^{33}Mg.

$I = 3/2$	$g = -0.4971(3)[1]$	$\mu = -0.7456(4)[1]\,\mu_N$

Table 5.5: Gyromagnetic ratios and quadrupole moments of different particle-hole excitations in ^{33}Mg ($I = 3/2$), calculated with the interactions WBMB [3] and SD - PF [74]. Free-nucleon g factors and effective charges $e_\pi = 1.5e$ and $e_\nu = 0.5e$ are used.

		WBMB		SD - PF	
$n\,\hbar\omega$	I^π	g_{free}	Q (mb)	g_{free}	Q (mb)
0	$3/2^-$	-1.47	-83	-1.35	-91
1	$3/2^+$	0.75	135	0.78	140
2	$3/2^-$	-0.45^a	147^b	-0.47^a	157^b

[a] Experimental gyromagnetic ratio from this work $g = -0.4971(3)[1]$ (see Tab. 5.4).
[b] $Q(\beta_C) = 151(38)$ mb, calculated from β_C (see the text).

the errors on the mass shift and an unknown change between the mean-square charge radii, is estimated to be smaller than 50 MHz, which can be neglected for the considerations below. Based on the isotope shift one can plot the fine-structure splitting of ^{33}Mg II relative to the transitions of the hyperfine structure, the so-called "center of gravity". The latter is represented by the alternating dash-dot line in Fig. 5.2. Closer to the center of gravity are always the transitions starting from the higher angular momentum state $F = I + 1/2$, which can be verified with the aid of (2.31). In the case of ^{33}Mg II their resonances appear at the higher frequency side of the spectra, revealing that they start from the lower energy level. The higher angular momentum states are lower in energy only for a negative magnetic hyperfine parameter (2.31). Since the ratio A/g is positive for all alkali-like atoms [42], the ground-state nuclear magnetic moment of ^{33}Mg is negative. The sign of the A factor is demonstrated in Fig. 5.2, where the relative energies of the hyperfine-structure levels in $3^2S_{1/2}$ are represented by the vectors $A(I+1)/2+\varepsilon < 0$ and $-AI/2+\varepsilon > 0$ ($|\varepsilon| \ll |A|$). Their direction towards the frequency axis demands $A < 0$.

The ground-state of $^{33}_{12}\text{Mg}_{21}$ is suggested in Ref. [25] to have a 1p-1h intruder configuration, with spin and parity $I^\pi = 3/2^+$. In the extreme shell-model picture the properties of such a state are determined by an odd neutron in the $\nu\,1d_{3/2}$ orbital with a positive single-particle magnetic moment (2.7). In order to explain the negative sign of μ, an odd number of neutrons must occupy the pf shell, as these have negative Schmidt values for the orbitals $\nu\,1f_{7/2}$ and $\nu\,2p_{3/2}$. The parity of such states is negative, thus providing evidence for a negative ground-state parity of ^{33}Mg. Large-scale shell-model calculations are carried out in the $sd-pf$ model space with the code Oxbash [69], using the Hamiltonians [3, 74] designed particularly to describe the Island of inversion. Mixing of states with a different number of particle-hole excitations ($\hbar\omega$) is not considered. The neutron configuration space is reduced to $\nu\,(sd-1f_{7/2}-$

Table 5.6: Energy levels of ^{33}Mg, calculated with the interactions WBMB [3] and SD - PF [74]. The configuration denoted with $\langle\star\rangle$ is identified as the ground state (see Tab. 5.5).

	$n\,\hbar\omega$	I^π	$E_{\mathrm{WBMB}}{}^a$ (keV)	$E_{\mathrm{SD-PF}}{}^a$ (keV)	
	0	$1/2^-$	2417^{11}	4490^{12}	
	0	$3/2^-$	737^{3}	2374^{10}	
	0	$5/2^-$	1894^{9}	4284^{11}	
	0	$7/2^-$	0^{1}	1710^{6}	
	1	$1/2^+$	2082^{10}	1921^{8}	
	1	$3/2^+$	399^{2}	283^{2}	
	1	$5/2^+$	1238^{5}	1187^{5}	
	1	$7/2^+$	1554^{8}	1738^{7}	
	2	$1/2^-$	3232^{12}	2298^{9}	
$\star$	2	$3/2^-$	1065^{4}	0^{1}	$\star$
	2	$5/2^-$	1327^{6}	403^{3}	
	2	$7/2^-$	1481^{7}	681^{4}	

^{a}The top energy index denotes the level ordering.

$2p_{3/2}$). Two out of four valence protons are fixed in the $\pi\,1d_{5/2}$ orbital. The other two are confined within the *sd* shell. Calculated nuclear moments of 0, 1 and $2\,\hbar\omega$ excitations for $I = 3/2$ are presented in Tab. 5.5. Clearly, the experimental g factor is only consistent with the 2p-2h configuration. The good agreement between the experimental and theoretical magnetic moments, demonstrated in Tab. 5.5, indicates that the ground state of ^{33}Mg is a nearly pure 2p-2h intruder. Indeed, the 2p-2h $3/2^-$ level is the lowest in the calculation with the SD - PF Hamoltonian from Ref. [74], as shown in Tab. 5.6. The theoretical calculations presented Tabs. 5.5 and 5.6 demonstrate an important fact. While the excitation energies of corresponding states computed with the two Hamiltonians are very different from each other, their nuclear moments are rather consistent, highlighting the relevance of comparing experimental moments with theory.

The charge and matter deformations of ^{33}Mg are experimentally determined to be $\beta_{\mathrm{C}} = 0.52(12)$ [26] and $\beta_{\mathrm{M}} = 0.47(8)$ [27], which appear to be consistent with the deformation parameters of the neighboring even-even ^{32,34}Mg [10, 21, 23, 24]. One can use β_{C} to evaluate the spectroscopic quadrupole moment of ^{33}Mg through (2.16), (2.17) and (2.22) for $I = K = 3/2$. Hence, under the assumption of an axial symmetry the result is $Q = 151(38)$ mb. This value is in agreement with the established 2p-2h configuration, as demonstrated in Tab. 5.5.

In the frame of the Nilsson model the established spin and parity of ^{33}Mg

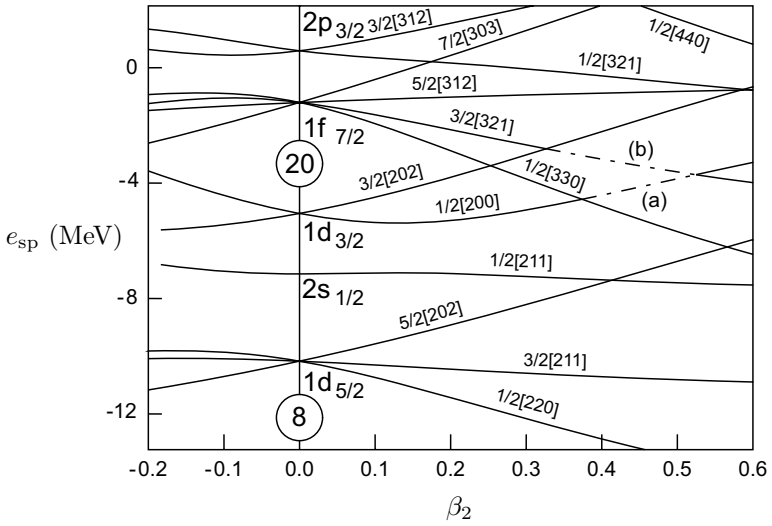

Figure 5.4: Nilsson diagram in the $\nu\,(sd-1f_{7/2}-2p_{3/2})$ configuration space. The segments (a) and (b) represent the odd neutron occupation in the ground states of ^{31,33}Mg, respectively.

($I^\pi = 3/2^-$) are consistent with a large prolate deformation and ground-state properties determined by a single-particle occupation of the $3/2\,[321]$ orbital - the segment (b) in Fig. 5.4. This range is consistent with the deformation of ^{31}Mg, as suggested in Ref. [15], represented in Fig. 5.4 by the segment (a) of the $1/2\,[200]$ orbital. It is relevant to support these findings by comparing the experimental magnetic moments with calculated values from the Nilsson model. This requires a knowledge on the composition of the Nilsson wave functions. Since the configuration mixing coefficients are not available one can roughly estimate which spherical states contribute the most by looking at Fig. 5.4. Thus, large fractions of $\nu\, f_{7/2}$ and $\nu\, p_{3/2}$ are expected into the single-particle wave function of the odd neutron in ^{33}Mg and therefore a single-particle g factor (2.21) in between the corresponding Schmidt values (divided by j)[A]. With the use of (2.19) one calculates the expectation boundaries for the nuclear magnetic moment of ^{33}Mg to be $-0.27 \leq \mu(^{33}\mathrm{Mg})/\mu_N \leq -0.93$. Although this estimate is very rough, it correctly reproduces the sign and the magnitude of the magnetic moment (Tab. 5.4), thus independently supporting the establishment of the nuclear deformation according to the segment (b) of the $3/2\,[321]$ orbital. In the case of ^{31}Mg, with $I = 1/2$, the magnetic moment depends additionally

[A] The single-particle g factors are obtained by dividing the Schmidt values (2.7) to the total angular momentum quantum number j of the spherical state.

on the *magnetic decoupling parameter* b [2] (2.20). Taking into account the contribution of $\nu\, s_{1/2}$ and $\nu\, d_{3/2}$ to the prolate side of the $1/2\,[200]$ orbital, one calculates the boundaries for the magnetic moment of ^{31}Mg to be $-1.7 \leq \mu(^{31}\mathrm{Mg})/\mu_N \leq -0.17$, being consistent with the experimental value in Tab. 5.2.

The results from studying the β-decay of ^{33}Na, as described in Ref. [25], are summarized in Fig. 5.5. The obtained branching fractions with the corresponding $\log ft$ values, as well as tentative spin-parity assignments based on large-scale shell-model calculations are presented next to the level scheme. The existence of the 159 keV level appears to be an unsettled feature of the scheme. This state is suggested to be an isomer, since its decay to the ground state has not been observed within a β-γ coincidence window of 500 ns.

The conclusions from the β-decay work have not been supported by Coulomb excitation [26] and proton inelastic scattering [27] experiments. The latter two studies consistently provide evidence that the parity of the 484 keV level is identical to the parity of the ground state. This level is suggested in Ref. [26] to be a rotational excitation, thus having one unit of angular momentum higher than the ground state and a similar intrinsic structure. Since the 546 keV gamma has only been detected in the neutron knockout reaction ^{1}H(^{34}Mg, ^{33}Mg$\,\gamma$) and not in the proton inelastic scattering process ^{1}H(^{33}Mg, ^{33}Mg$\,\gamma$), described in Ref. [27], it is concluded that this transition originates from a state with a parity opposite to the parity of the ground state. These experimental facts contradict with Ref. [25] (Fig. 5.5). In the context of the firm spin-parity assignment to the ground state $I^\pi = 3/2^-$ established in the present work, the experimental results from Refs. [25–27] allow to propose a modified level scheme, as presented in Fig. 5.6 (see the text below). In order to have an isomeric state at 159 keV, with a lifetime longer than 500 ns, an angular momentum of at least two units larger than the one of the ground state is required, demanding a spin assignment $I = (7/2)$. If the 484 keV level

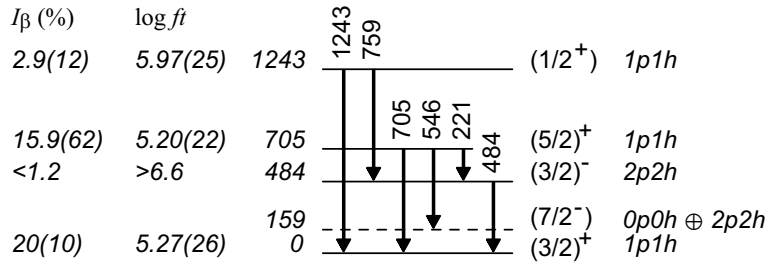

Figure 5.5: ^{33}Mg level scheme, established in the β decay of ^{33}Na, with tentative spin-parity assignments according to Ref. [25]. The 159 keV level is not experimentally observed.

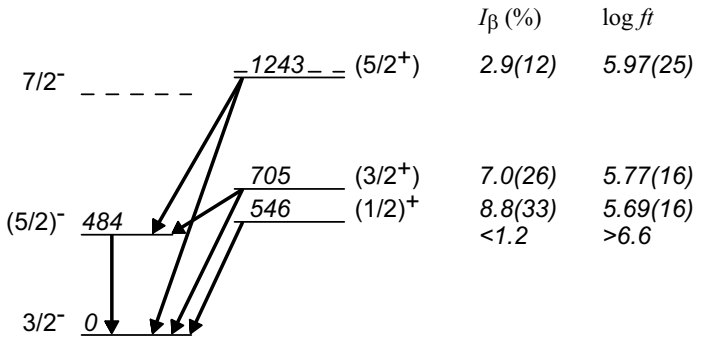

Figure 5.6: Modified decay scheme of ^{33}Mg with suggested spin-parity assignments, based on the firm assignments to the ground state.

has one unit higher angular momentum than the ground state and the same parity, resulting in spin-parity assignment $I^\pi = (5/2)^-$, the transition to the isomeric state should also be observed, since it would have the same multipolarity ($L = 1$) as the transition to the ground state. It is therefore more likely that the 546 keV gamma is associated with a state at that energy, not a decay to an isomeric state. The branching fractions to the 705 keV and 546 keV levels, presented in Fig. 5.6, are recalculated, based on the γ intensities from Ref. [25]. The error on the log ft values to these states includes the uncertainties on the branching ratios and the half-life of ^{33}Na. The uncertainty on the electrons kinetic energy is not taken into account. The large feeding to the ground state of ^{33}Mg suggested in Ref. [25] (Fig. 5.5) is unlikely, considering a first forbidden β transition. Here ^{33}Na is regarded as having $3/2^+$ or $5/2^+$, either 0p-0h or 2p-2h ground state, based on analogy with ^{31}Na ($I^\pi = 3/2^+$ [6]) and shell-model calculations [25]. An indirect confirmation of this assertion comes from the fact that the 484 keV level, which has a negative parity, is weakly fed in the β decay.

The most likely interpretation of the available experimental evidence is that the observed excited states in ^{33}Mg rise from two rotational bands - one based on a single-particle state with $K^\pi = 3/2^-$ ($3/2\,[321]$) and another with $K^\pi = 1/2^+$ ($1/2\,[200]$). This interpretation would explain the spin change between ^{31}Mg ($I^\pi = 1/2^+$) and ^{33}Mg ($I^\pi = 3/2^-$) with a relative movement of the two bands when adding two neutrons. In the case of $K^\pi = 3/2^-$, with the use of (2.18), one can calculate the moment of inertia and consequently the energy of the next member of the band. The result is $E_{K=3/2}(I = 7/2) = 1162$ keV. In the case of $K^\pi = 1/2^+$, using the theoretical value for the decoupling parameter $a_{\beta=0.4} = -0.615$ from Ref. [2] (vol. 2,

p. 290), one calculates $E_{K=1/2}(I = 5/2) = 1271$ keV. In both cases the computed energies are close to the experimental level at 1243 keV, as it is demonstrated in Fig. 5.6, where the calculated energies are represented by the dashed lines. Since the $\log ft$ value associated with the 1243 keV level is relatively low, one tends to assign this state to the band with $K^\pi = 1/2^+$. However, belonging to the other band is not completely excluded. The tentative spin-parity assignments in Fig. 5.6, proposed according to this interpretation, are consistent with the recalculated $\log ft$ values.

Recent results on the β decay of ^{33}Mg are presented in Ref. [75]. The ground-state spin and parity of the daughter ^{33}Al are known to be $I^\pi = 5/2^+$ (mostly 0p-0h configuration), derived through a comparison of shell-model calculations with a g factor measurement [17]. Inelastic nuclear scattering [76] further suggests spin parity-assignment $I^\pi = 5/2^+$ (2p-2h configuration) to the observed excited state at 730(50) keV. In the β decay of ^{33}Mg no feeding to states below 1.6 MeV has been detected, which is consistent with the conclusions of the latter two studies since the $5/2^+$ levels would be populated from the $3/2^-$ ground state of ^{33}Mg with first forbidden β transitions. The nuclear structure of the excited states in ^{33}Al above 1.6 MeV is unknown. The large feeding to these levels needs to be understood in the context of the present work.

5.4 Solid-state aspects of NMR

NMR measurements of ^{33}Mg were performed in two cubic crystals - Pt (ccp) and the MgO (fcc). The magnetic field in both hosts was calibrated by the NMR resonances of ^{31}Mg, yielding the Knight shift of Mg in Pt. The Knight shift was calculated from the frequencies, given in Tab. 5.7, by solving the system:

$$\left| \begin{array}{ll} h\,\nu_{\mathrm{MgO}} = g\,\mu_N\,B_0\,(1-\sigma_{12}) \\ h\,\nu_{\mathrm{Pt}} \quad = g\,\mu_N\,B_0\,(1-\sigma_{10}+K)\,, \end{array} \right. \tag{5.1}$$

where g and B_0 represent the nuclear g factor and the external magnetic field and σ_{12} and σ_{10} account for the diamagnetic shielding of the localized electrons in the two hosts. Since the valence electrons in a metal are no longer

Table 5.7: NMR frequencies of ^{31}Mg in Pt and MgO crystals and the Knight shift of Mg in Pt.

ν_{Pt} (kHz)	ν_{MgO} (kHz)	K
3850.40(16)	3849.05(20)	$3.4(7) \times 10^{-4}$

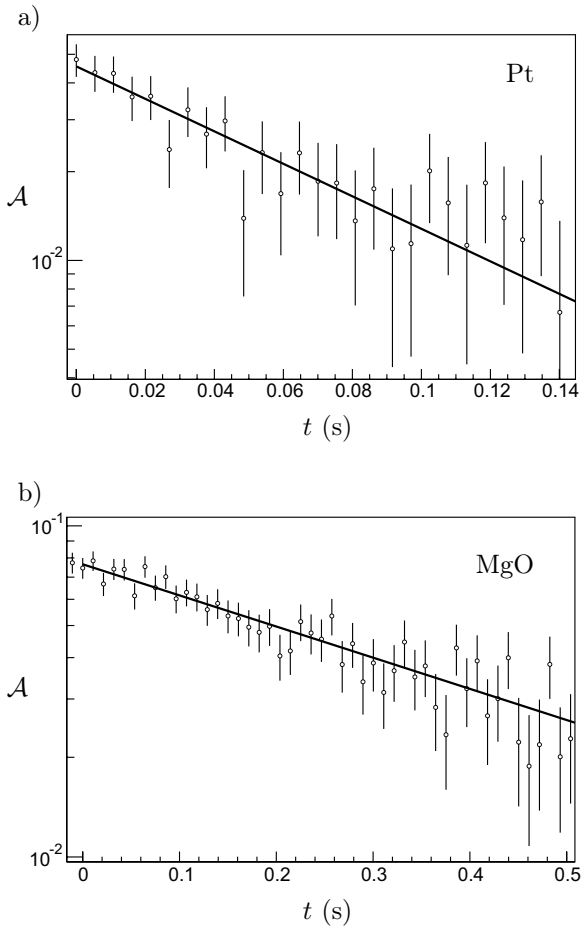

Figure 5.7: Relaxation times of ^{31}Mg in Pt and MgO at room temperature.

localized they will only contribute to the Knight shift. Theoretical values for the shielding factors σ_{12} and σ_{10} are given in Refs. [60, 77]. The temperature dependence of the spin-lattice relaxation (SLR) time T_1 in metals is given by:

$$T_1\,T = \frac{\hbar}{K^2 g^2 (m_e/m_p)^2 k\,\pi}\,, \tag{5.2}$$

known as the *Korringa relation* [78]. The constant factor on the right side is determined by the nuclear g factor and the Knight shift. Example spectra of ^{31}Mg relaxation in Pt and MgO crystals are shown in Fig. 5.7 and the results of both sets of measurements are presented in Tab. 5.8. With the use of

Table 5.8: Relaxation times of ^{31}Mg in Pt and MgO at room temperature and external magnetic field $B = 0.28596(3)$ T.

	Pt	MgO	
T_1 (ms)	80(8)	395(63)	$T = 293(5)$ K
$T_1\,T$ (Ks)	23.4(23)	116(9)	

(5.2) and the experimental g and K from Tab. 5.2 and Tab. 5.7 one calculates $T_1 = 80(32)$ ms. This value is in agreement with the direct determination of the asymmetry decay constant in Pt at room temperature, presented in Tab. 5.8. The quantity $T_1\,T\,g^2$, according to (5.2), should be isotope independent, as long as the Knight shift is isotope independent. However, measurements of the SLR of ^{23}Mg in Pt, reported in Ref. [79], established $T_1\,T\,g^2(^{23}\mathrm{Mg}) = 213(18)$ Ks, to be compared with the present result $T_1\,T\,g^2(^{31}\mathrm{Mg}) = 73(7)$ Ks. The latter difference can not be attributed to a field dependence of T_1 since the measurements performed at 0.27 T and 0.4 T, described in Ref. [79], are consistent. Another possibility is a different orientation of the host crystal in respect to the external field in the two experiments (see Ref. [48]). The above discrepancy is not understood until now.

5.5 Quadrupole moment of ^{29}Mg

The level scheme of ^{29}Mg is established in the β-decay of ^{29}Na [19, 20, 80]. The ground-state spin-parity assignment $I^\pi = 3/2^+$ [19, 20, 72] is based on experimental branching fractions to known states in ^{29}Al. The hyperfine structure and nuclear magnetic resonance measurements on ^{29}Mg II, described in Refs. [16], determine the nuclear magnetic moment and independently confirm the spin. The sign of the magnetic moment, as in the cases of ^{31,33}Mg, is an experimental fact based on the hyperfine structure. The results are summarized in Tab. 5.2. The possibilities for extracting additional information from the hyperfine structure, namely the quadrupole moment and ground-state deformation, are discussed in this section. The experimental spectra of ^{29}Mg II in the D_2 line strongly resemble the theoretical curves plotted in Fig. 3.10. The β-asymmetry parameter $A_\beta = 15\,\%$, substituted in the simulations, is calculated from the branching fractions in Ref. [53] with the use of Tab. 2.1. The experimental β asymmetry in Fig. 5.8 is a factor of two smaller than the prediction from the theoretical function. The major reason is perhaps the long half-life $\tau_{1/2} = 1.30(12)$ s [19, 20, 81], comparable with the relaxation time $T_1(^{29}\mathrm{Mg}) = 0.59(23)$ s in MgO at room temperature, calculated with use of

Table 5.9: Quadrupole hyperfine parameter of ^{29}Mg II in $3^2S_{3/2}$, obtained with the use of the realistic polarization function (R) and Lorentz profiles (L), with the corresponding quadrupole moments and deformation parameters.

			$K = 1/2$		$K = 3/2$	
	B (MHz)	Q (mb)	Q_0 (mb)	β	Q_0 (mb)	β
R	−23.2(22)	−195(20)	975(100)	0.58(6)	−975(100)	−0.73(9)
L	−15.1(19)	−126(17)	630(85)	0.39(5)	−630(85)	−0.45(7)

(5.2). The cluster of the lower energy transitions with σ^+ laser polarization gives the highest experimental asymmetry and relative amplitudes suitable for extraction of the hyperfine parameters of the excited state. The positions of the three lines (two energy gaps) completely determine the A and B factors. This is one of the experimental evidence for the positive sign of the A factor and consequently the positive magnetic moment. The independent experimental spectra are fitted with the realistic polarization function from Appendix B.3 and using the natural lineshape (3.48). The two fit functions can be compared in Figs. 5.8 (a) and (b). The value of A is obtained independently through the relation (2.33) and substituted as a constant parameter. At low laser power the transition $F : 2 \rightarrow 2$ is the strongest (Fig. 3.10). The fact that experimentally it is weaker than the transition $F : 2 \rightarrow 3$ is evident for oversaturation and simultaneous optical pumping in the neighboring transitions. These effects are also causing the broadening and change in the lineshape of the middle resonance. While the theoretical curve reproduces well these experimental features it fails to account precisely for the relative asymmetry in the transition $F : 2 \rightarrow 1$. The fit function in Fig. 5.8 (b) is a sum of three Lorentzian profiles with amplitudes set as free parameters. This simple approach is unable to account for pumping in multiple transitions. Thus, the Lorentzian profiles become too broad and the transitions in the fit function less resolved than they are experimentally. As a result both fitting procedures converge to a similar χ^2. The obtained values for the B parameter are given in Tab. 5.9. The large discrepancy in the two numbers signifies the importance of the line profiles for the analysis of optical and polarization spectra. It will be postulated here that the difference in the obtained B factors is a measure for the systematical uncertainty associated with the choice of the fitting function. Thus, with the use of (2.34) and the quadrupole moment of ^{25}Mg from Ref. [82], one calculates an expectation range for the spectroscopic quadrupole moment $Q \sim \big(-195(20)\text{ mb}\,,\,-126(17)\text{ mb}\big)$. Such an inaccurate estimate is expected to have a minor impact on the understanding of the nuclear structure of ^{29}Mg. However, one can state with confidence that the sign of the quadrupole moment is negative as well as quantitatively estimate the nuclear deformation, using relations (2.22) and (2.16).

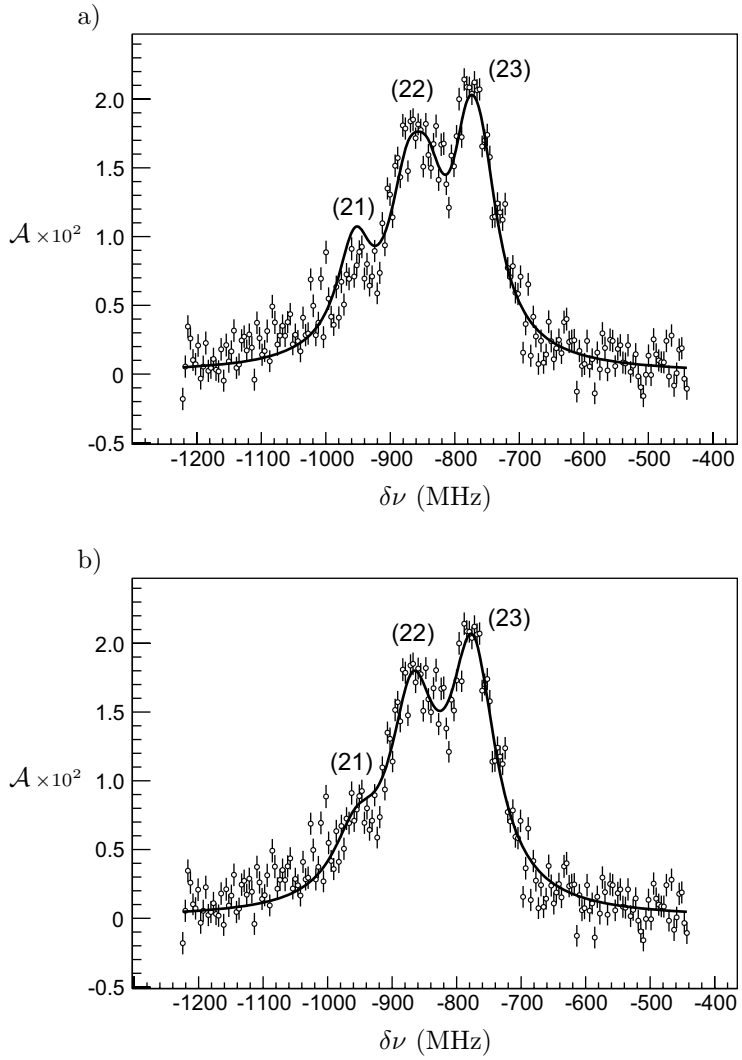

Figure 5.8: The cluster of lower energy transitions within the hyperfine structure of ^{29}Mg II ($I = 3/2$, $A > 0$) in the D_2 line fitted with: (a) The realistic polarization function from Appendix B.3; (b) Lorentzian profiles;

The results are presented in Tab. 5.9.

In the particle plus rotor model the ground state of ^{29}Mg, with spin and parity $I^\pi = 3/2^+$, is built on a single-particle state, based either in the $3/2\,[202]$ or $1/2\,[200]$ Nilsson orbitals (Fig. 5.4). The second option requires a decoupling

Table 5.10: Gyromagnetic ratios and quadrupole moments of the two lowest states in ^{29}Mg, calculated with the interactions USD [70] and USDB [83]. Free-nucleon g factors and effective charges $e_\pi = 1.5e$ and $e_\nu = 0.5e$ are used.

	USD			USDB		
I^π	E (keV)	g_{free}	Q (mb)	E (keV)	g_{free}	Q (mb)
$1/2^+$	0	-2		45	-1.65	
$3/2^+$	40	0.64^a	-109^b	0	0.71^a	-110^b

[a] Experimental gyromagnetic ratio from this work $g = 0.6520(4)$ (see Tab. 5.2).
[b] $Q \sim \big(-195(20)$ mb , $-126(17)$ mb$\big)$ (see the text).

parameter $a < -1$ in order to invert the energies of the first two members of the rotational band and have the $3/2^+$ state as the ground state. Even precisely known, the spectroscopic quadrupole moment is not associated with a particular intrinsic deformation. This is clearly demonstrated in Tab. 5.9, where under the assumption of different K one arrives with either positive or negative β. The study presented in Ref. [72] suggest prolate ground-state deformation. Under this condition the two lowest levels in ^{29}Mg, according to the estimates in Tab. 5.9 for $K = 1/2$, are associated with deformation similar to the one of ^{31}Mg. This supports the earlier argument that similar magnetic moments are to be expected for the first excited state in ^{29}Mg and the ground state of ^{31}Mg.

Shell-model calculations are carried out in the *sd* model space with the code Oxbash [69], using the Hamiltonians USD [70] and USDB [83]. The results for the two lowest levels in ^{29}Mg are presented in Tab. 5.10. The USD interaction generates a g factor closer to the experimental value (Tab. 5.2), but fails to account for the inversion of the two states. The USDB interaction is successful in predicting the correct level ordering. It also suggests a g factor for the $1/2^+$ level close to the experimental value of the ground state in ^{31}Mg. There a is strong experimental evidence that negative parity states occur in ^{29}Mg already close to 1 MeV [84, 85]. This is an indication that the orbitals of the pf shell play a role in the low-energy spectrum of ^{29}Mg. However, the magnetic moment is well reproduced within the *sd* shell, meaning that the presence of 2p-2h excitations in the ground-state wave function can be neglected. The sign of the theoretical quadrupole moment is negative, being consistent with the considerations above.

Chapter 6

Conclusions and outlook

Tab. 6.1 summarizes the experimental results presented in this dissertation. The magnetic moments of ^{27,33}Mg and the spin of ^{33}Mg are reported for the first time, completing a sequence of ground-state studies of neutron rich Mg isotopes towards the Island of inversion. Thus, laser spectroscopy in combination with nuclear magnetic resonance provide valuable probes for the development of the theoretical models in this region. The spin-parity assignments to the ground states of ^{27,29}Mg are confirmed and no influence from the orbitals of the pf shell in their wave functions is found. However, particle-hole excitations do play a role in the energy spectra of these two isotopes, since negative-parity states are found around 3 and 1 MeV, respectively [53, 84, 85]. Coulomb excitation studies [10, 73] appear to be consistent with the *sd* shell-model description of ^{30}Mg. The transition to the Island of inversion therefore occurs at ^{31}Mg, which was found to have a nearly pure 2p-2h intruder ground state [15]. The spin and magnetic moment of ^{33}Mg are the key results of this work, determining a 2p-2h ground-state configuration and correspondingly a negative parity. This result is consistent with a large prolate deformation, based on the $3/2\,[321]$ Nilsson orbital. The outcome of the present work is combined with former experimental studies [25–27, 75] under a coherent physical picture. Tentative spin-parity

Table 6.1: Spins and magnetic moments of ^{27,29,31,33}Mg.

	^{27}Mg	^{29}Mg	^{31}Mg	^{33}Mg
I^π	$1/2^+$	$3/2^+$	$1/2^+$	$3/2^-$
μ (μ_N)	$-0.4107(13)$	$0.9779(6)$	$-0.88355(2)[5]$	$-0.7456(4)[1]$
$n\,\hbar\omega$	$0\,\hbar\omega$	$0\,\hbar\omega$	$2\,\hbar\omega$	$2\,\hbar\omega$

assignments are made to the known excited states and an interpretation within the particle plus rotor model is proposed.

The ground-state spin of ^{29}Mg is consistent with an odd-neutron occupation based either on the 3/2 [202] or 1/2 [200] Nilsson orbitals. The second option demands a decoupling parameter $a < -1$ in order to invert the 1/2 and 3/2 states and arrive with the correct level ordering. Hyperfine structure measurements of ^{29}Mg II in the D_2 line are performed for the purpose of determining the nuclear spin and achieving maximum nuclear orientation for NMR measurements. These conditions are not optimal for quadrupole moment measurements due to the power broadening resulting in a poor resolution. A theoretical study of the polarization and optical lineshapes, described in Chapter 3, is beneficial for estimating the quadrupole moment under these conditions. A negative value was determined, resulting in either prolate or oblate deformation for $K = 1/2$ or 3/2, respectively, thus being consistent with the predictions from the Nilsson model. The knowledge on which is the true configuration must be extracted from other studies.

Laser spectroscopy and nuclear magnetic resonance further than ^{33}Mg are presently impossible, due to the low production rates. Optical measurements with the current apparatus demand beam intensities in the pA range. In order to extract root mean-square charge radii of nuclei close to the borderline of the Island of inversion, one must either improve the efficiency of the optical detection or combine optical with β-decay spectroscopy. Technical capabilities for applying the second alternative are currently available at COLLAPS (Fig. 3.1). However, this is a new technique in terms of data analysis. The work described in Chapter 3 is considered an important step in the development of this technique. The first alternative is by no means neglected. A recent developments on the side of ISOLDE, namely the installation of a cooling and bunching device [86], will be highly beneficial for the laser spectroscopy at COLLAPS. The bunching will remove a significant part of the laser background and the velocity spread will be reduced, improving the resolution. An off-line ion source will allow isotope-shift measurements on stable isotopes for calibration and technical improvements without interfering with other experiments.

The study of NMR lineshapes with modulation described in Section 2.6 enables the interpretation of experimental data collected under specific experimental conditions. It is another inseparable piece of work associated with the presented doctoral research.

Appendix A

Specialities

A.1 Systematic error and total probability density distribution

In this section the problem of obtaining the total probability density distribution from the distributions of the statistical and systematic uncertainties will be considered. Suppose the quantity x has the experimental value x_0 and statistical and systematic errors σ and δ, respectively. This is usually noted with $x = x_0(\sigma)[\,\delta\,]$. The probability of finding the true value in the interval $(x,\, x + dx)$ is:

$$p(x;\, x_0,\, \sigma,\, \delta)\, dx = \sum_{x'} p_\delta(x';\, x_0,\, \delta)\, dx'\, p_\sigma(x;\, x',\, \sigma)\, dx\,, \tag{A.1}$$

where $p_\sigma(x;\, x_0,\, \sigma)$ and $p_\delta(x;\, x_0,\, \delta)$ are the probability density distributions associated with σ and δ, and $p(x;\, x_0,\, \sigma,\, \delta)$ is the overall resulting distribution. The meaning of (A.1) is that the probability of finding the true value in the interval $(x,\, x + dx)$ equals to the sum over all possible values of the product of the probabilities of finding the true value in the interval $(x',\, x' + dx')$, according to one of the distributions, and of finding it in the interval $(x,\, x + dx)$ according to the other, now centered on x' (not x_0). It is straightforward to write (A.1) in the continuous case:

$$p(x;\, x_0,\, \sigma,\, \delta) = \int_{-\infty}^{\infty} p_\delta(x';\, x_0,\, \delta)\, p_\sigma(x;\, x',\, \sigma)\, dx'\,. \tag{A.2}$$

It is easy to verify that if both errors are normally distributed, according to (3.47)[A], the overall distribution is again a normal distribution with a standard

[A] Attention must payed to the fact that the Gaussian profile (3.47) is given centered around $x_0 = 0$. For the purposes in this section x must be substituted with $x - x_0$.

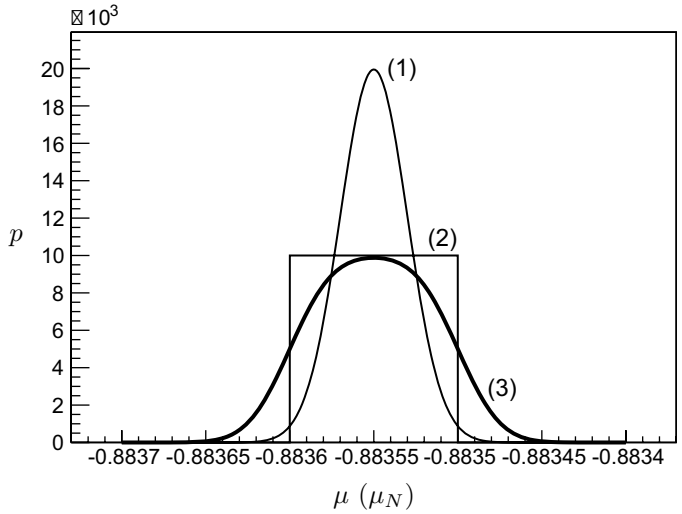

Figure A.1: Probability densities for the magnetic moment of ^{31}Mg. (1) The normal distribution of the statistical error; (2) The constant distribution of the systematic error; (3) The total probability density distribution;

deviation:

$$\zeta = \sqrt{\sigma^2 + \delta^2}\,. \tag{A.3}$$

Lets consider now the case of having a constant distribution of the systematic error:

$$p_\delta(x;\, x_0,\, \delta) = \begin{cases} 1/2\,\delta\,, & x \in [x_0 - \delta,\, x_0 + \delta] \\ 0\,, & x \in (-\infty,\, x_0 - \delta) \cup (x_0 + \delta,\, \infty)\,, \end{cases} \tag{A.4}$$

while the statistical error is normally distributed. Substituting (3.47) and (A.4) into (A.2) yields the total probability density distribution:

$$p(x;\, x_0,\, \sigma,\, \delta) = \frac{1}{4\,\delta}\,\left[\mathrm{erf}\left(\frac{x_0 + \delta - x}{\sigma\sqrt{2}}\right) + \mathrm{erf}\left(\frac{x_0 - \delta - x}{\sigma\sqrt{2}}\right)\right]\,, \tag{A.5}$$

where $\mathrm{erf}(x)$ is the so-called error function[A]. Often the statistical and systematic errors are combined in one number, usually through the relation (A.3) or simply by summing the two errors. In any case, one is obliged to associate the quoted error with a certain confidence level. This can be done by integrating $p(x;\, x_0,\, \sigma,\, \delta)$, given in the most general case with (A.2), in the interval

[A] The error function is defined as: $\mathrm{erf}(x) = \frac{2}{\sqrt{\pi}} \int_0^x e^{-t^2} dt$.

Table A.1: Confidence levels for the magnetic moment of ^{31}Mg: $\mu = -0.88355(\zeta)\,\mu_N$

ζ	confidence level (%)
1×10^{-5}	19.7
2×10^{-5}	38.8
3×10^{-5}	56.7
4×10^{-5}	72.1
5×10^{-5}	84

$(x_0 - \zeta,\, x_0 + \zeta)$, where ζ is the quoted error. Lets consider now the magnetic moments of ^{31,33}Mg, with their uncertainties, from Tab. 5.2 and Tab. 5.4. The exact probability distributions (3.47), (A.4) and (A.5) of ^{31}Mg are drawn in Fig. A.1. This case is chosen for an illustration, because the systematic error dominates and there is a significant difference, between the plotted functions. Calculated confidence levels, associated with the experimental magnetic moments of ^{31,33}Mg, are given in Tab. A.1 and Tab. A.2.

Table A.2: Confidence levels for the magnetic moment of ^{33}Mg: $\mu = -0.7456(\zeta)\,\mu_N$

ζ	confidence level (%)
1×10^{-4}	18.5
2×10^{-4}	36
3×10^{-4}	51.7
4×10^{-4}	65
5×10^{-4}	75.8

A.2 Individual NMR measurements on ^{33}Mg

All independent NMR spectra of ^{33}Mg are presented in Figs. A.2, A.3 and A.4. The measurements with small frequency modulation (Figs. A.2 and A.3) are fitted with the Lorentzian profile (3.48). The spectra in Fig. A.4 are obtained with modulation significantly larger than the natural linewidth. The purpose ot these was to locate the resonance and establish a narrower range for the consequent measurements. They are treated with the theoretical function (2.69) developed in Section 2.6. The fitting results are presented in Tab. A.3, together

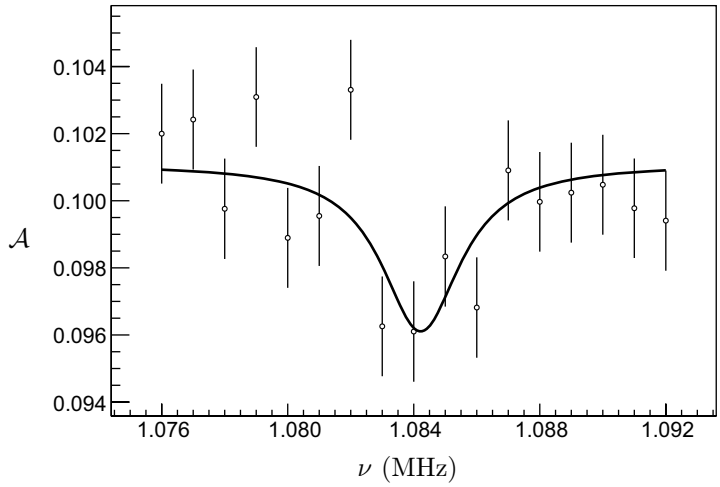

Figure A.2: NMR of ^{33}Mg in Pt.

with the amplitude M of the frequency modulation. The consistency between the independent measurements can be verified by comparing the ratio of the Larmor frequencies of ^{31,33}Mg, which is independent of the magnetic field and the chemical and Knight shifts. The only value that is more than two standard deviations away from the most precise measurement is derived from the spectrum displayed in Fig. A.4 (a). Due to the lack of points on the right wing of the resonance there could be a systematic deviation in the fit to higher frequencies. The measurements with large modulation are given below the line in

Table A.3: Individual NMR frequencies of ^{33}Mg and calibration frequencies of ^{31}Mg. The ratio $\nu(^{33}\mathrm{Mg})/\nu(^{31}\mathrm{Mg}) = g(^{33}\mathrm{Mg})/g(^{31}\mathrm{Mg})$ is independent of the magnetic field. The measurements used to obtain the final result are denoted with $\langle\star\rangle$ (see the text).

	$\nu(^{33}\mathrm{Mg})$ (kHz)	$\nu(^{31}\mathrm{Mg})$ (kHz)	$g(^{33}\mathrm{Mg})/g(^{31}\mathrm{Mg})$	M (kHz)
*Fig. A.2	1084.22(76)	3850.40(16)	0.28159(20)	1
*Fig. A.3 (a)	1083.0(12)	3849.05(20)	0.28137(31)	4
*Fig. A.3 (b)	1082.34(45)	the same	0.28120(12)	1
Fig. A.4 (a)	1086.3(12)	3851.51(6)	0.28205(31)	20
Fig. A.4 (b)	1086(3)	the same	0.28197(78)	10

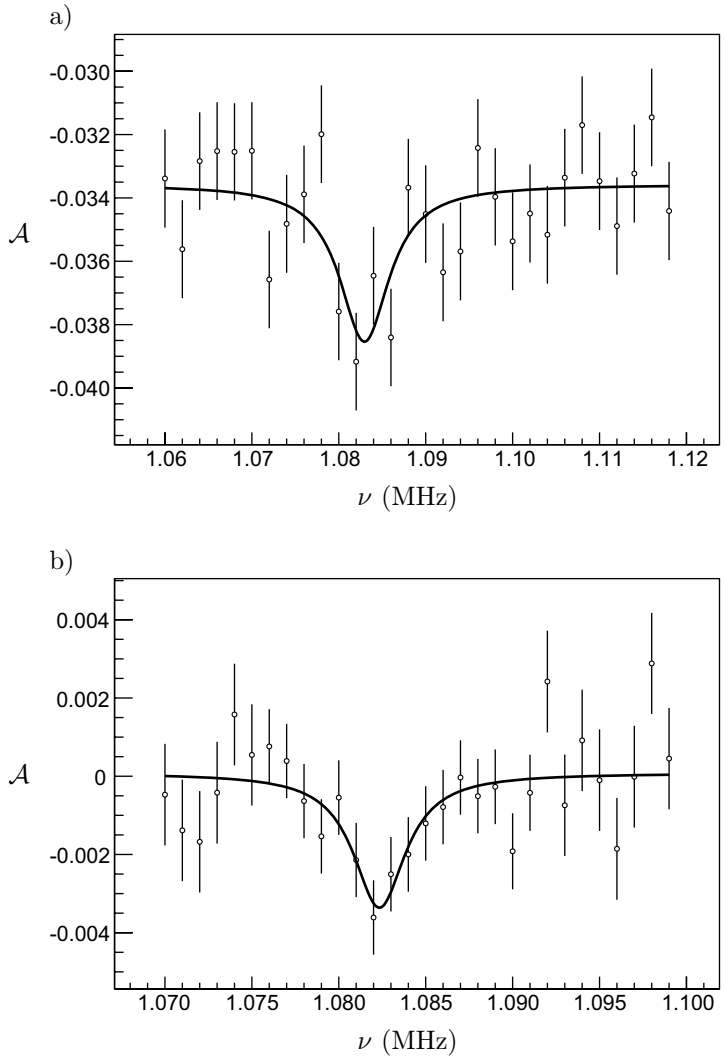

Figure A.3: NMR spectra of ^{33}Mg in MgO with small frequency modulation.

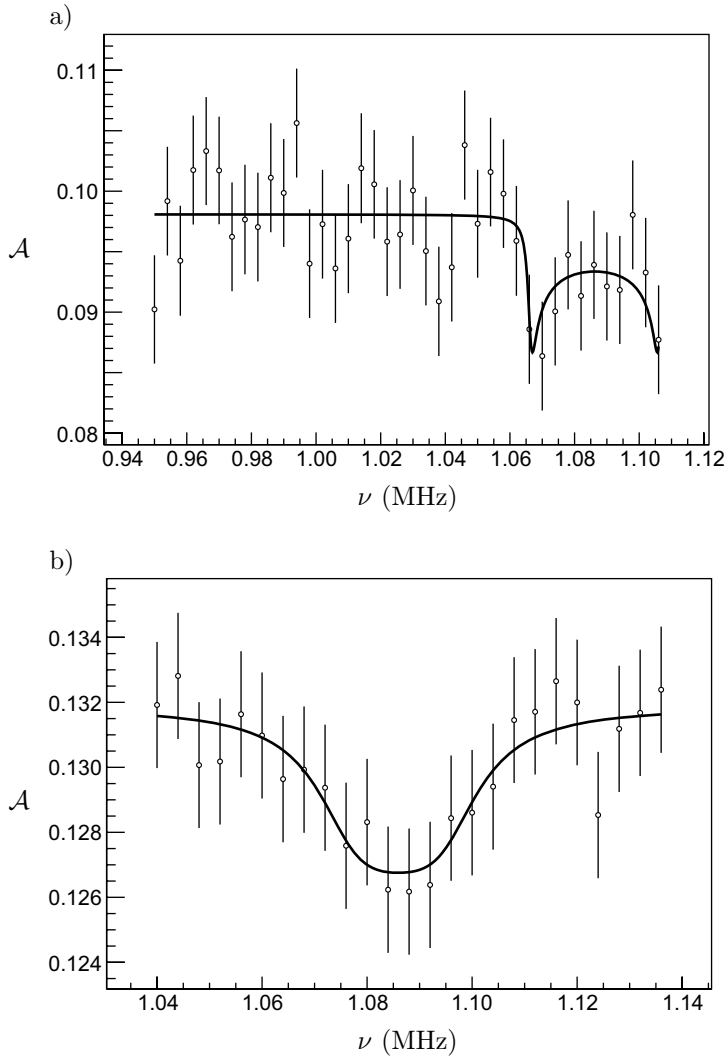

Figure A.4: NMR spectra of ^{33}Mg in MgO with large frequency modulation.

Tab. A.3. These are not used for obtaining the final result, since the accuracy of (2.69) has not been verified independently (for instance by measuring NMR with a large modulation in the reference nucleus and comparing the the result with those derived from narrow resonance lines). The weighted mean of the Larmor frequencies is MgO (Figs. A.3 (a) and (b)) and the frequency in Pt (Fig. A.2) together with the reference frequencies of ^{31}Mg in the same hosts are displayed in Tab. 5.3. The weighted mean of the two independent ratios $\nu(^{33}\mathrm{Mg})/\nu(^{31}\mathrm{Mg}) = g(^{33}\mathrm{Mg})/g(^{31}\mathrm{Mg})$ is used to calculate the final value of the ^{33}Mg g factor.

A.3 Individual HFS measurements on ^{27}Mg II

The procedure of fitting the fluorescence spectra of ^{27}Mg II is described in Section 4.2. The weighted mean of three independent measurements yields the final value of the ground-state magnetic hyperfine parameter, as presented in Tab. A.4. Fig. 4.2 corresponds to the first value in the table. The uncertainties are mainly statistical in origin. The A factor of the excited state is calculated from the one of the ground state with the use of the ratio $A(3^2P_{1/2})/A(3^2S_{1/2})$, given in Tab. 4.2. The final results are presented in Tab. 4.3.

Table A.4: Magnetic hyperfine parameter in the ground state of ^{27}Mg II from three independent measurements.

	$A(3^2S_{1/2})$ (MHz)
	−1433.1(85)
	−1425.3(80)
	−1436.9(73)
weighted mean	−1432.0(46)

A.4 Coupling of angular momenta

The coupling of two angular momenta $\boldsymbol{J}_1$ and $\boldsymbol{J}_2$ to the total angular momentum $\boldsymbol{J} = \boldsymbol{J}_1 + \boldsymbol{J}_2$ is considered first. The associated quantum numbers must satisfy the triangle condition:

$$\Delta(J_1 J_2 J) \equiv |J_2 - J_1| \leq J \leq J_1 + J_2 \ . \tag{A.6}$$

J takes either the integer or the half-integer values in that interval, depending on J_1 and J_2, so that $J_1 + J_2 + J$ is an integer. The Clebsch-Gordan coefficients:

$$\langle J_1 M_1 J_2 M_2 | J_1 J_2 J M \rangle \equiv \langle J_1 M_1 J_2 M_2 | J M \rangle \ , \tag{A.7}$$

where M_1, M_2 and M are the projection quantum numbers, are used to transfer wave functions from $|J_1 J_2 JM\rangle$ to $|J_1 J_2 M_1 M_2\rangle$ basis:

$$|J_1 J_2 JM\rangle = \sum_{M_1 M_2} |J_1 M_1 J_2 M_2\rangle \langle J_1 M_1 J_2 M_2 | J_1 J_2 JM\rangle \ . \tag{A.8}$$

These are real numbers with symmetry properties given by:

$$\langle J_1 M_1 J_2 M_2 | JM\rangle = (-1)^{J_1+J_2-J} \langle J_2 M_2 J_1 M_1 | JM\rangle \ , \tag{A.9}$$

$$\langle J_1 M_1 J_2 M_2 | JM\rangle = (-1)^{J_1+J_2-J} \langle J_1, -M_1 J_2, -M_2 | J, -M\rangle \tag{A.10}$$

and

$$\langle J_1 M_1 J_2 M_2 | JM\rangle = (-1)^{J_2+M_2} \sqrt{\frac{2J+1}{2J_1+1}} \langle J_2, -M_2 JM | J_1 M_1\rangle \ . \tag{A.11}$$

Their orthogonality conditions are:

$$\sum_{JM} \langle J_1 M_1 J_2 M_2 | JM\rangle \langle J_1 M_1' J_2 M_2' | JM\rangle = \delta_{M_1 M_1'} \delta_{M_2 M_2'} \ , \tag{A.12}$$

$$\sum_{M_1 M_2} \langle J_1 M_1 J_2 M_2 | JM\rangle \langle J_1 M_1 J_2 M_2 | J'M'\rangle = \delta_{JJ'} \delta_{MM'} \ . \tag{A.13}$$

The Clebsch-Gordan coefficients are related to the Wigner's $3j$ coefficients by:

$$\langle J_1 M_1 J_2 M_2 | JM\rangle = (-1)^{J_1-J_2+M} \sqrt{2J+1} \begin{pmatrix} J_1 & J_2 & J \\ M_1 & M_2 & -M \end{pmatrix}, \tag{A.14}$$

where $M_1 + M_2 = M$. The symmetry properties of the $3j$ coefficients are given with:

$$\begin{pmatrix} J_1 & J_2 & J_3 \\ M_1 & M_2 & M_3 \end{pmatrix} = (-1)^p \begin{pmatrix} J_a & J_b & J_c \\ M_a & M_b & M_c \end{pmatrix}, \tag{A.15}$$

where $p = J_a + J_b + J_c$ when two neighboring columns have been interchanged. This formula is still valid when the top row is unchanged but the bottom row inverts its sign ($M_a = -M_1$, $M_b = -M_2$, $M_c = -M_3$). Note that the $3j$ symbol is defined only if the triangle condition $\Delta(J_1 J_2 J_3)$ is satisfied and $M_1 + M_2 + M_3 = 0$, otherwise it equals zero. The orthogonality relations are:

$$\sum_{JM} (2J+1) \begin{pmatrix} J_1 & J_2 & J \\ M_1 & M_2 & M \end{pmatrix} \begin{pmatrix} J_1 & J_2 & J \\ M_1' & M_2' & M \end{pmatrix} = \delta_{M_1 M_1'} \delta_{M_2 M_2'} \ , \tag{A.16}$$

$$\sum_{M_1 M_2} (2J+1) \begin{pmatrix} J_1 & J_2 & J \\ M_1 & M_2 & M \end{pmatrix} \begin{pmatrix} J_1 & J_2 & J' \\ M_1 & M_2 & M' \end{pmatrix} = \delta_{JJ'} \delta_{MM'} \ . \tag{A.17}$$

The $3j$ symbols, and therefore the Clebsch-Gordan coefficients trough the relation (A.14), can be calculated with the formula:

$$\begin{pmatrix} a & b & c \\ \alpha & \beta & \gamma \end{pmatrix} = (-1)^{a-b-\gamma}\sqrt{\Delta(abc)} \quad \times \tag{A.18}$$
$$\sqrt{(a+\alpha)!\,(a-\alpha)!\,(b+\beta)!\,(b-\beta)!\,(c+\gamma)!\,(c-\gamma)!} \quad \times$$
$$\sum_t \frac{(-1)^t}{t!\,(c-b+t+\alpha)!\,(c-a+t-\beta)!\,(a+b-c-t)!\,(a-t-\alpha)!\,(b-t+\beta)!} \,,$$

where the sum is over all integers t for which the factorials have nonnegative arguments. The triangle coefficient $\Delta(abc)$ must be distinguished from the triangle condition (A.6). It can be calculated with:

$$\Delta(abc) = \frac{(a+b-c)!\,(a-b+c)!\,(-a+b+c)!}{(a+b+c+1)!} \,. \tag{A.19}$$

In cases of coupling three angular momenta the notation $|(J_1J_2J_{12})J_3JM\rangle$, adopted from Ref. [37], represents Clebsch-Gordan coupling of $\boldsymbol{J}_1$ and $\boldsymbol{J}_2$ to $\boldsymbol{J}_{12}$, which in turn undergoes Clebsch-Gordan coupling with $\boldsymbol{J}_3$ to form $\boldsymbol{J}$. Another way of coupling is to combine $\boldsymbol{J}_2$ and $\boldsymbol{J}_3$:

$$|J_1(J_2J_3J_{23})JM\rangle = \sum_{J_{12}} |(J_1J_2J_{12})J_3JM\rangle\langle(J_1J_2J_{12})J_3JM|J_1(J_2J_3J_{23})JM\rangle \,. \tag{A.20}$$

The transformation coefficients in the above relation are independent of the projection quantum number M. They can be expressed using the Wigner's $6j$ coefficients:

$$\langle(J_1J_2J_{12})J_3JM|J_1(J_2J_3J_{23})JM\rangle = (-1)^{J_1+J_2+J_3+J}\sqrt{(2J_{12}+1)(2J_{23}+1)}\begin{Bmatrix} J_1 & J_2 & J_{12} \\ J_3 & J & J_{23} \end{Bmatrix} \,. \tag{A.21}$$

An orthogonality condition of the $6j$ coefficients is:

$$\sum_{j_3}(2j_3+1)(2J_3+1)\begin{Bmatrix} j_1 & j_2 & j_3 \\ J_1 & J_2 & J_3 \end{Bmatrix}\begin{Bmatrix} j_1 & j_2 & j_3 \\ J_1 & J_2 & J_3' \end{Bmatrix} = \delta_{J_3J_3'} \,. \tag{A.22}$$

Their symmetry properties are:

$$\begin{Bmatrix} j_1 & j_2 & j_3 \\ J_1 & J_2 & J_3 \end{Bmatrix} = \begin{Bmatrix} j_a & j_b & j_c \\ J_a & J_b & J_c \end{Bmatrix} \tag{A.23}$$

and

$$\left\{ \begin{array}{ccc} j_1 & j_2 & j_3 \\ J_1 & J_2 & J_3 \end{array} \right\} = \left\{ \begin{array}{ccc} J_1 & J_2 & j_3 \\ j_1 & j_2 & J_3 \end{array} \right\} . \tag{A.24}$$

The $6j$ symbol, consider the one in the left column, is defined if each of the triads $(j_1 j_2 j_3)$, $(j_1 J_2 J_3)$, $(J_1 j_2 J_3)$ and $(J_1 J_2 j_3)$ satisfies the triangle condition (A.6) and the sum of their elements is an integer number. Otherwise it equals zero. The $6j$ coefficients can be computed with the formula:

$$\begin{aligned} \left\{ \begin{array}{ccc} a & b & c \\ \alpha & \beta & \gamma \end{array} \right\} = & \sqrt{\Delta(abc)\,\Delta(a\beta\gamma)\,\Delta(\alpha b\gamma)\,\Delta(\alpha\beta c)} \quad \times \\ & \sum_t (-1)^t (t+1)! \Big[(t-a-b-c)!\,(t-a-\beta-\gamma)! \quad \times \\ & (t-\alpha-b-\gamma)!\,(t-\alpha-\beta-c)!\,(a+b+\alpha+\beta-t)! \quad \times \\ & (b+c+\beta+\gamma-t)!\,(c+a+\gamma+\alpha-t)! \Big]^{-1} . \end{aligned} \tag{A.25}$$

The above relations as well as a detailed description concerning coupling of angular momenta can be found in Refs. [37, 38, 43, 87, 88].

The aim of this section is to provide the basics for working with Clebsch-Gordan, $3j$ and $6j$ coefficients and, more importantly, to offer a simplified code for calculating them. Their values are returned by the functions:

$$\mathrm{CG}\,(J_1,\, M_1,\, J_2,\, M_2,\, J,\, M) \tag{A.26}$$

$$\mathrm{TJ}\,(J_1,\, M_1,\, J_2,\, M_2,\, J_3,\, M_3) \tag{A.27}$$

$$\mathrm{SJ}\,(j_1,\, j_2,\, j_3,\, J_1,\, J_2,\, J_3)\,, \tag{A.28}$$

given in the file *functions.h* included at the end. Conditioning of the input parameters has been avoided in order to achieve maximum calculation speed. When using the code below, one should make sure that the input parameters are correct. CG() and TJ() have a fault if $M_1+M_2-M \neq 0$ and $M_1+M_2+M_3 \neq 0$, respectively. All functions properly give zero when the triangle conditions are not fulfilled, but have a fault when the input parameters are not integer or half integer and give a number or could crush due to the term $(-1)^t$.

```
//*************
//* functions.h *
//*************

//**********<<< maximum >>>**********
double Max(double x, double y){
        if(x>y)
                return x;
        else
```

```
        return y;}

//**********<<< minimum >>>**********
double Min(double x, double y){
    if(x<y)
        return x;
    else
        return y;}

//**********<<< factorial >>>**********
double frl(double n){
    double p=fabs(n);
    if(p==0)
        return 1;
    else{
        double q=1;
        for(double i=1;i<=p;i++)
            q=q*i;
        return q;}}

//**********<<< triangle coefficient >>>**********
double delta(double j1, double j2, double j3){
    return frl(j1+j2-j3)*frl(j1-j2+j3)*frl(-j1+j2+j3)/frl(j1+j2+j3+1);}

//**********<<< 3j >>>**********
//**********      (   j1   j2   j3   )      **********
//**********      (   m1   m2   m3   )      **********
double TJ(double j1, double m1, double j2, double m2, double j3, double m3){
    double sum=0;
    for(double i=Max(Max(0,j2-j3-m1),m2+j1-j3);
        i<=Min(Min(j1+j2-j3,j1-m1),j2+m2);i++)
        sum=sum+pow(-1,i)
            /frl(i)/frl(j3-j2+i+m1)/frl(j3-j1+i-m2)
            /frl(j1+j2-j3-i)/frl(j1-i-m1)/frl(j2-i+m2);
    return pow(-1,j1-j2-m3)*sqrt(delta(j1,j2,j3)*frl(j1+m1)*frl(j1-m1)
        *frl(j2+m2)*frl(j2-m2)*frl(j3+m3)*frl(j3-m3))*sum;}

//**********<<< 6j >>>**********
//**********      {   j1   j2   j3   }      **********
//**********      {   J1   J2   J3   }      **********
double SJ(double j1, double j2, double j3, double J1, double J2, double J3){
    double sum=0;
    for(double i=Max(Max(j1+j2+j3,j1+J2+J3),Max(J1+j2+J3,J1+J2+j3));
        i<=Min(Min(j1+j2+J1+J2,j2+j3+J2+J3),j3+j1+J3+J1);i++)
        sum=sum+pow(-1,i)*frl(i+1)
            /frl(i-j1-j2-j3)/frl(i-j1-J2-J3)/frl(i-J1-j2-J3)/frl(i-J1-J2-j3)
            /frl(j1+j2+J1+J2-i)/frl(j2+j3+J2+J3-i)/frl(j3+j1+J3+J1-i);
    return sqrt(delta(j1,j2,j3)*delta(j1,J2,J3)*delta(J1,j2,J3)*delta(J1,J2,j3))*sum;}

//**********<<< Clebsch-Gordan >>>**********
//**********      < j1  m1 j2  m2 |  j3  m3 >      **********
double CG(double j1, double m1, double j2, double m2, double j3, double m3){
    return pow(-1,j1-j2+m3)*sqrt(2*j3+1)*TJ(j1,m1,j2,m2,j3,-m3);}
```

Appendix B

Numerical functions

B.1 Realistic decay rate function

The code presented in this section uses a fifth order Runge-Kutta method with variable step size [49, 50]. The function:

$$rate\,(\nu-\nu_0,\,\nu_0,\,A_{\rm gr},\,A_{\rm ex},\,B_{\rm gr},\,B_{\rm ex},\\ J_{\rm gr},\,J_{\rm ex},\,L_{\rm gr},\,L_{\rm ex},\,S_{\rm gr},\,S_{\rm ex},\,I,\,\tau,\,B,\,I_l,\,\Delta M) \quad \text{(B.1)}$$

returns the decay rate per atom $\mathcal{R}/N$. The parameters are as follows: ν - the transition frequency (MHz), ν_0 - the fine structure splitting (MHz), follow the hyperfine parameters of the two states in MHz and their quantum numbers, I - the nuclear spin, τ - the lifetime of the decaying state (s), B - the external magnetic field (T), I_l - the laser intensity (W/m^2) and ΔM - the polarization of the laser (-1, 0, 1, 2 - no polarization).

```
//************************
//* Optical spectra simulator *
//************************

#include "functions.h"

//**********<<< constants >>>**********
const double C=299792457.4;                    //Speed of light (m/s)
const double gL=1;                             //atomic g factor (muB)
const double gS=2.00232;                       //atomic g factor (muB)
const double muB=9.27408e-24;                  //Bohr magneton (J/T)
const double h=6.62618e-34;                    //Planck's constant (J.s)
const double pi=3.14159265;

//**********<<< calculates the energy of a level relative >>>**********
//**********<<< to the FSLevel of the ground state >>>**********
```

```
double Ener(double fst,double L,double S,double J,double I,double F,double M,
            double A,double B,double field)//MHz(A and B in MHz, field in T)
{
        double cA=F*(F+1)-I*(I+1)-J*(J+1);                                      20
        double cB;
        if(I!=0.5 && J!=0.5)
                cB=(1.5*cA*(cA+1)-2*I*(I+1)*J*(J+1))/(4*I*(2*I-1)*J*(2*J-1));
        else
                cB=0;
        double gJ,gF;//for the Lande formulas
        gJ=gL*(J*(J+1)+L*(L+1)-S*(S+1))/(2*J*(J+1))
                +gS*(J*(J+1)-L*(L+1)+S*(S+1))/(2*J*(J+1));
        if(F!=0)
                gF=gJ*(F*(F+1)+J*(J+1)-I*(I+1))/(2*F*(F+1));                    30
                //the nuclear term is neglected
        else
                gF=0;
        return fst+A*cA/2+B*cB+gF*muB*field*M*1.e-6/h;
}

//**********<<< D = B x Rho >>>**********
const double factor=C*C/(32*h*pow(pi,3));
double BxRho(double f0,double f,double Aeg,double G,double Il)
//s-1(MHz,MHz,s-1,s-1,W/m2)                                                     40
{
        return factor*Aeg*Il*G/(pow(1.e6*(f-f0),2)+pow(G/(4*pi),2))
                /(pow(f0*1.e6,2)*f*1.e6);
}

//**********<<< main function >>>**********
double rate(double f,double fst,double Agr,double Aex,double Bgr,double Bex,
            double Jgr,double Jex,double Lgr,double Lex,double Sgr, double Sex,
            double I,double lifetime,double field,double Il,double deltaM)
            //decays per second per atom(6 x MHz,7 x number,s,T,W/m2,number)    50
{
        //**********<<< input parameters >>>**********
        const double G=1/lifetime; //FWHM in terms of angular frequency
        const double fst_gr=0;
        int Ngr=int((2*Jgr+1)*(2*I+1));
        int Nex=int((2*Jex+1)*(2*I+1));
        int N=Ngr+Nex;
        double E[100];      //state energy in MHz
        double sL[100];     //L
        double sS[100];     //S                                                 60
        double sJ[100];     //J
        double sF[100];     //F
        double sM[100];     //M
        double A[100][100]; //spontaneous emission coefficient
        double AT[100];     //Total decay probability
        double D[100][100]; //D = B x Rho, absorption/stim. emission coefficient
        double M[100][100]; //Matrix for the rate equations
        double P[100];      //population of the levels
```

```
//**********<<< initialization to 0 >>>**********
int i,j;
for(i=0;i<N;i++)
{
        P[i]=0;
        AT[i]=0;
        for(j=0;j<N;j++)
        {
                A[i][j]=0;
                D[i][j]=0;
                M[i][j]=0;
        }
}

//**********<<< initialization of E,A,D,sL,sS,sJ,sF,sM >>>**********
double Fg,Fe;
double Mg,Me;
j=0;
for(Fg=fabs(Jgr-I);Fg<=Jgr+I;Fg++)
{
        for(Mg=-Fg;Mg<=Fg;Mg++)
        {
                sL[Nex+j]=Lgr;sS[Nex+j]=Sgr;sJ[Nex+j]=Jgr;
                sF[Nex+j]=Fg;sM[Nex+j]=Mg;
                E[Nex+j]=Ener(fst_gr,Lgr,Sgr,Jgr,I,Fg,Mg,Agr,Bgr,field);
                j++;
        }
}
i=0,j=0;
if(deltaM==2)
{
        for(Fe=fabs(Jex-I);Fe<=Jex+I;Fe++)
        {
                for(Me=-Fe;Me<=Fe;Me++)
                {
                        sL[i]=Lex;sS[i]=Sex;sJ[i]=Jex;sF[i]=Fe;sM[i]=Me;
                        E[i]=Ener(fst,Lex,Sex,Jex,I,Fe,Me,Aex,Bex,field);
                        j=0;
                        for(Fg=fabs(Jgr-I);Fg<=Jgr+I;Fg++)
                        {
                                for(Mg=-Fg;Mg<=Fg;Mg++)
                                {
                                        A[i][Nex+j]=(2*Jex+1)*(2*Fe+1)*(2*Fg+1)
                                                *pow(TJ(Fg,-Mg,1,Mg-Me,Fe,Me),2)
                                                *pow(SJ(Jgr,Fg,I,Fe,Jex,1),2)/lifetime;
                                        if(abs(Mg-Me)<=1)//condition 3j
                                        {
                                                D[i][Nex+j]=BxRho(fabs(E[i]-E[Nex+j]),
                                                        f+fst,A[i][Nex+j],G,Il);
                                                D[Nex+j][i]=D[i][Nex+j];
                                        }
                                        j++;
                                }
```

```
                        }
                        i++;
                }
        }
}
else
{
        for(Fe=fabs(Jex−I);Fe<=Jex+I;Fe++)                                    130
        {
                for(Me=−Fe;Me<=Fe;Me++)
                {
                        sL[i]=Lex;sS[i]=Sex;sJ[i]=Jex;sF[i]=Fe;sM[i]=Me;
                        E[i]=Ener(fst,Lex,Sex,Jex,I,Fe,Me,Aex,Bex,field);
                        j=0;
                        for(Fg=fabs(Jgr−I);Fg<=Jgr+I;Fg++)
                        {
                                for(Mg=−Fg;Mg<=Fg;Mg++)
                                {                                             140
                                        A[i][Nex+j]=(2*Jex+1)*(2*Fe+1)*(2*Fg+1)
                                                *pow(TJ(Fg,−Mg,1,Mg−Me,Fe,Me),2)
                                                *pow(SJ(Jgr,Fg,I,Fe,Jex,1),2)/lifetime;
                                        if(Mg−Me==deltaM)//polarization
                                        {
                                                D[i][Nex+j]=BxRho(fabs(E[i]−E[Nex+j]),
                                                        f+fst,A[i][Nex+j],G,Il);
                                        }
                                        if(Me−Mg==deltaM)//polarization
                                        {                                     150
                                                D[Nex+j][i]=BxRho(fabs(E[i]−E[Nex+j]),
                                                        f+fst,A[i][Nex+j],G,Il);
                                        }
                                        j++;
                                }
                        }
                        i++;
                }
        }
}                                                                             160

//***<<< initialization of M; dNdt = M . N (dNidt=\sum_j(Mij.Nj)) >>>***
double sum;
for(i=0;i<Nex;i++)
{
        sum=0;
        for(j=0;j<N;j++)
        {
                M[i][j]=D[j][i];
                sum=sum+(A[i][j]+D[i][j]);                                    170
        }
        M[i][i]=M[i][i]−sum;
}
for(i=Nex;i<N;i++)
{
```

```
        sum=0;
        for(j=0;j<N;j++)
        {
                M[i][j]=A[j][i]+D[j][i];
                sum=sum+D[i][j];                                        180
        }
        M[i][i]=M[i][i]−sum;
}

//******<<< calculationg the population of the levels at time t=0 >>>******
for(i=Nex;i<N;i++)
        P[i]=1/double(Ngr);

//*******<<< fifth order Runge - Kutta with adaptive step size >>>*******
double tof=1.e−7;                       //time of flight                190
double t=0;                             //time
double dt=1.e−10;                       //size of the first step
double d0=1.e−8;                        //precision
double d=0;                             //error
double delta;                           //temp. variable
double k1[100],k2[100],k3[100],k4[100],k5[100],k6[100];
//********** Cash - Karp parameters **********
double a1=0.,a2=0.2,a3=0.3,a4=0.6,a5=1.0,a6=0.875,
        b21=0.2,b31=3./40.,b32=9./40.,b41=0.3,b42=−0.9,b43=1.2,
        b51=−11./54.,b52=2.5,b53=−70./27.,b54=35./27.,                  200
        b61=1631./55296.,b62=175./512.,b63=575./13824.,
        b64=44275./110592.,b65=253./4096.,c1=37./378.,
        c2=0.,c3=250./621.,c4=125./594.,c5=0.,c6=512./1771.,
        dc1=c1−2825./27648.,dc2=0.,dc3=c3−18575./48384.,
        dc4=c4−13525./55296.,dc5=−277./14336.,dc6=c6−0.25;
while(t<=tof)
{
        for(i=0;i<N;i++)
        {
                k1[i]=0;                                                210
                for(j=0;j<N;j++)
                        k1[i]=k1[i]+M[i][j]*P[j];
                k1[i]=dt*k1[i];
        }
        for(i=0;i<N;i++)
        {
                k2[i]=0;
                for(j=0;j<N;j++)
                        k2[i]=k2[i]+M[i][j]*(P[j]+b21*k1[j]);
                k2[i]=dt*k2[i];                                         220
        }
        for(i=0;i<N;i++)
        {
                k3[i]=0;
                for(j=0;j<N;j++)
                        k3[i]=k3[i]+M[i][j]*(P[j]+b31*k1[j]+b32*k2[j]);
                k3[i]=dt*k3[i];
        }
```

```
            for(i=0;i<N;i++)
            {
                k4[i]=0;
                for(j=0;j<N;j++)
                    k4[i]=k4[i]+M[i][j]*(P[j]+b41*k1[j]+b42*k2[j]+b43*k3[j]);
                k4[i]=dt*k4[i];
            }
            for(i=0;i<N;i++)
            {
                k5[i]=0;
                for(j=0;j<N;j++)
                    k5[i]=k5[i]+M[i][j]
                    *(P[j]+b51*k1[j]+b52*k2[j]+b53*k3[j]+b54*k4[j]);
                k5[i]=dt*k5[i];
            }
            for(i=0;i<N;i++)
            {
                k6[i]=0;
                for(j=0;j<N;j++)
                    k6[i]=k6[i]+M[i][j]
                    *(P[j]+b61*k1[j]+b62*k2[j]+b63*k3[j]+b64*k4[j]+b65*k5[j]);
                k6[i]=dt*k6[i];
            }
            d=0;
            for(i=0;i<N;i++)
            {
                P[i]=P[i]+c1*k1[i]+c2*k2[i]+c3*k3[i]+c4*k4[i]+c5*k5[i]+c6*k6[i];
                delta=fabs(dc1*k1[i]+dc2*k2[i]+dc3*k3[i]
                +dc4*k4[i]+dc5*k5[i]+dc6*k6[i]);
                if(d<delta)
                    d=delta;
            }
            if(t==tof)
                break;
            dt=dt*pow(d0/d,0.2);
            if(t+dt>tof)
                dt=tof-t;
            t=t+dt;
        }

        //**********<<< calculation of the decay rate >>>**********
        double rate=0;
        for(i=0;i<Nex;i++)
        {
            for(j=Nex;j<N;j++)
                AT[i]=AT[i]+A[i][j];
            rate=rate+P[i]*AT[i];
        }
        return rate;
}
```

B.2 Pseudo Voigt function

The following code offers the function:

$$\mathrm{ETCH}\,(x,\,\sigma,\,\Gamma_L)\,, \tag{B.2}$$

returning, relatively quickly and very accurately, the values of of the Voigt function (3.46).

```
//**********<<< Normalized Gaussian >>>**********
const double pi=3.14159265;
double G(double x,double s){//s=sigma
        double S=fabs(s);
        return exp(-0.5*pow(x/S,2))/(S*sqrt(2*pi));}

//**********<<< Normalized Lorentzian >>>**********
double L(double x,double GL){//GL=FWHM
        double gl=fabs(GL);
        return 0.5*gl/(pow(gl/2,2)+pow(x,2))/pi;}

//**********<<< Normalized Irrational function >>>**********
double FI(double x,double gI){
        double gi=fabs(gI);
        return pow(1+pow(x/gi,2),-1.5)/(2*gi);}

//**********<<< Normalized Squared Hyperbolic function >>>**********
double FP(double x,double gP){
        double gp=fabs(gP);
        return pow(1/cosh(x/gp),2)/(2*gp);}

//**********//////////////\\\\\\\\\\\\\\**********
//**********((( Extended Pseudo-Voigt )))**********
//**********\\\\\\\\\\\\\\//////////////**********

//**********<<< Extended Pseudo-Voigt function >>>**********
double aX[7]={0.66, 0.15021,-1.24984,4.74052,-9.48291,8.48252,-2.95553};
double bX[7]={-0.42179,-1.25693,10.30003,-23.45651,29.14158,-16.50453,3.19974};
double cX[7]={1.19913,1.43021,-15.36331,47.06071,-73.61822,57.92559,-17.80614};
double dX[7]={1.10186,-0.47745,-0.68688,2.76622,-4.55466,4.05475,-1.26571};
double fX[7]={-0.30165,-1.38927,9.3155,-24.10743,34.96491,-21.18862,3.7029};
double gX[7]={0.25437,-0.14107,3.23653,-11.09215,22.10544,-24.12407,9.76947};
double hX[7]={1.01579,1.50429,-9.21815,23.59717,-39.71134,32.83023,-10.02142};
double ETCH(double x,double s,double GL)
{
        double S=fabs(s),gl=fabs(GL);
        double GG=2*S*sqrt(2*log(2));
        double r=gl/(GG+gl);
        double wG=0,wL=0,wI=0,wP=0;
        double nL=0,nI=0,nP=0;
        for(int i=0;i<=6;i++)
        {
                wG=wG+aX[i]*pow(r,i);
```

```
        wL=wL+bX[i]*pow(r,i);
        wI=wI+cX[i]*pow(r,i);
        wP=wP+dX[i]*pow(r,i);
        nL=nL+fX[i]*pow(r,i);
        nI=nI+gX[i]*pow(r,i);
        nP=nP+hX[i]*pow(r,i);
}                                                                    50
wG=(GG+gl)*(1−r*wG);
wL=(GG+gl)*(1−(1−r)*wL);
wI=(GG+gl)*wI;
wP=(GG+gl)*wP;
nL=r*(1+(1−r)*nL);
nI=r*(1−r)*nI;
nP=r*(1−r)*nP;
wG=wG/(2*sqrt(2*log(2)));
wI=wI*0.5/sqrt(pow(2,2/double(3))−1);
wP=wP*0.5/log(sqrt(2)+1);                                            60
return (1−nL−nI−nP)*G(x,wG)+nL*L(x,wL)+nI*FI(x,wI)+nP*FP(x,wP);}
```

B.3 Realistic polarization function

The code presented below is principally identical to the code for the transition rates, given in Appendix B.1, until the point at which the atomic level populations are calculated. There is a difference in the numerical procedure for solving the system of differential equations (3.26). For the purpose of increasing the amount of nuclear polarization, the interaction time with the laser radiation must be considerably longer. This is achieved by inducing optical pumping in the long section (6) of the apparatus, Fig 3.1. This long interaction time demands numerous steps for the solution of (3.26). While the fifth order Runge-Kutta method with variable step size is the more elegant approach, it is generally slower, especially for high I and J, than the fourth order Runge-Kutta method with constant step size, both described in Refs. [49, 50]. The second procedure was applied. The function:

$$polar\,(\nu-\nu_0,\,\nu_0,\,A_{\rm gr},\,A_{\rm ex},\,B_{\rm ex},\,J_{\rm ex},\,L_{\rm gr},\,L_{\rm ex},\,S_{\rm gr},\,S_{\rm ex},\,I,\,\tau,\,B,\,I_l,\,\Delta M) \quad \text{(B.3)}$$

returns the nuclear polarization (2.60). The parameters are as follows: ν - the transition frequency (MHz), ν_0 - the fine structure splitting (MHz), follow the hyperfine parameters of the two states in MHz and their quantum numbers, I - the nuclear spin, τ - the lifetime of the decaying state (s), B - the external magnetic field (T), I_l - the laser intensity (W/m^2) and ΔM - the polarization of the laser (-1, 0, 1). The code deals with excitations from $3^2S_{1/2}$.

```
//*******************************************************
//* This program is designed for optical pumping from 3^2S_1/2 *
//*******************************************************

#include "functions.h"

//**********<<< constants >>>**********
const double C=299792457.4;                    //Speed of light (m/s)
const double gL=1;                             //atomic g factor (muB)
const double gS=2.00232;                       //atomic g factor (muB)
const double muB=9.27408e-24;                  //Bohr magneton (J/T)
const double h=6.62618e-34;                    //Planck's constant (J.s)
const double pi=3.14159265;

//**********<<< calculates the energy of a level relative >>>**********
//**********<<< to the FSLevel of the ground state >>>**********
double Ener(double fst,double L,double S,double J,double I,double F,double M,
            double A,double B,double field)//MHz(A and B in MHz, field in T)
{
    double cA=F*(F+1)-I*(I+1)-J*(J+1);
    double cB;
    if(I!=0.5 && J!=0.5)
        cB=(1.5*cA*(cA+1)-2*I*(I+1)*J*(J+1))/(4*I*(2*I-1)*J*(2*J-1));
    else
        cB=0;
    double gJ,gF;//for the Lande formulas
    gJ=gL*(J*(J+1)+L*(L+1)-S*(S+1))/(2*J*(J+1))
        +gS*(J*(J+1)-L*(L+1)+S*(S+1))/(2*J*(J+1));
    if(F!=0)
        gF=gJ*(F*(F+1)+J*(J+1)-I*(I+1))/(2*F*(F+1));
        //the nuclear term is neglected
    else
        gF=0;
    return fst+A*cA/2+B*cB+gF*muB*field*M*1.e-6/h;
}

//**********<<< D = B x Rho >>>**********
const double factor=C*C/(32*h*pow(pi,3));
double BxRho(double f0,double f,double Aeg,double G,double Il)
//s-1(MHz,MHz,s-1,s-1,W/m2)
{
    return factor*Aeg*Il*G/(pow(1.e6*(f-f0),2)+pow(G/(4*pi),2))
        /(pow(f0*1.e6,2)*f*1.e6);
}

//**********<<< main function >>>**********
double polar(double f,double fst,double Agr,double Aex,double Bex,
             double Jex,double Lgr,double Lex,double Sgr, double Sex,
             double I,double lifetime,double field,double Il,double deltaM)
             //polarisation(5xMHz,6xnumber,s,T,W/m2,number)
{
    //**********<<< input parameters >>>**********
```

```
const double G=1/lifetime; //FWHM in terms of angular frequency
const double fst_gr=0;
const double Jgr=0.5;
const double Bgr=0;
int Ngr=int((2*Jgr+1)*(2*I+1));
int Nex=int((2*Jex+1)*(2*I+1));
int N=Ngr+Nex;
double E[100];      //state energy in MHz                                    60
double sL[100];     //L
double sS[100];     //S
double sJ[100];     //J
double sF[100];     //F
double sM[100];     //M
double A[100][100]; //spontaneous emission coefficient
double D[100][100]; //D = B x Rho, absorption/stim. emission coefficient
double M[100][100]; //Matrix for the rate equations
double P[100];      //population of the levels
                                                                           70
//**********<<< initialization to 0 >>>**********
int i,j;
for(i=0;i<N;i++)
{
        P[i]=0;
        for(j=0;j<N;j++)
        {
                A[i][j]=0;
                D[i][j]=0;
                M[i][j]=0;                                                 80
        }
}

//**********<<< initialization of E,A,D,sL,sS,sJ,sF,sM >>>**********
double Fg,Fe;
double Mg,Me;
j=0;
for(Fg=fabs(Jgr-I);Fg<=Jgr+I;Fg++)
{
        for(Mg=-Fg;Mg<=Fg;Mg++)                                            90
        {
                sL[Nex+j]=Lgr;sS[Nex+j]=Sgr;sJ[Nex+j]=Jgr;
                sF[Nex+j]=Fg;sM[Nex+j]=Mg;
                E[Nex+j]=Ener(fst_gr,Lgr,Sgr,Jgr,I,Fg,Mg,Agr,Bgr,field);
                j++;
        }
}
i=0,j=0;
for(Fe=fabs(Jex-I);Fe<=Jex+I;Fe++)
{                                                                          100
        for(Me=-Fe;Me<=Fe;Me++)
        {
                sL[i]=Lex;sS[i]=Sex;sJ[i]=Jex;sF[i]=Fe;sM[i]=Me;
                E[i]=Ener(fst,Lex,Sex,Jex,I,Fe,Me,Aex,Bex,field);
                j=0;
```

```
                for(Fg=fabs(Jgr−I);Fg<=Jgr+I;Fg++)
                {
                        for(Mg=−Fg;Mg<=Fg;Mg++)
                        {
                                A[i][Nex+j]=(2*Jex+1)*(2*Fe+1)*(2*Fg+1)
                                        *pow(TJ(Fg,−Mg,1,Mg−Me,Fe,Me),2)
                                        *pow(SJ(Jgr,Fg,I,Fe,Jex,1),2)/lifetime;
                                if(Mg−Me==deltaM)//cirqular polarization
                                {
                                        D[i][Nex+j]=BxRho(fabs(E[i]−E[Nex+j]),
                                                f+fst,A[i][Nex+j],G,Il);
                                }
                                if(Me−Mg==deltaM)//cirqular polarization
                                {
                                        D[Nex+j][i]=BxRho(fabs(E[i]−E[Nex+j]),
                                                f+fst,A[i][Nex+j],G,Il);
                                }
                                j++;
                        }
                }
                i++;
        }
}

//**********<<< initialization of M; dNdt = M . N >>>**********
double sum;
for(i=0;i<Nex;i++)
{
        sum=0;
        for(j=0;j<N;j++)
        {
                M[i][j]=D[j][i];
                sum=sum+(A[i][j]+D[i][j]);
        }
        M[i][i]=M[i][i]−sum;
}
for(i=Nex;i<N;i++)
{
        sum=0;
        for(j=0;j<N;j++)
        {
                M[i][j]=A[j][i]+D[j][i];
                sum=sum+D[i][j];
        }
        M[i][i]=M[i][i]−sum;
}

//**********<<< equal population at t=0 >>>**********
for(i=Nex;i<N;i++)
        P[i]=1/double(Ngr);

//**********<<< fourth order Runge - Kutta >>>**********
int nSteps=400;                 //number of steps
```

```
double tof=3.e-6;           //time of flight
double dt=tof/nSteps;       //step size
double k1[100],k2[100],k3[100],k4[100];
int q;
for(q=0;q<nSteps;q++)
{
        for(i=0;i<N;i++)
        {
                k1[i]=0;
                for(j=0;j<N;j++)
                        k1[i]=k1[i]+M[i][j]*P[j];
                k1[i]=dt*k1[i];
        }
        for(i=0;i<N;i++)
        {
                k2[i]=0;
                for(j=0;j<N;j++)
                        k2[i]=k2[i]+M[i][j]*(P[j]+0.5*k1[j]);
                k2[i]=dt*k2[i];
        }
        for(i=0;i<N;i++)
        {
                k3[i]=0;
                for(j=0;j<N;j++)
                        k3[i]=k3[i]+M[i][j]*(P[j]+0.5*k2[j]);
                k3[i]=dt*k3[i];
        }
        for(i=0;i<N;i++)
        {
                k4[i]=0;
                for(j=0;j<N;j++)
                        k4[i]=k4[i]+M[i][j]*(P[j]+k3[j]);
                k4[i]=dt*k4[i];
        }
        for(i=0;i<N;i++)
                P[i]=P[i]+k1[i]/6+k2[i]/3+k3[i]/3+k4[i]/6;
}

//**********<<< I - J decoupling for J = 1/2 >>>**********
double MJ;
int NI=int(2*I+1);
double MI[100];     //m_I
if(Agr>=0)
{
        for(i=Nex;i<Nex+Ngr/2;i++)
                MI[i]=sM[i]+Jgr;
        for(i=Nex+Ngr/2;i<N;i++)
                MI[i]=sM[i]-Jgr;
}
else
{
        for(i=Nex;i<Nex+Ngr/2-1;i++)
                MI[i]=sM[i]-Jgr;
```

```
            for(i=Nex+Ngr/2-1;i<N-1;i++)
                MI[i]=sM[i]+Jgr;
            MI[N-1]=sM[N-1]-Jgr;
        }

        //**********<<< calculation the polarization >>>**********
        double polar=0;
        for(i=Nex;i<N;i++)
            polar=polar+MI[i]*P[i];                                    220
        polar=polar/I;
        return polar;
}
```

Bibliography

[1] S. G. Nilsson, Kgl. Dan. Viden. Selsk. Mat. Fys. Medd. **29**, No. 16 (1955).

[2] A. Bohr and B. R. Mottelson, *Nuclear Structure* (W. A. Benjamin, Inc., 1975).

[3] E. K. Warburton, J. A. Becker, and B. A. Brown, Phys. Rev. C **41**, 1147 (1990).

[4] C. Thibault *et al.*, Phys. Rev. C **12**, 644 (1975).

[5] X. Campi *et al.*, Nucl. Phys. **A251**, 193 (1975).

[6] G. Huber *et al.*, Phys. Rev. C **18**, 2342 (1978).

[7] B. H. Wildenthal and W. Chung, Phys. Rev. C **22**, 2260 (1980).

[8] A. Watt *et al.*, J. Phys. G **7**, L145 (1981).

[9] A. Poves and J. Retamosa, Phys. Lett. B **184**, 311 (1987).

[10] B. V. Pritychenko *et al.*, Phys. Lett. B **461**, 322 (1999).

[11] H. Iwasaki *et al.*, Phys. Lett. B **620**, 118 (2005).

[12] M. Keim *et al.*, Eur. Phys. J. A **8**, 31 (2000).

[13] Y. Utsuno, T. Otsuka, T. Mizusaki, and M. Honma, Phys. Rev. C **70**, 044307 (2004).

[14] V. Tripathi *et al.*, Phys. Rev. Lett. **94**, 162501 (2005).

[15] G. Neyens *et al.*, Phys. Rev. Lett. **94**, 022501 (2005).

[16] M. Kowalska, Ph.D. thesis, Institut für Physik, Universität Mainz (2006), ISBN 978 - 92 - 9083 - 282 - 9.

[17] P. Himpe *et al.*, Phys. Lett. B **643**, 257 (2006).

[18] P. Himpe *et al.* (2007), (in preparation).

[19] C. Détraz *et al.*, Phys. Rev. C **19**, 164 (1979).

[20] D. Guillemand-Mueller *et al.*, Nucl. Phys. **A426**, 37 (1984).

[21] T. Motobayashi *et al.*, Phys. Lett. B **346**, 9 (1995).

[22] K. Yoneda *et al.*, Phys. Lett. B **499**, 233 (2001).

[23] V. Chisté *et al.*, Phys. Lett. B **514**, 233 (2001).

[24] H. Iwasaki *et al.*, Phys. Lett. B **522**, 227 (2001).

[25] S. Nummela *et al.*, Phys. Rev. C **64**, 054313 (2001).

[26] B. V. Pritychenko *et al.*, Phys. Rev. C **65**, 061304(R) (2002).

[27] Z. Elekes *et al.*, Phys. Rev. C **73**, 044314 (2006).

[28] G. Neyens *et al.*, Eur. Phys. J. A (2007), (proceedings to RNB7 in print).

[29] Y. Yanagisawa *et al.*, Phys. Lett. B **566**, 84 (2003).

[30] D. T. Yordanov *et al.*, Balk. Phys. Lett. p. 358 (2004), ISSN 1301 - 8329.

[31] M. Kowalska *et al.*, Eur. Phys. J. A **25**, s01, 193 (2005).

[32] D. T. Yordanov *et al.* (2007), (in preparation).

[33] M. Kowalska *et al.* (2007), (in preparation).

[34] P. Ring and P. Schuck, *The Nuclear Many-Body Problem* (Springer-Verlag, 1980).

[35] P. J. Mohr and B. N. Taylor, Rev. Mod. Phys. **72**, 351 (2000).

[36] B. Castel and I. S. Towner, *Modern Theories of Nuclear Moments* (Clarendon Press, 1990).

[37] B. A. Brown, *Lecture Notes in Nuclear Structure Physics* (2005).

[38] K. L. G. Heyde, *The Nuclear Shell Model* (Springer-Verlag, 1994).

[39] J. M. Eisenberg and W. Greiner, *Nuclear Models: Collective and Single-Particle Phenomena* (North-Holland, 1987).

[40] D. L. Hill and J. A. Wheeler, Phys. Rev. **89**, 1102 (1953).

[41] B. Odom *et al.*, Phys. Rev. Lett. **97**, 030801 (2006).

[42] H. Kopfermann and E. E. Schneider, *Nuclear Moments* (Academic Press Inc., 1958).

[43] I. I. Sobel'man, *Introduction to the Theory of Atomic Spectra* (Pergamon Press, 1972).

[44] W. H. King, *Isotope Shifts in Atomic Spectra* (Plenum Press, 1984).

[45] G. Fricke *et al.*, At. Data Nucl. Data Tables **60**, 177 (1995).

[46] C. P. Slichter, *Principles of Magnetic Resonance* (Springer-Verlag, 1978).

[47] J. D. Jackson, S. B. Treiman, and H. W. Wyld, Phys. Rev. **106**, 517 (1957).

[48] N. Stone and H. Postma, eds., *Low Temperature Nuclear Orientation* (North-Holland, 1986).

[49] W. H. Press, S. A. Teukolsky, W. T. Vetterling, and B. P. Flannery, *Numerical Recipes in C++* (Cambridge University Press, 2002).

[50] `http://www.nr.com/`.

[51] `http://isolde.web.cern.ch/`.

[52] U. Köster *et al.*, Nucl. Instr. and Meth. in Phys. Res. B **204**, 347 (2003).

[53] R. B. Firestone, *Table of Isotopes* (John Wiley & Sons, Inc., 1996).

[54] F. Maréchal *et al.*, Phys. Rev. C **72**, 044314 (2005).

[55] A. C. Morton *et al.*, Phys. Lett. B **544**, 274 (2002).

[56] V. Kaufman and W. C. Martin, J. Phys. Chem. Ref. Data **20**, 83 (1991).

[57] W. Demtröder, *Laser Spectroscopy* (Springer-Verlag, 1996).

[58] W. Ansbacher, Y. Li, and E. H. Pinnington, Phys. Lett. A **139**, 165 (1989).

[59] C. J. Foot, *Atomic Physics* (Oxford University Press, 2005).

[60] P. Raghavan, At. Data Nucl. Data Tables **42**, 189 (1989).

[61] M. L. Citron *et al.*, Phys. Rev. A **16**, 1507 (1977).

[62] P. Thompson *et al.*, J. Appl. Cryst. **20**, 79 (1987).

[63] T. Ida *et al.*, J. Appl. Cryst. **33**, 1311 (2000).

[64] F. Alder and F. C. Yu, Phys. Rev. **82**, 105 (1951).

[65] P. M. Endt and C. V. der Leun, Nucl. Phys. **A310**, 1 (1978).

[66] W. M. Itano and D. J. Wineland, Phys. Rev. A **24**, 1364 (1981).

[67] W. Geithner *et al.*, Phys. Rev. C **71**, 064319 (2005).

[68] A. Klein *et al.*, Nucl. Phys. **A607**, 1 (1996).

[69] B. A. Brown *et al.*, MSU - NSCL report 1289.

[70] B. H. Wildenthal *et al.*, Prog. Part. Nucl. Phys. **11**, 5 (1984).

[71] A. Winnacker *et al.*, Phys. Lett. **67A**, 423 (1978).

[72] D. R. Goosman, C. N. Davids, and D. E. Alburger, Phys. Rev. C **8**, 1331 (1973).

[73] O. Niedermaier *et al.*, Phys. Rev. Lett. **94**, 172501 (2005).

[74] S. Nummela *et al.*, Phys. Rev. C **63**, 044316 (2001).

[75] J. C. Angélique *et al.*, AIP Conf. Proc. **831**, 134 (2006).

[76] W. Mittig *et al.*, Eur. Phys. J. A **15**, 157 (2002).

[77] F. D. Feiock and W. R. Johnson, Phys. Rev. **187**, 39 (1969).

[78] J. Korringa, Physica **16**, 601 (1950).

[79] K. Matsuta *et al.*, Hyp. Interact. **97/98**, 501 (1996).

[80] P. Baumann *et al.*, Phys. Rev. C **36**, 765 (1987).

[81] E. Roeckl *et al.*, Phys. Rev. C **10**, 1181 (1974).

[82] D. Sundholm and J. Olsen, Nucl. Phys. **A534**, 360 (1991).

[83] B. A. Brown and W. A. Richter, Phys. Rev. C **74**, 034315 (2006).

[84] P. Baumann *et al.*, Phys. Rev. C **39**, 626 (1989).

[85] L. K. Fifield *et al.*, Nucl. Phys. **A437**, 141 (1985).

[86] A. Jokinen, M. Lindroos, E. Molin, M. Petersson, and The ISOLDE Collaboration, Nucl. Instr. and Meth. in Phys. Res. B **204**, 86 (2003).

[87] A. Messiah, *Quantum mechanics* (North-Holland, 1962).

[88] `http://mathworld.wolfram.com/`.

Acknowledgments

At this place I would like to deeply thank the various people, who during the four (and a half) years of my research supported all my undertakings on the way of experimental nuclear physics. Without their help and assistance this doctoral dissertation would not have developed to the present stage.

Foremost, I would like to express my sincere gratitude to my promoter *Prof. Dr. Gerda Neyens*, who gave me the opportunity to work in her group and introduced me in the field of experimental physics with such an interesting research topic. I have been able to benefit from her scientific knowledge and experience throughout the years of my studies. Her balanced way of supervision enabled me, while having clear objectives, to work independently and take important decisions myself, which is something to appreciate in personal aspect. I have got used to the friendly atmosphere established in the group and her enthusiasm and I am looking forward for future collaborations.

I would like to express my sincerest gratitude to *Prof. Dr. Dimiter L. Balabanski*, who directed my energy and enthusiasm, when I was a postgraduate student at Sofia University without a clear view of the perspectives, on the path of experimental nuclear physics. I appreciate the fascinating discussions with him, which in some cases extended even outside the field of science. His experience and confidence during sleepless nights of numerous hard experiments has kept me (and many of my colleagues) sane and fighting to the last minute.

I am grateful to *Dr. Georgi Georgiev* under whose vigilant supervision I learned what is to be an experimentalist and more importantly how. I own to him much of my practical skills and experience with scientific equipment. His support has been crucial for my development as a physicist and in some particular occasions for my survival.

I would like to express my gratitude to *Prof. Dr. Rainer Neugart* from whom I learned most about the experimental technique. Moreover, a few key ideas in the supplement of this dissertation have been based on his experience and

valuable advices. I am grateful to *Prof. Dr. Peter Lievens* for the stimulating discussions. He has always been watchful for any imperfections in the experimental or analysis procedures, from which the measurements accuracy has benefited a number of times. I would like to thank him and *Prof. Dr. Nathal Severijns* for being members of my supervisory committee and answering many of my question about physics. I am grateful to *Prof. Dr. Klaus Blaum* for the constant support. He is a major driving force for our experiments with his knowledge and familiarity with the facilities. I have been trying to learn from him as much as possible and I look forward for further collaborations.

I am thankful to *Dr. Luis M. Fraile*, who did not spare efforts to put our experiments on track even when this involved taking action in the middle of the night. Many thanks go to the ISOLDE technical group and the laser ion source team for their support and professionalism.

To the people who ran IKS behind the curtains and made the scientific work possible - *Katia, Josee, Sally, Luc* and *Willy.* Thank you very much!

My special thanks go to all my colleagues. Some of you are doctors already, the others will soon become, so please let me use your first names only as I used to do all these years. *Nele, Marieke, Radomira, Iolanda, Magdalena, Dana, Ketel, Kieran, Stephen and* $2 \times$ *Pieter* - thank you all for your help, understanding and patience. I have shared the office, lab and data with you, but most importantly - many nice moments together! Please, do not change. I wish we will continue doing physics together.

My deepest gratitude goes to my parents, who unconditionally stood behind me and supported all my deeds through this journey. I wish to always see them so energetic and helpful (and only more often).
Моята най-дълбока признателност е отправена към моите родители, които бесусловно стояха зад мен и подкрепяха всичките ми начинания през цялото това пътешествие. Пожелавам си да ги виждам все така енергични и помагащи (и само по-често).

My most precious thank you goes to the most special person in my life - *Tanya.*

Мои близки, колеги, приятели и Писа, щастлив съм че когато „понякога все пак се срещаме“ всичко е отново така сякаш никога не съм напускал България. Благодаря ви!

20 April 2007 Деян Тодоров Йорданов

Measurement of the Spin and Magnetic Moment of ^{31}Mg: Evidence for a Strongly Deformed Intruder Ground State

G. Neyens,[1] M. Kowalska,[2] D. T. Yordanov,[1]
K. Blaum,[3] P. Himpe,[1] P. Lievens,[4] S. Mallion,[1] R. Neugart,[2] N. Vermeulen,[1]
Y. Utsuno,[5] and T. Otsuka[6]

[1]*Instituut voor Kern- en Stralingsfysica, Katholieke Universiteit Leuven, B-3001 Leuven, Belgium*
[2]*Institut für Physik, Universität Mainz, D-55099 Mainz, Germany*
[3]*CERN, Physics Department, CH-1211 Geneva 23, Switzerland*
[4]*Laboratorium voor Vaste-Stoffysica en Magnetisme, Katholieke Universiteit Leuven, B-3001 Leuven, Belgium*
[5]*Japan Atomic Energy Research Institute, Tokai, Ibaraki 319-1195, Japan*
[6]*Department of Physics and Center for Nuclear Study, University of Tokyo, Hongo, Tokyo 113-0033, Japan and RIKEN, Hirosawa, Wako-shi, Saitama 351-0198, Japan*

Unambiguous values of the spin and magnetic moment of ^{31}Mg are obtained by combining the results of a hyperfine structure measurement and a β-NMR measurement, both performed with an optically polarized ion beam. With a measured nuclear g factor and spin $I = 1/2$, the magnetic moment $\mu(^{31}\mathrm{Mg}) = -0.88355(15)\,\mu_N$ is deduced. A revised level scheme of ^{31}Mg ($Z = 12$, $N = 19$) with ground state spin/parity $I^\pi = 1/2^+$ is presented, revealing the coexistence of 1p-1h and 2p-2h intruder states below 500 keV. Advanced shell-model calculations and the Nilsson model suggest that the $I^\pi = 1/2^+$ ground state is a strongly prolate deformed intruder state. This result plays a key role for the understanding of nuclear structure changes due to the disappearance of the $N = 20$ shell gap in neutron-rich nuclei.

DOI: 10.1103/PhysRevLett.94.022501

PACS numbers: 21.10.-k, 23.20.-g, 27.30.+t, 32.10.Fn

Since Mayer and Jensen established the concept of shell structure in atomic nuclei, magic nucleon numbers have played a decisive role in describing the nuclear system [1]. About a quarter century later, the discovery of the anomalous ground state properties of ^{31}Na [2, 3] suggested that the magic shell structure can be broken. Shell-model calculations allowing particle-hole (p-h) excitations across the $N = 20$ shell gap proposed that a group of nuclei with deformed ground states appears between $Z = 10 - 12$ and $N = 20 - 22$. Because the p-h excited intruder states come lower in energy than the normal shell-model

states, this region has been called the "island of inversion" [4]. In fact, β-decay experiments [5, 6], intermediate energy Coulomb excitation [7], and in-beam γ-ray spectroscopy [8] confirmed the deformation of the even-even nuclei ^{30}Ne, ^{32}Mg and ^{34}Mg. Moment measurements revealed that also the ground state of the $N = 19$ nucleus ^{30}Na has an anomalous deformation [9] linked to this normal-intruder inversion [10]. The following questions thus arise: Where is the boundary between the normal *sd*-shell nuclei and nuclei having an intruder ground state, and does it clearly exist at all? This general intriguing question, about how widely nuclei with intruder ground states are spread and in what manner they become normal has not been answered, either experimentally or theoretically.

It has been suggested that the $N = 20$ shell gap is changing from one nucleus to another [11, 12] due to changes in the proton-neutron interaction. The boundary of the island of inversion can thus be shifted or smeared out, and intruder ground states might appear outside the earlier defined boundaries. Since the size of the shell gap is related to the single-particle energies [determined mainly by the monopole part of the nucleon-nucleon (NN) interaction], the mapping of the boundary is linked to one of the most basic and unanswered questions in present day nuclear structure physics: the microscopic mechanism to determine the monopole part of the NN interaction.

We present in this Letter a measurement of the ground state spin and magnetic moment of the exotic even-odd nucleus ^{31}Mg ($Z = 12$, $N = 19$). The earlier observed anomalous lifetime and the branching intensities in its β decay have never been explained [5, 13], although the high level density suggested the presence of intruder states at low excitation energy [14]. However, unambiguous spin/parity assignments are needed in order to establish the coexistence of normal *sd*-shell states with 1p-1h and 2p-2h intruder states. In addition to the ground state spin and parity, the magnetic moment value and sign provides direct information on the odd-neutron configuration.

The spin and magnetic moment of ^{31}Mg are measured by combining the results from two experimental techniques, based on the atomic hyperfine structure and on the nuclear interaction with external magnetic fields. Both methods rely on an optically polarized beam of ^{31}Mg^{+} ions which are implanted into a crystal, where the angular asymmetry in the β decay is detected. The experiments were performed at ISOLDE-CERN at the on-line collinear laser spectroscopy setup [15–17]. The ^{31}Mg beam was produced by bombarding a thick UC_2 target with 1.4 GeV protons (1.2×10^{13}/s on average) from the CERN PS-Booster. ^{31}Mg was selectively laser ionized with the resonance ionization laser ion source [18]. The ions were accelerated to 60 keV, and a mass separated ^{31}Mg^{+} beam with a typical intensity of 1.5×10^{5} ions/s (and less than 5% contamination from surface-ionized ^{31}Na) was guided to the collinear laser spectroscopy setup. The β-decay half-life was measured to be in agreement

with the earlier published value of 250(30) ms [5].

The Mg^+ ions are polarized through optical Zeeman pumping with a circularly polarized laser beam propagating along the ion beam. The polarization axis parallel to the laser beam is maintained by a weak magnetic guiding field over the interaction zone. Via the hyperfine interaction and adiabatic decoupling of the electron and nuclear spins, the resonantly induced electron polarization is partly transferred to the nucleus. The laser wavelength was set to the Doppler-shifted resonance value for the D_2 line ($3s^2S_{1/2} \leftrightarrow 3p^2P_{3/2}$; 35760.88 cm^{-1}). About 15 mW of UV power ($\lambda \approx 280$ nm) was obtained from an external-cavity frequency doubling ring, coupled to the output of a cw dye laser (Pyrromethene 556) which was pumped by an Ar^+ laser. By varying the velocity of the ions, applying a tunable high voltage to the interaction zone, the hyperfine structure was scanned. The optically induced resonances are observed through the asymmetry in the β decay of the polarized ^{31}Mg nuclei, after implantation into a MgO single crystal placed in a transverse magnetic field B. The coincidence counts from two β telescopes (each consisting each of two thin plastic scintillators), placed at 0° and 180° with respect to the magnetic field, allowed the normalized β-decay asymmetry $[N(0°) - N(180°)]/[N(0°) + N(180°)]$ to be deduced.

In Figs. 1(a) and 1(b) the β-decay asymmetry is shown as a function of the scanned acceleration voltage, for left-handed (σ^-) and right-handed (σ^+) polarized laser light. Apart from the sign changes in the resonance amplitudes, which depend on details of the optical pumping and decoupling process as explained in [9], the line positions are easily understood as arising from the different hyperfine structure components F of the atomic ground and excited states [Fig. 1(c)]. For example, the splitting between the $J = 1/2$ ground state levels equals $\Delta\nu(x) = A(x)[I(x)+1/2]$ and depends on the nuclear spin I. The hyperfine constant $A(x)$ depends on the nuclear g factor and the isotope independent magnetic hyperfine field H_e [15], $A(x) = g(x)\,\mu_N\,H_e/J$. To simulate the line positions, the hyperfine fields induced by the $^2S_{1/2}$ and $^2P_{3/2}$ electron states need to be known. These have been deduced from hyperfine-structure data on the stable isotope ^{25}Mg, reported from an optical pumping laser-rf double resonance experiment in a Penning trap [19]. The essential number is the $3s^2S_{1/2}$ magnetic hyperfine structure constant $A_{g.s.}(^{25}Mg) = -596.254376(54)$ MHz. Knowing the spin $I = 5/2$ and magnetic moment $\mu = -0.85545(8)\,\mu_N$ of ^{25}Mg [20], the hyperfine constant for ^{31}Mg can be deduced with the nuclear g factor as a parameter. Assuming the measured g factor (as described below) with a negative or a positive sign, this results in $A_{g.s.}(^{31}Mg) = \pm 3079.4(8)$ MHz. For a nuclear spin $I = 1/2$ this gives the line positions as shown in Figs. 1(d) and 1(e). The good agreement of Fig. 1(d) with the observed line splitting clearly decides for the ground state spin $I = 1/2$ and a negative g factor. Any other spin assumption would involve a much larger splitting, as shown in Fig. 1(f)

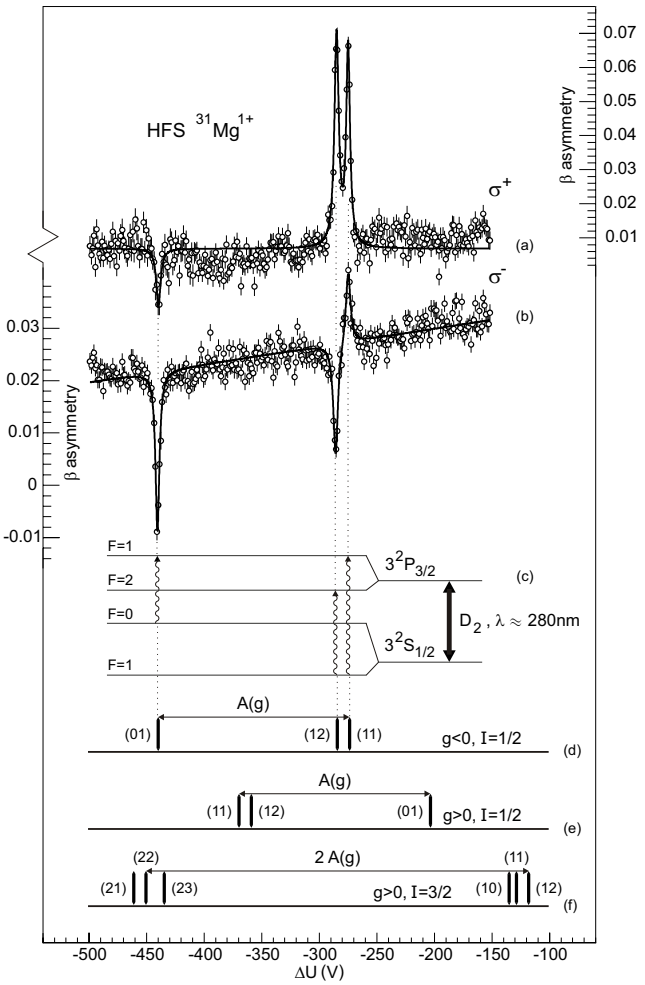

FIG. 1: (a), (b) Hyperfine spectra of σ^+/σ^- optically polarized $^{31}Mg^+$ ions, observed via the asymmetry in the nuclear β decay after implantation into MgO. (c) Hyperfine structure in the transition $3s^2S_{1/2} \rightarrow 3p^2P_{3/2}$ (D_2 line) assuming a nuclear spin $I = 1/2$. (d) - (f) Simulated spectra assuming $I = 1/2$ or $I = 3/2$, using the absolute g factor measured by NMR. The allowed transitions are labelled by the total angular momenta F of the ground- and excited-state hyperfine levels.

for the example of $I = 3/2$. The spin $I = 1/2$ is also manifest in the feature that only three resonances are detected in the hyperfine-structure scans. Now the adopted nuclear g factor remains to be confirmed by a nuclear magnetic

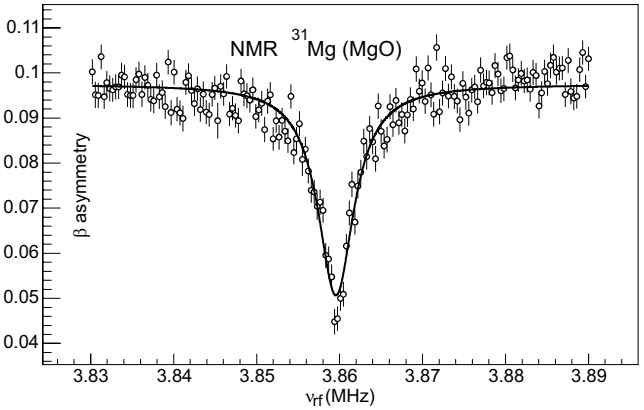

FIG. 2: Typical β NMR for ^{31}Mg implanted in MgO.

resonance (NMR) measurement.

Maximum polarization of the ^{31}Mg beam is obtained for σ^+ light*, with the Doppler-tuning voltage fixed to the resonance value of the (12) transition defined in Fig. 1(d). This is used for a NMR measurement on ^{31}Mg implanted into MgO. Resonant destruction of the nuclear polarization is induced by a rf magnetic field at the Larmor frequency $\nu_L = \mathrm{g}\,\mu_N\,B/h$. The resonance is recorded by measuring the β asymmetry as a function of the applied rf frequency, as shown in Fig. 2. In total, ten measurements have been performed for different rf powers, and a statistical average over the resonance positions was taken to obtain the Larmor frequency $\nu_L(^{31}\mathrm{Mg}) = 3859.73(18)$ kHz. To calibrate the magnetic field, we measured the NMR spectrum for a polarized ^{8}Li beam implanted in the same MgO crystal: $\nu_L(^8\mathrm{Li}) = 1807.03(2)$ kHz. From both Larmor frequencies, and using $\mathrm{g}(^8\mathrm{Li}) = 0.826780(9)$ [20], the absolute value of the ^{31}Mg g factor is deduced. This value needs to be corrected for diamagnetic shielding, using the numbers from Raghavan's table [20], resulting in $|\mathrm{g}(^{31}\mathrm{Mg})| = 1.7671(3)$. The error accounts for a possible 5 $\times 10^-5$ magnetic field drift over the 48 h period between the measurements and a similar uncertainty due to a possible difference in the beam positions on the crystal. This value, with a negative sign, gives the hyperfine-structure simulation of Fig. 1(d), confirming not only that the ground state spin of ^{31}Mg is $I = 1/2$ but also that the magnetic moment is negative, namely, $\mu(^{31}\mathrm{Mg}) = -0.88355(15)\,\mu_N$. The sign and magnetic moment value confirm the positive parity assigned to this $I = 1/2$ level (see further).

* There is a confusion in the original text between $\sigma^\pm$. A correction must be considered in Fig. 1, where (a) corresponds to σ^- and (b) to σ^+.

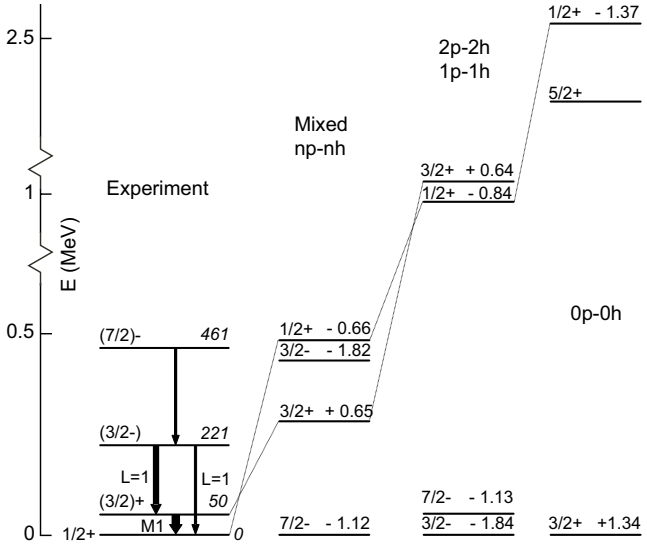

FIG. 3: Partial experimental level scheme of ^{31}Mg, with new spin/parity assignments, compared to various shell-model calculations (see text for details). The magnetic moments of theoretical levels are mentioned on the right (units μ_N).

Earlier β-decay experiments already assigned a positive parity to the ground state and most of the low-lying states, based on the fact that they are fed via the β decay from the positive parity ^{31}Na ground state [14]. One level at 461 keV was observed only via the β-delayed neutron decay of ^{32}Na ($N = 21$) and therefore assigned a negative parity. No firm spin assignments could be made. Now, with our ground state spin/parity $I^\pi(^{31}\text{Mg})=1/2^+$, we can make tentative spin/parity assignments to the first excited states of ^{31}Mg (Fig. 3) using the multipolarity assignments made by Klotz *et al.* [14]. The negative parity level at 461 keV is most likely the $I^\pi=7/2^-$ (1p-1h) intruder state, confirmed recently from a lifetime measurement on the 240 keV γ decay [21]. Further, the earlier observed hindered β decay to the ground state of ^{31}Al [14], known to have $I^\pi=5/2^+$ [22], can also be understood. A new measurement of the ^{31}Mg β decay has revealed an even weaker ground state feeding [23], as expected for a second forbidden $1/2^+$ to $5/2^+$ transition.

The level scheme is compared to recent shell-model calculations in Fig. 3. First we compare to a calculation performed with the USD interaction, where protons and neutrons are in the positive parity *sd* shell only [13]. The lowest $1/2^+$ state is in this case predicted around 2.5 MeV above the normal $3/2^+$ ground state (labeled 0p-0h in Fig. 3). The complete disagreement with the

observed high level density below 500 keV, including both positive and negative parity states, suggests the need to include neutron excitations into the negative parity pf shell [14]. Such calculations in the $sd-pf$ model space have been performed using two approaches.

With the ANTOINE shell-model code [12], using the interaction described in [24], calculations are performed in the full $sd-pf$ space. Intruder states are calculated by blocking, respectively, one or two neutrons in the pf shell (1p-1h, 2p-2h in Fig. 3), resulting in low-lying positive and negative parity states below 1 MeV. While the 1p-1h intruder states are predicted to occur well below the 2p-2h states (contrary to the experimental situation), these calculations do predict the correct ordering within each doublet ($1/2^+$ below $3/2^+$, and $3/2^-$ below $7/2^-$). The calculated magnetic moment (using free-nucleon g factors) of the pure 2p-2h $1/2^+$ intruder state is in good agreement with the observed value ($\mu = -0.84\,\mu_N$ compared to $\mu_{\rm exp} = -0.88355\,\mu_N$), suggesting that the wave function of the observed ground state is close to a pure 2p-2h intruder. The lowest $1/2^-$ state lies around 1.5 MeV and has a positive magnetic moment $\mu = +1.54\,\mu_N$.

Another set of calculations, including mixing between normal and intruder np-nh configurations have been performed with the Monte Carlo shell model (MCSM) [25] in the $sd-p_{3/2}f_{7/2}$ space ("mixed np-nh" in Fig. 3). The interaction for this model space is described in [26] and was used to describe a variety of nuclei, many of which have intruder dominant low-lying states [10, 26, 27]. While these mixed calculations reproduce better the high level density below 500 keV, they also cannot reproduce the correct ordering of the intruder levels. The magnetic moment for the $1/2^+$ level ($\mu = -0.66\,\mu_N$), dominated by more than 90% of 2p-2h intruder configurations, shows a less good agreement with experiment than for the pure 2p-2h state calculated with the interaction from [24]. This shows the sensitivity of the magnetic moment to small changes in the configuration, due to differences in the model space and single-particle energies.

The fact that the pure intruder calculations with the interaction from Ref. [24] predict the correct ordering within each doublet and reproduce better the magnetic moment than the calculations with the interaction from [26] may guide us to improve the interactions, particularly in their monopole and/or spin-isospin parts. The spacing between the 1p-1h and 2p-2h states is closely related to the $N = 20$ $sd-pf$ shell gap. The reduction of this gap from ^{40}Ca down to ^{32}Mg is different for the $sd-pf$ interaction (from 7.5 to 5.3 MeV) and the $sd-p_{3/2}f_{7/2}$ interaction (from 6 to 4 MeV). The better agreement of the MCSM calculations with the high experimental level density is an indication that indeed the shell gap is strongly reduced in the Mg isotopes. Such a reduced gap creates extensive particle-hole excitations from the sd-shell to the pf-shell, making ^{31}Mg rather soft against deformation and inducing a near degeneracy

of 1p-1h and 2p-2h states. In fact, in a Nilsson model picture, the $[200]\,1/2^+$ Nilsson orbit is occupied by the last neutron of ^{31}Mg for a large prolate deformation ($\beta \sim +0.4$). Thus, the present firm spin value suggests a strong prolate deformation of the ^{31}Mg ground state. This is confirmed by the shell-model calculations, where the quadrupole moment of the mixed np-nh and the pure 2p-2h states are calculated to be respectively Q($3/2^+$)= -13.6 and -14.6 $e\,\mathrm{fm}^2$ and with transition moments $B(E2;\, 3/2^+ \rightarrow 1/2^+) = 85$ and 87 $e^2\,\mathrm{fm}^4$. These $E2$ quantities are consistent with a prolate deformed $K = 1/2$ band having an intrinsic quadrupole moment $Q_0 \sim 65$ fm^2 and deformation $\beta \sim +0.44$.

In conclusion, we determined the spin/parity of the ^{31}Mg ground state as I^π=$1/2^+$ and present an updated level scheme with tentative spin/parity assignments to the lowest excited states. Calculations using the most recent shell-model interactions for the $sd-pf$ shell cannot reproduce the experimentally observed level ordering, but they predict the observed coexistence of 1p-1h and 2p-2h intruder configurations at low excitation energy. A comparison of the experimental magnetic moment with the calculations for pure intruder and mixed wave functions suggests that the observed $1/2^+$ ground state is a nearly pure 2p-2h intruder state, which in a Nilsson model approach is related to the strongly deformed $[200]\,1/2^+$ level.

The spin/parity assignments made in this work, together with the static moments of this and other odd-A nuclei, are thus providing a key element for further investigating the shell gap evolution in this region of the nuclear chart.

This work is part of the Ph.D. theses of M.K. and D.Y. We are very grateful to F. Nowacki, A. Poves and N.A. Smirnova for help with the ANTOINE calculations and fruitful discussions about the results. This work has been supported by the German Ministry for Education and Research (BMBF) under contract No. 06MZ175, by the IUAP project No. p5-07 of OSCT Belgium and by the FWO-Vlaanderen, by Grant-in-Aid for Specially Promoted Research (13002001) and for Young Scientists (14740176) from the MEXT of Japan. P.H. acknowledges financial support from IWT Flanders. The authors thank the ISOLDE technical group for their assistance.

[1] M.G. Mayer and J.H.D. Jensen, *Elementary Theory of Nuclear Shell Structure* (John Wiley and Sons, London, 1955).
[2] C. Thibault *et al.*, Phys. Rev. C **12**, 644 (1975).
[3] G. Huber *et al.*, Phys. Rev. C **18**, 2342 (1978).
[4] E.K. Warburton, J.A. Becker, and B.A. Brown, Phys. Rev. C **41**, 1147 (1990).
[5] C. Detraz *et al.*, Phys. Rev. C **19**, 164 (1979).
[6] D. Guillemaud-Mueller *et al.*, Nucl. Phys. **A426**, 37 (1984).
[7] T. Motobayashi *et al.*, Phys. Lett. B **346**, 9 (1995).
[8] B.V. Pritychenko *et al.*, Phys. Rev. C **63**, 011305(R) (2000).

[9] M. Keim *et al.*, Eur. Phys. J. A **8**, 31 (2000).
[10] Y. Utsuno *et al.*, Phys. Rev. C **70**, 044307 (2004).
[11] T. Otsuka *et al.*, Phys. Rev. Lett. **87**, 082502 (2001).
[12] E. Caurier, F. Nowacki, A. Poves, and J.Retamosa, Phys. Rev. C **58** (1998) 2033.
[13] B.H. Wildenthal, M.S. Curtin, and B.A. Brown, Phys. Rev. C **28**, 1343 (1983).
[14] G. Klotz *et al.*, Phys. Rev. C **47**, 2502 (1993).
[15] R. Neugart, Nucl. Instrum. Methods Phys. Res. **186**, 165 (1981)
[16] E. Arnold *et al.*, Phys. Lett. B **197**, 311 (1987).
[17] W. Geithner *et al*, Phys. Rev. Lett. **83**, 3792 (1999)
[18] U. Köster *et al.*, Nucl. Instrum. Methods Phys. Res., Sect. B **204**, 347 (2003).
[19] W.M. Itano and D.J. Wineland, Phys. Rev. A **24**, 1364 (1981).
[20] P. Raghavan, At. Data Nucl. Data Tables **42**, 189 (1989).
[21] H. Mach (private communication)
[22] D. Borremans *et al.*, Phys. Lett. B **537**, 45 (2002).
[23] F. Marechal (private communication)
[24] S. Nummela *et al.*, Phys. Rev. C **63**, 044316 (2001)
[25] T. Otsuka *et al.*, Prog. Part. Nucl. Phys. **47**, 319 (2001).
[26] Y. Utsuno, T. Otsuka, T. Mizusaki, and M. Honma, Phys. Rev. C **64**, 011301(R) (2001).
[27] Y. Utsuno, T. Otsuka, T. Mizusaki, and M. Honma, Phys. Rev. C **60**, 054315 (1999).

^{33}Mg: determination of a negative parity intruder ground state via nuclear moments

D. T. Yordanov,[1] M. Kowalska,[2,3] K. Blaum,[2] M. De Rydt,[1] K. Flanagan,[1,3] P. Lievens,[4] R. Neugart,[2] W. Nörtershäuser,[2] H. H. Stroke,[5] and G. Neyens[1]

[1]*Instituut voor Kern- en Stralingsfysica, Katholieke Universiteit Leuven, B-3001 Leuven, Belgium*
[2]*Institut für Physik, Universität Mainz, D-55099 Mainz, Germany*
[3]*CERN, Physics Department, CH-1211 Geneva 23, Switzerland*
[4]*Laboratorium voor Vaste-Stoffysica en Magnetisme, Katholieke Universiteit Leuven, B-3001 Leuven, Belgium*
[5]*Department of Physics, New York University, 4 Washington Place, New York, NY 10003, USA*

We report on the first unambiguous determination of the nuclear ground-state spin of ^{33}Mg, $I = 3/2$, achieved by combining laser spectroscopy with nuclear magnetic resonance techniques. The measured negative magnetic moment $\mu = -0.7456(5)\,\mu_N$ points to a 2p-2h intruder ground state and a negative parity. Discrepancies in the interpretation of former experimental studies are discussed and based on the firm spin-parity assignment from this work a corrected set of spins and parities is proposed for the known excited states. An interpretation is given within the deformed shell model and the particle plus rotor model. The results are consistent with an odd-neutron occupation of the 3/2 [321] Nilsson orbital at a large prolate deformation.

PACS numbers: 21.10.Hw, 21.10.Ky, 21.60.Cs, 27.30.+t, 32.10.Dk, 32.10.Fn

Since introduced in nuclear physics, the concept of shell structure and magic numbers has governed our understanding of nuclear matter in atomic nuclei close to stability. With obtaining an access to more exotic species we could follow the nuclear structure evolution towards extreme isospin values, in particular with increasing the neutron excess in light systems. The onset of deformation in nuclei with a closed neutron *sd*-shell was discovered via the extra binding energy and anomalous spin of ^{31}Na [1, 2], and the low-lying first 2_1^+ state in ^{32}Mg [3, 4]. Nuclear-reaction experiments directly determined large prolate deformations in the three $N = 20$ isotones ^{30}Ne [5], ^{31}Na [6] and ^{32}Mg [7–9]. The observed phenomena are understood as an inversion of the normal spherical ground-state configurations, expected for these nuclei according to the traditional shell model, with deformed, "intruder", states governed by particle-hole excitations over the $N = 20$ shell gap. Including Ne, Na and

Mg isotopes, the "Island of inversion" initiates with ^{28}Ne [8, 10], ^{29}Na [11–13] and exhibits a sharp boundary between ^{30,31}Mg [14, 15]. Being inside the island, where different particle-hole excitations coexist at low energies, the ^{33}Mg ground state needs to be probed experimentally. A β-decay study [16] suggests a 1p-1h ground-state configuration with spin and parity $I^\pi = 3/2^+$ in contrast to $I^\pi = 5/2^+$ from intermediate energy Coulomb excitation [17] and proton inelastic scattering [18] experiments. The systematics of nuclear moments in the region [19] and studies of the neighboring even-even Mg isotopes [7, 8, 20, 21] point to a 2p-2h ground state. This fact and the discrepancy in the spin assignment served as a motivation to measure the spin and magnetic moment of ^{33}Mg and thus unambiguously determine its ground-state configuration. This is of high importance for the theoretical modeling of the region, since the strong competition between 1p-1h and 2p-2h configurations is directly related to the size of the $N = 20$ shell gap.

The neutron rich ^{31,33}Mg were produced in a fragmentation reaction at ISOLDE - CERN [22] by 1.4 GeV protons from the Proton Synchrotron Booster impinging on a thick UC_x/graphite target. Their lifetimes [23, 24] enabled the use of the shortest cycle of 2×10^{13} protons every 1.2 s. When the primary beam was shared with other experiments the highest pulse intensity of 3×10^{13} protons every 2.4 s was used. Laser ionization was applied to chemically select Mg [25] with an average yield of 2.5×10^3 ions/μC for ^{33}Mg. The radioactive beams were accelerated to 40 or 50 keV, mass analyzed and delivered to the Collinear Laser Spectroscopy Setup (COLLAPS) [11, 26, 27].

The probe's Hyperfine Structure (HFS) and nuclear gyromagnetic ratio are measured by employing Laser Spectroscopy and Nuclear Magnetic Resonance (NMR). The singly ionized Mg (Mg II) resonantly interacts with a circularly polarized UV laser radiation. Optical pumping takes place, polarizing the atomic spins in the direction of the photons momentum, parallel to an applied weak magnetic field of ≈ 0.6 mT. A strong magnetic field of ≈ 0.3 T, perpendicular to the propagation axis, is causing a decoupling of the electronic and nuclear angular momenta and resulting in a nuclear polarization. After implantation in a cubic crystal, the β-decay anisotropy is monitored with two telescopes of thin scintillators, placed at 0° and 180° with respect to the orientation axis. The experimental β asymmetry $\left[N\left(0°\right) - N\left(180°\right)\right] / \left[N\left(0°\right) + N\left(180°\right)\right]$, constructed from the coincidence events, is measured as a function of the laser frequency in the reference frame of the atomic beam or as a function of an external Radio Frequency (RF) field.

The Doppler shifted laser frequency is scanned in the D_2 line (279.635 nm for Mg [28]), inducing transitions between the $3^2S_{1/2}$ and $3^2P_{3/2}$ hyperfine multiplets, as shown in Figs. 1 (a) and (e). The experimental spectra of ^{33}Mg II, obtained with σ^- and σ^+ laser polarization are displayed in Fig. 1 (b) and (c), respectively. The frequency scale is given relative to the fine-structure splitting

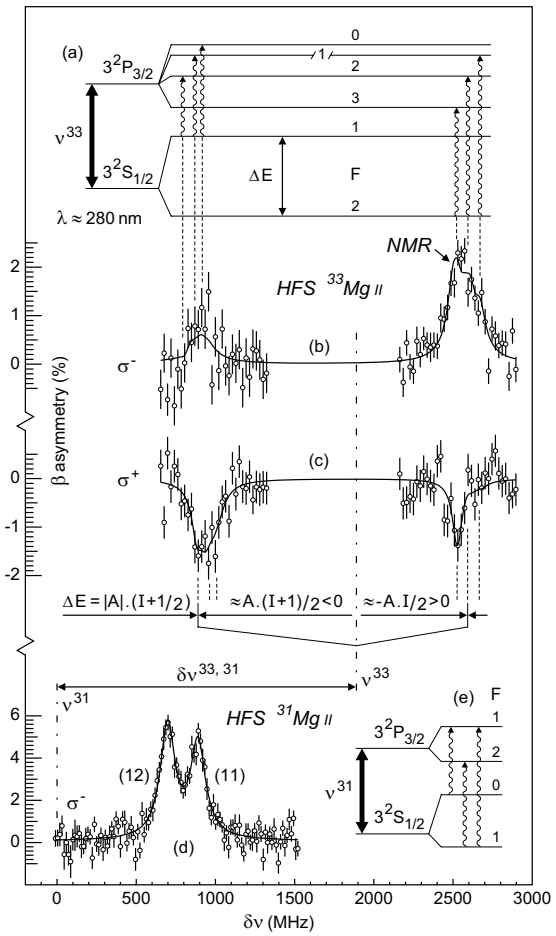

FIG. 1: (a) Principle hyperfine structure in the D_2 line for $I = 3/2$ and $A < 0$; (b), (c) Realistic fits of the β-asymmetry spectra of σ^- and σ^+ polarized ^{33}Mg II in the D_2 line, after implantation into MgO; (d) β-asymmetry spectrum of σ^- polarized ^{31}Mg II ($I = 1/2$, $A < 0$) in the D_2 line, implanted into MgO; (e) HFS scheme corresponding to (d). The transition $F : 0 \rightarrow 1$ falls outside the frequency range of the figure;

of the reference ^{31}Mg II ($I = 1/2$ [15]). The distance between the two groups of resonances in ^{33}Mg II is determined by the splitting ΔE in the $3^2S_{1/2}$ multiplet. This direct observable is related to the nuclear spin I and magnetic dipole hyperfine parameter A with the equation: $\Delta E = |A|\,(I + 1/2)$. The ratio A/g, where g is the nuclear g factor, is constant for an isotopic chain and has a

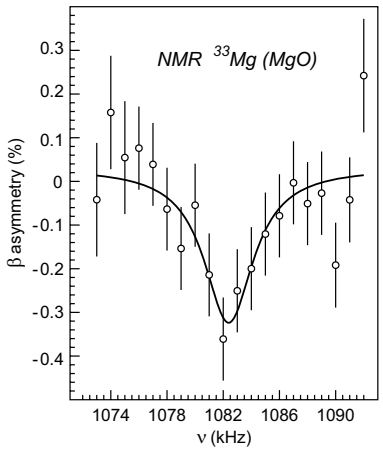

FIG. 2: NMR spectrum of ^{33}Mg implanted into MgO, representing 34 % of the total statistics.

positive sign for alkali-like atoms [29]. The precise A/g value is established for Mg II by the experimental work on the stable ^{25}Mg II [30, 31]. Thus a g-factor measurement in ^{33}Mg leads to the determination of A, which in combination with the HFS splitting yields the nuclear ground-state spin. Magnetic resonance measurements were carried out with σ^- polarized light in the higher frequency triplet of transitions [Fig. 1 (b)] after implantation into the cubic crystal lattices of MgO (fcc) and Pt (ccp). The produced experimental asymmetry was ≈ 2 %. A radio frequent magnetic field of a few tenths of a mT was applied perpendicularly to the static magnetic field B. In the vicinity of the Larmor frequency $\nu_L = \mathrm{g}\, B\, \mu_N/h$ the experimental asymmetry is reduced by the resonant absorption of photons from the RF field. An example NMR spectrum of ^{33}Mg in MgO, obtained with a small sinusoidal frequency modulation with an amplitude of 1 kHz, is presented in Fig. 2. The total statistics includes spectra of similar quality in Pt. The reference probe ^{31}Mg was implanted in both hosts in order to extract the ratio of the Larmor frequencies, which is independent of the chemical and Knight shifts. The nuclear gyromagnetic ratio of ^{33}Mg, found in such manner, is $\left|\mathrm{g}\left(^{33}\mathrm{Mg}\right)\right| = 0.4971(4)$. The error includes a systematic uncertainty due to a possible drift of the static magnetic field. This specific value of the g factor, together with the measured HFS splitting ΔE, fix the ^{33}Mg ground-state spin to $I = 3/2$.

The isotope shift between ^{31,33}Mg II, using the total mass shift from Ref. [32], was calculated to be $\delta\nu^{33,31} = 1867$ MHz. The uncertainty on this number, including the errors on the mass shift and an unknown change between the

mean-square charge radii, is estimated to be smaller than 50 MHz. Based on the isotope shift one can plot the fine-structure splitting of ^{33}Mg II relative to the transitions of the hyperfine structure, the so-called "center of gravity". The latter is represented by the alternating dash-dot line ν^{33} in Fig. 1. The transitions starting from the higher angular momentum state $F = I + 1/2$ ($F = 2$ for $I = 3/2$) are always closer to the center of gravity. In the case of ^{33}Mg II their resonances appear at the higher frequency side of the spectra meaning that they start from the lower energy level. Since the levels in $3^2S_{1/2}$ are inverted the magnetic dipole hyperfine parameter has a negative sign. This conclusion is independently confirmed by the theoretical polarization function [11, 33], represented by the fitted curves in Figs. 1 (b) and (c). Since the ratio A/g is positive, the ground-state g factor of ^{33}Mg is negative, resulting in a negative nuclear magnetic moment $\mu(^{33}\mathrm{Mg}) = \mathrm{g}\, I\, \mu_N = -0.7456(5)\, \mu_N$.

The ground-state configuration of $^{33}_{12}\mathrm{Mg}_{21}$ suggested in Ref. [16] is characterized by spin and parity $I^\pi = 3/2^+$, associated with 1p-1h excitation over the $N = 20$ shell gap. In the extreme shell-model picture, the properties of such a state are determined by an odd neutron in the $\nu\, 1d_{3/2}$ orbital, which has a positive single-particle magnetic moment. In order to explain the experimental negative sign of the magnetic moment, an odd number of neutrons must occupy the pf-shell, as these have negative Schmidt values for the orbitals $\nu\, 1f_{7/2}$ and $\nu\, 2p_{3/2}$. In this simplified manner one already arrives with the conclusion that the ground-state parity of ^{33}Mg is negative, determined by the negative parity of the latter two orbitals.

Large-scale shell-model calculations are carried out in the *sd–pf* model space with the code Oxbash [36], using the Hamiltonians from Refs. [34, 35], designed specifically for the island of inversion. Mixing of states with a different number of particle-hole excitations ($\hbar\omega$) is not considered. The neutron configuration space is reduced to $\nu\,(sd{-}1f_{7/2}{-}2p_{3/2})$, as it is commonly undertaken in this

TABLE I: Gyromagnetic ratios and quadrupole moments of different particle-hole excitations in ^{33}Mg ($I = 3/2$), calculated with the interactions WBMB [34] and SD − PF [35]. Free-nucleon g factors are used and effective charges $e_\pi = 1.5\, e$ and $e_\nu = 0.5\, e$.

		WBMB		SD − PF	
$n\,\hbar\omega$	I^π	g_{free}	Q (mb)	g_{free}	Q (mb)
0	$3/2^-$	−1.47	−83	−1.35	−91
1	$3/2^+$	0.75	135	0.78	140
2	$3/2^-$	-0.45^a	147^b	-0.47^a	157^b

[a] Experimental gyromagnetic ratio from this work g = −0.4971(4).
[b] $Q(\beta_\mathrm{C}) = 151(38)$ mb, calculated from β_C [17].

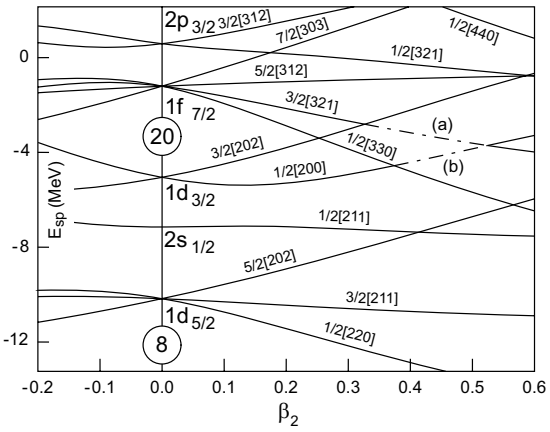

FIG. 3: Nilsson diagram in the $\nu\,(sd-1f_{7/2}-2p_{3/2})$ configuration space. (a), (b) Odd neutron occupation in the ground state of ^{33}Mg and ^{31}Mg, respectively.

region [12, 15, 20, 34, 35]. Two out of four valence protons are fixed on the $\pi\,1d_{5/2}$ orbital. The other two are confined within the *sd*-shell. Calculated nuclear moments of different particle-hole excitations (0, 1 and $2\,\hbar\omega$) with spin 3/2 are presented in Tab. I. Clearly, the experimental g factor is only consistent with the 2p-2h configuration. Furthermore, the good agreement between the theoretical and experimental values indicates that the ground state of ^{33}Mg is a nearly pure 2p-2h intruder.

The charge distribution deformation of ^{33}Mg has been determined via Coulomb excitation to be $\beta_{\rm C} = 0.52(12)$ [17]. This number only slightly depends on the assumed initial and final spin values ($5/2^+ \rightarrow 7/2^+$) in that study. An axially symmetric rotor with a ground-state spin $I = K = 3/2$ has a spectroscopic quadrupole moment directly related to the deformation parameter, as described in Ref. [37]. The obtained model-dependent value $Q = 151(38)$ mb is in good agreement with the theoretical number for the $2\,\hbar\omega$ state in Tab. I. In a Nilsson model picture the Fermi level for $N = 21$ coincides with an orbital having spin and parity $I^\pi = 3/2^-$ for a deformation in the interval $0.33 \lesssim \beta_2 \lesssim 0.52$. This is represented in Fig. 3 by the dashed section (a) of the $3/2\,[321]$ orbital. The established range is in good agreement with the matter deformation $\beta_{\rm M} = 0.47(8)$ from a proton inelastic scattering study [18]. The neighboring even-even ^{32,34}Mg exhibit similar charge deformations, in accordance with Refs. [7–9] and [21], respectively. Analogous deformation parameters are determined for ^{31}Mg [15], as shown in Fig. 3 (b), ^{31}Na [6] and ^{30}Ne [5]. Altogether, the result of this work appears to be consistent with the systematics in the island of inversion.

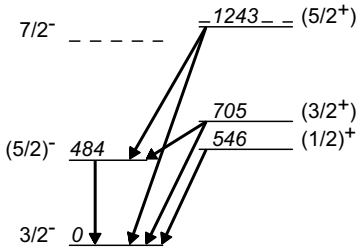

FIG. 4: Experimental level scheme of ^{33}Mg: two rotational bands with $K^\pi = 3/2^-$ and $K^\pi = 1/2^+$ (see the text).

In an attempt to compile the current experimental facts in a coherent interpretation, we adopt the energy levels at 484, 705 and 1243 keV, identified in the β decay of ^{33}Na [4, 16], and propose a different set of spin-parity assignments. In the latter work [16] a suggestion is made that since the most intense γ in ^{33}Mg of 546 keV is not found in coincidence with any of the other transitions it must connect the 705 keV level with an isomeric state at 159 keV. The decay of this state has not been observed within their coincidence window of 500 ns, thus setting a lower limit for the lifetime of the isomer and consequently demanding a spin of at least two units greater than the spin of the ground state. Reaction experiments [17, 18] consistently provide evidence that the parity of the 484 keV level is identical to the parity of the ground state, contrary to Ref. [16]. This level is suggested in Ref. [17] to be a rotational excitation, which according to our firm spin-parity assignment to the ground state results in spin and parity $5/2^-$ of the first excited state. The transition from the 484 keV level to the isomer, which has the same multipolarity as the transition to the ground state, has not been experimentally observed. Based on this fact we consider the hypothesis of having an isomer very unlikely and postulate a level at 546 keV. The modified level scheme is presented in Fig. 4. We reject the claim of a large β branch to the ground state, which we regard as the source of inconsistencies between Ref. [16] on one side and the present work, as well as Refs. [17, 18], on the other. Here the ground-state parity of ^{33}Na is considered positive, based on analogy with ^{31}Na ($I^\pi = 3/2^+$ [2]) and shell-model calculations predicting either $0\,\hbar\omega$ or $2\,\hbar\omega$ configurations. The most likely interpretation of the available experimental evidence is that the observed excited states in ^{33}Mg originate from two rotational bands - one with $K^\pi = 3/2^-$ based on the $3/2\,[321]$ Nilsson orbital and another with $K^\pi = 1/2^+$ based on the $1/2\,[200]$ orbital, both at a large prolate deformation. This interpretation is consistent with the spin-parity change between ^{31}Mg ($I^\pi = 1/2^+$) and ^{33}Mg ($I^\pi = 3/2^-$). The dashed lines in Fig. 4, both being close to the

experimental level at 1243 keV, represent the calculated third members in each of the bands. The $\log ft$ value associated with this state is relatively low [16], suggesting that it belongs to the positive parity band.

In summary, the nuclear ground-state spin and magnetic moment of ^{33}Mg have been experimentally determined to be $I = 3/2$ and $\mu = -0.7456(5)\,\mu_N$. This is the first magnetic-moment measurement for a nucleus with 21 neutrons in the island of inversion. Shell-model calculations reveal the 2p-2h nature of the ground state and associate it with a negative parity. The result is consistent with a large prolate deformation, based on the $3/2\,[321]$ Nilsson orbital. A corrected level scheme with tentative spin-parity assignments is proposed, combining our firm spin-parity assignment to the ground state with the available evidence from other experimental studies.

We are grateful to B. A. Brown for sharing ideas and valuable insights of Oxbash, as well as to A. Poves for the discussion at the ISOLDE workshop. We acknowledge G. Rainovski for providing the Nilsson diagram. The authors would like to thank the ISOLDE technical group for their professional assistance. This work has been supported by FP6-EURONS project nr. RII3-CT-2004-506065, the IUAP project P5/07 of OSCT Belgium, the FWO-Vlaanderen and the German Federal Ministry for Education and Research (BMBF).

[1] C. Thibault *et al.*, Phys. Rev. C **12**, 644 (1975).
[2] G. Huber *et al.*, Phys. Rev. C **18**, 2342 (1978).
[3] C. Détraz *et al.*, Phys. Rev. C **19**, 164 (1979).
[4] D. Guillemaud-Mueller *et al.*, Nucl. Phys. **A426**, 37 (1984).
[5] Y. Yanagisawa *et al.*, Phys. Lett. B **566**, 84 (2003).
[6] B. V. Pritychenko *et al.*, Phys. Rev. C **63**, 011305(R) (2000).
[7] T. Motobayashi *et al.*, Phys. Lett. B **346**, 9 (1995).
[8] B. V. Pritychenko *et al.*, Phys. Lett. B **461**, 322 (1999).
[9] V. Chisté *et al.*, Phys. Lett. B **514**, 233 (2001).
[10] H. Iwasaki *et al.*, Phys. Lett. B **620**, 118 (2005).
[11] M. Keim *et al.*, Eur. Phys. J. A **8**, 31 (2000).
[12] Y. Utsuno, T. Otsuka, T. Mizusaki, and M. Honma, Phys. Rev. C **70**, 044307 (2004).
[13] V. Tripathi *et al.*, Phys. Rev. Lett. **94**, 162501 (2005).
[14] O. Niedermaier *et al.*, Phys. Rev. Lett. **94**, 172501 (2005).
[15] G. Neyens *et al.*, Phys. Rev. Lett. **94**, 022501 (2005).
[16] S. Nummela *et al.*, Phys. Rev. C **64**, 054313 (2001).
[17] B. V. Pritychenko *et al.*, Phys. Rev. C **65**, 061304(R) (2002).
[18] Z. Elekes *et al.*, Phys. Rev. C **73**, 044314 (2006).
[19] G. Neyens *et al.*, Eur. Phys. J. A (2007), (proceedings to RNB7 in progress).
[20] A. Poves and J. Retamosa, Phys. Lett. B **184**, 311 (1987).
[21] H. Iwasaki *et al.*, Phys. Lett. B **522**, 227 (2001).

[22] http://isolde.web.cern.ch.
[23] F. Maréchal *et al.*, Phys. Rev. C **72**, 044314 (2005).
[24] A. C. Morton *et al.*, Phys. Lett. B **544**, 274 (2002).
[25] U. Köster *et al.*, Nucl. Instr. and Meth. in Phys. Res. B **204**, 347 (2003).
[26] D. T. Yordanov *et al.*, Balk. Phys. Lett. p. 358 (2004), ISSN 1301 - 8329.
[27] M. Kowalska *et al.*, Eur. Phys. J. A **25**, s01, 193 (2005).
[28] V. Kaufman and W. C. Martin, J. Phys. Chem. Ref. Data **20**, 83 (1991).
[29] H. Kopfermann and E. E. Schneider, *Nuclear Moments* (Academic Press Inc., 1958).
[30] W. M. Itano and D. J. Wineland, Phys. Rev. A **24**, 1364 (1981).
[31] F. Alder and F. C. Yu, Phys. Rev. **82**, 105 (1951).
[32] M. Kowalska, Ph.D. thesis, Johannes Gutenberg Univ. Mainz (2006).
[33] D. T. Yordanov, Ph.D. thesis, Katholieke Universiteit Leuven (2007), (in preparation).
[34] E. K. Warburton, J. A. Becker, and B. A. Brown, Phys. Rev. C **41**, 1147 (1990).
[35] S. Nummela *et al.*, Phys. Rev. C **63**, 044316 (2001).
[36] B. A. Brown *et al.*, MSU - NSCL report 1289.
[37] A. Bohr and B. R. Mottelson, *Nuclear Structure*, vol. 2 (W. A. Benjamin, Inc., 1975), p. 45 - 47.

B A L K A N P H Y S I C S L E T T E R S ISSN 1301 - 8329, 358 (2004)

SPIN AND MAGNETIC MOMENT OF OPTICALLY POLARIZED ^{31}Mg DETERMINED VIA β-DECAY ASYMMETRY MEASUREMENTS

D.YORDANOV, M.KOWALSKA,**, K.BLAUM**, P.HİMPE, P.LİEVENS***, S.MALLİON, N.VERMEULEN, R.NEUGART* and G.NEYENS*

Instituut voor Kern- en Stralingsfysica, K.U.Leuven, Leuven, Belgium
** Insititut für Physik, Universität Mainz, Mainz, Germany*
*** CERN, Physics Department – IS, Geneva, Switzerland*
**** Laboratorium voor Vaste-Stoffysica en Magnetisme, K.U.Leuven, Leuven, Belgium*

ABSTRACT

The results from a recent measurement of the ground-state spin and magnetic moment of ^{31}Mg are presented. The g-factor value is obtained via nuclear magnetic resonance to be $|g(^{31}Mg)| = 1.7671(3)$. Comparison between the hyperfine splitting in $3^2S_{1/2}$ of $^{31,25}Mg^{1+}$ unambiguously determines the ground-state spin $I(^{31}Mg) = 1/2$ and fixes negative sign to the magnetic moment, which combined with the precise value of the g factor, yields $\mu(^{31}Mg) = -0.88355(15)\ \mu_N$. Spins and parities are assigned to the first four levels according to former β-decay studies and comparison with advanced shell-model calculations. Based on the calculations and the Nilsson model a significant prolate deformation is deduced for the ground state of ^{31}Mg.

Keywords: ^{31}Mg, NMR, Spin, Magnetic moment

Introduction

This study is instigated by the interesting phenomenon taking place for neutron rich Na and Mg isotopes around N = 20. There are experimental evidences for deformation and breaking of the shell structure in the region, although these nuclei have a number of neutrons close to a magic number. First, online mass spectrometry suggested the onset of deformation in ^{31,32}Na [1]. Later on, β-decay studies of neutron rich Na isotopes suggested the deformation of ^{32}Mg [2,3]. A direct quadrupole moment measurement indeed confirmed the deformation of ^{30}Na [4]. It is presently established that ^{30}Ne and ^{34}Mg are also deformed. The deformation has been attributed to the fact that the ground states of these nuclei are "intruder states" - with wave functions dominated by particle-hole excitations over the shell gap. With reducing the N = 20 shell gap, these states could decrease in energy and even become the ground state. The earliest shell-model calculations, taking into account (p-h) excitations from the sd to the pf shell, predicted the deformation region to be within the limits ($10 \leq Z \leq 12$ & $20 \leq N \leq 22$), while more recent calculations

enclose different boundaries depending on the used parametrization of the interaction. Since these are exotic nuclei, which became available for research the last years, the borderlines of the so-called "Island of Inversion" are not experimentally revealed - ^{31}Mg in particular. The measured spin and magnetic moment of this nucleus give a valuable contribution to the understanding of the nuclear structure in the region.

Experimental technique

The ions of the neutron rich ^{31}Mg are produced at ISOLDE-CERN [5] in nuclear reactions induced by high energy protons (1.4 GeV) impinging on a UC_2 target. The "chemical" selectivity of the laser ion source RILIS, is used to ionize the Mg atoms [6], making possible their extraction from the ion source with an electrostatic potential of 60 keV. The Mg isotopes are mass separated with the general purpose separator (GPS) and delivered to the collinear laser spectroscopy setup COLLAPS [7] (Fig. 1.).

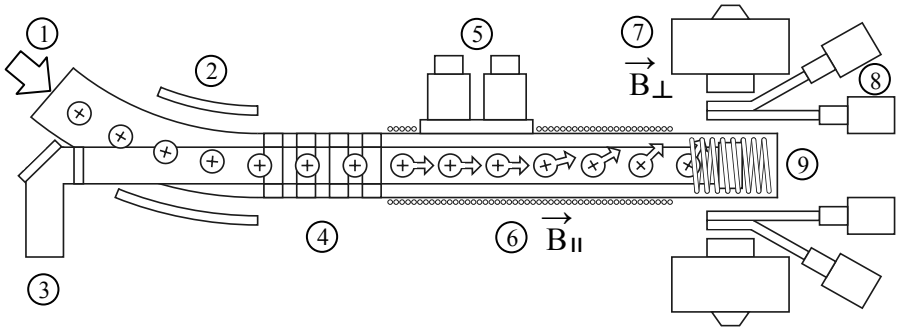

Fig. 1. *Collaps; 1.)Incoming 1^+ ions; 2.)Ion-beam deflection; 3.)UV-laser beam; 4.)Post-acceleration lenses; 5.)Optical detection; 6.)Coils-weak magnetic field; 7.)Magnet-strong field; 8.)β detectors; 9.)RF Coil;*

After a deflection of 10° the ion beam coincides with a UV-laser beam close in frequency to the atomic transitions between the $3^2S_{1/2}$ and either $3^2P_{1/2}$ or $3^2P_{3/2}$ hyperfine multiplets (D_1 and D_2 lines respectively). By applying an additional acceleration, the Doppler shifted frequency (1.1) sensed by the ions is scanned through all the transitions of the hyperfine structure in the investigated line.

$$\nu = \nu_0 \sqrt{(1 - v/c)/(1 + v/c)} \qquad (1.1)$$

The exotic ^{31}Mg is studied via its β decay. A section with a weak magnetic field causes the Zeeman splitting of the F quantum states (***F*** = ***I*** + ***J***), which ensures the optical pumping between the m_F states. The produced atomic polarization is maintained during the adiabatic transition from the weak longitudinal to the strong transverse magnetic field, provided that the nuclear and electronic spins do not

decouple. The nuclear spin orientation is maintained after implantation in a suitable crystal (MgO with a cubic lattice structure) due to the strong field. The asymmetry in the β-scintillation detectors (1.2) reflects the nuclear polarization (1.4) according to the angular distribution of the β radiation of a polarized ensemble (1.3).

$$a = \left[N\left(0^0\right) - N\left(180^0\right) \right] / \left[N\left(0^0\right) + N\left(180^0\right) \right] \tag{1.2}$$

$$W\left(\theta\right) = 1 + \left(\mathrm{v}/c\right) AP\cos\left(\theta\right) \tag{1.3}$$

$$P = \sum_{m_I} p\left(m_I\right) m_I / I \tag{1.4}$$

Applying a radiofrequency field, corresponding to the equidistant energy splitting of the nuclear Zeeman levels (1.5), changes their population, which destroys the polarization and with that the observed asymmetry.

$$\Delta E = h\nu_L = g_I \mu_N B \tag{1.5}$$

Results

Multiple observations of the low-lying hyperfine structure of $^{31}Mg^{1+}$ are done with left and right circularly polarized laser light. In the example spectra shown in Fig. 2 a) and b) one can clearly identify three transitions of the D_2 line ($3^2S_{1/2} \rightarrow 3^2P_{3/2}$). According to the selection rule $\Delta F = 0, \pm 1$, such a number of resonances occurs only for spin 1/2. This is not considered as a proof, since at certain conditions, no polarization is created for some of the transitions. In the D_1 line for instance F: 1→1 was observed with only one polarization of the laser light. Following the first evidence on the spin, we performed a NMR measurement in the region predicted by shell-model calculations for $1/2^+$ intruder ground state (Fig. 2. f). The measured resonance frequency is $\nu_L(^{31}Mg)$ = 3859.73(18) kHz. In order to have a magnetic field calibration of at least the same precision, ^8Li is implanted in the same crystal (MgO) and investigated with NMR 48 hours later: $\nu_L(^8Li)$ = 1807.03(2) kHz (Fig. 2. g). The g factor of the reference ^8Li is known with a high precision $g(^8Li)$ = 0.826780(9) [8]. Considering proper corrections for the diamagnetic shielding of the electrons [8] and $\times 10^{-4}$ additional error accounting for a possible drift of the magnetic field and a change of the beam position on the crystal over the time period we deduce $|g(^{31}Mg)|$ = 1.7671(3). The hyperfine parameters in the same multiplet of two isotopes and their g factors are related (1.6). Knowing that ^{25}Mg has a negative g factor $g(^{25}Mg) = -0.342180(32)$ [8] and a negative hyperfine constant $A(^{25}Mg) = -596.254376(54)$ [9] in $3^2S_{1/2}$, one requires the same sign for the g factor of ^{31}Mg as for its hyperfine constant.

$$A_1 / A_2 = g_1 / g_2 \tag{1.6}$$

If the levels F = 1 and F = 0 in $3^2S_{1/2}$ (Fig. 2. c) are interchanged, than the single transition F: 0→1 would have higher energy than the other two and would occur on the right side of the spectrum. Since it is on the left side, we conclude a negative sign for the hyperfine constant and the g factor of ^{31}Mg. For J = 1/2 the ground state splitting is |A|(I + 1/2). It has been calculated for spins 1/2 and 3/2, using the A

factor derived with (1.6), in order to proof that 1/2 is the nuclear spin corresponding to the observed HFS (Fig. 2. d, e). From the firm g factor and spin the magnetic moment is derived $\mu(^{31}\mathrm{Mg}) = -0.88355(15)\ \mu_N$.

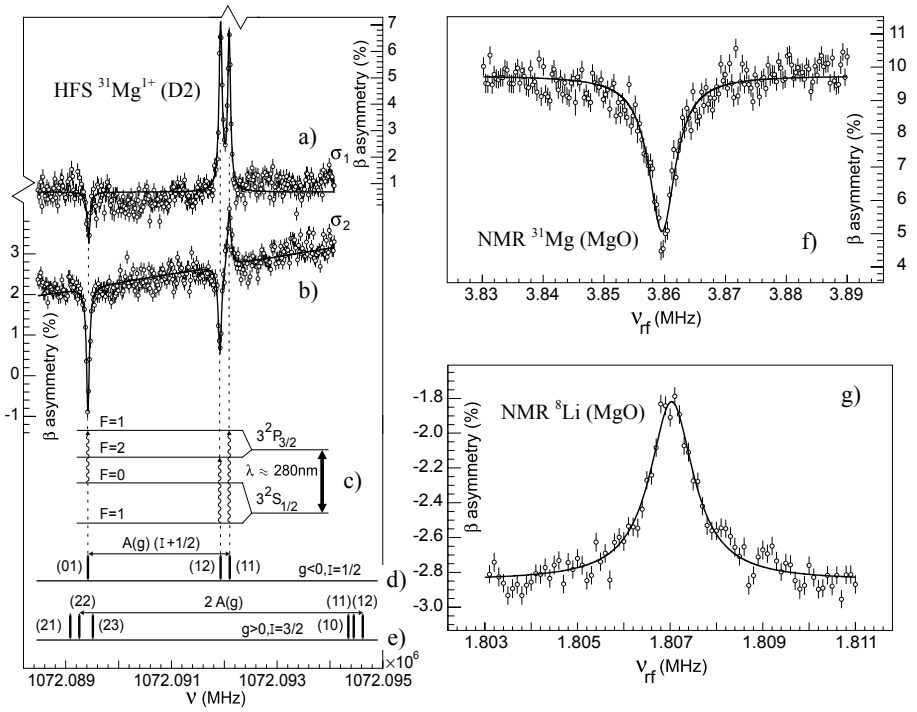

Fig. 2. a, b)HFS of $^{31}Mg^{1+}$ in the D_2 line with different laser polarization; c)HFS of $^{31}Mg^{1+}$ - level scheme; d, e)Transitions calculated from g(^{31}Mg), g(^{25}Mg) and HFS of $^{25}Mg^{1+}$ with assumption of the nuclear spin 1/2 and 3/2, respectively; f)NMR of ^{31}Mg in MgO; g)NMR of ^{8}Li in MgO;

Discussion

A scheme of the first four states in ^{31}Mg as they are fed in the β decay of ^{31,32}Na [10] is shown in Fig. 3. The reported log *ft* values corresponding to the first two levels are 4.9 and 5.6, respectively, which suggests that they are populated via an allowed β decay and accordingly no change of parity is expected. The ^{31}Na ground state is investigated with laser spectroscopy and tentatively assigned the spin 3/2 [11]. According to shell-model calculations [12] positive parity is accepted and this suggests positive parity for the first two levels in ^{31}Mg. The $1/2^+$ magnetic moment obtained with the ANTOINE code for a pure 2p-2h intruder closely reproduces the measured value, while the one for $1/2^-$ is in disagreement [13]. Since they are fed

through one neutron emission from the ^{32}Na ground state, negative parity is suggested for the 221 and 461 keV levels [10] (the multipolarity assignments come from the same study).

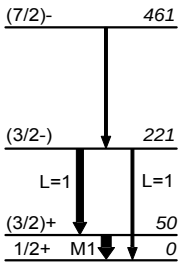

Fig. 3. Partial level scheme of ^{31}Mg.

Knowing the spin and parity of the ground state of ^{31}Mg, we have been able to assign spins and parities to the four lowest levels, showing that all of them are intruder states (with a strong competition between 1p-1h and 2p-2h wave functions) [13]. The intruder nature of the $1/2^+$ ground state follows directly from the large-scale shell-model calculations, which predict this level around 500 keV with a large intrinsic quadrupole moment. The Nilsson orbital 1/2[200] becomes the Fermi level for $\beta > 0.3$ and also suggests considerable prolate deformation for the ^{31}Mg ground state. The discussed results are important for the understanding of the competition between normal (0p-0h), and intruder (1p-1h,…, np-nh) states at low energy in this mass region and for determining more accurately the changing N = 20 shell gap as a function of isospin.

References

[1] C. Thibault *et al.*, Phys. Rev. **C 12**, 644 (1975)
[2] C. Detraz *et al.*, Phys. Rev. **C 19**, 164 (1979)
[3] D. Guillemaud-Mueller *et al.*, Nucl. Phys. **A 426**, 37 (1984)
[4] M. Keim *et al.*, Eur. Phys. J. **A 8**, 31 (2000)
[5] isolde.web.cern.ch
[6] U. Köster *et al.*, Nucl. Instr. Meth. **B 204**, 347 (2003)
[7] www.cern.ch/collaps
[8] P. Raghavan, At. Data Nucl. Data Tables **42**, 189 (1989)
[9] W. Itano, D. Wineland, Phys. Rev. **A 24**, 1364 (1981)
[10] G. Klotz *et al.*, Phys. Rev. **C 47**, 2502 (1993)
[11] G. Huber *et al.*, Phys. Rev. **C 18**, 2342 (1978)
[12] A. Poves *et al.*, Phys. Lett. **B 184**, 311 (1987)
[13] G. Neyens *et al.*, Phys. Rev. Lett., accepted December 2004

Eur. Phys. J. A **25**, s01, 193 – 197 (2005)
DOI: 10.1140/epjad/i2005-06-041-1

EPJ A direct
electronic only

Laser and β-NMR spectroscopy on neutron-rich magnesium isotopes

M. Kowalska[1,a], D. Yordanov[2], K. Blaum[1], D. Borremans[2], P. Himpe[2], P. Lievens[3], S. Mallion[2], R. Neugart[1], G. Neyens[2] and N. Vermeulen[2]

[1] Institut für Physik, Universität Mainz, D-55099 Mainz, Germany
[2] Instituut voor Kern- en Stralingsfysica, K.U.Leuven, B-3001 Leuven, Belgium
[3] Laboratorium voor Vaste-Stoffysica en Magnetisme, K.U.Leuven, B-3001 Leuven, Belgium

Received: 15 January 2005 / Revised version: 24 February 2005 / Published online: 3 May 2005 –

Abstract. Ground-state properties of neutron-rich ^{29,31}Mg have been recently measured at ISOLDE/CERN in the context of shell structure far from stability. By combining the results of β NMR and hyperfine-structure measurements unambiguous values of the nuclear spin and magnetic moment of ^{31}Mg are obtained. $I^{\pi} = 1/2^{+}$ and $\mu = -0.88355(15)\ \mu_N$ can be explained only by an intruder ground state with at least 2p-2h excitations, revealing the weakening of the $N = 20$ shell gap in this nucleus. This result plays an important role in the understanding of the mechanism and boundaries of the so called "island of inversion".

PACS. 21.10.Hw Spin, parity, and isobaric spin −21.10.Ky Electromagnetic moments −27.30. + t $20 \leq A \leq 38$ −32.10.Fn Fine and hyperfine structure

1 Introduction

With the advent of radioactive beam facilities the number of nuclei available for study became much larger than about 300 stable nuclei investigated before. Among the ways of gaining insight into this vast variety of nuclear systems, one is to study their ground-state properties. One of the regions of special interest is the "island of inversion", comprising highly deformed neutron-rich nuclei with 10 to 12 protons and about 20 neutrons. The large deformation in this region

[a] Conference presenter

Table 1. Ground-state properties of ^{29,31,33}Mg (before our measurements).

Isotope	Half-Life	Nuclear spin-parity
^{29}Mg	1.3 s	$3/2^+$
^{31}Mg	230 ms	$(3/2)^+$
^{33}Mg	90 ms	$(3/2)^+$

was first suggested after mass measurement of ^{31}Na [1] and has been since then observed also by other methods in some neighbouring nuclei, such as ^{30}Ne [2], ^{30}Na [3] or ^{32}Mg [2,4]. The shell model interprets this behaviour as a sign of weakening, or even disappearance of the $N = 20$ shell gap between the sd and fp shells. Due to this, particle-hole excitations come very low in energy and even become the ground state, giving rise to the inversion of classical shell-model levels, thus the name of the region. The exact borders of this "island" are not known. Odd-A neutron-rich radioactive Mg isotopes lie on its onset, or probably even inside it. Their nuclear moments are not known and only the spin of ^{29}Mg has been firmly assigned [4], and the spins of ^{31,33}Mg have been assigned tentatively [5,6] (Table 1). It is therefore important to study these systems.

2 Experimental procedure and tests

The beams of interest are produced at the ISOLDE mass separator at CERN via nuclear fragmentation reactions in the UC_2 target by a 1.4 GeV pulsed proton beam (about 3×10^{13} protons per pulse, every 2.4 seconds). They are next ionised by stepwise excitation in the resonance ionisation laser ion source [7], accelerated to 60 kV and guided to the collinear laser spectroscopy setup [8], where laser and β-NMR spectroscopy are performed (Fig. 1). The typical ion intensities available are 6.5×10^6, 1.5×10^5, and 8.9×10^3 ions/s of ^{29}Mg$^+$, ^{31}Mg$^+$ and ^{33}Mg$^+$, respectively. In the experimental setup the ions are polarised, implanted into a crystal lattice and the angular asymmetry of their β decay is detected [9].

The polarisation is obtained via optical pumping (see [3]). For this purpose the ions are overlapped with circularly polarised cw laser light and their total spins (electron and nuclear) get polarised due to the interaction with the light in presence of a weak longitudinal magnetic field. When positive laser polarisation is chosen (σ^+), after several excitation-decay cycles the ground-state sublevel with highest m_F (projection of the total atomic spin F in the direction of the guiding magnetic field) is mostly populated. For σ^- the population is highest for the lowest $m_F = -F$ (Fig. 2). The electric and nuclear spins are next rotated in a gradually increasing guiding field and adiabatically decoupled (Fig. 3) before the ions enter the region of a high transversal magnetic field (0.3 T), where they are implanted into a suitable host crystal. With polarised spins the β decay is anisotropic and the angular asymmetry of the emitted β particles

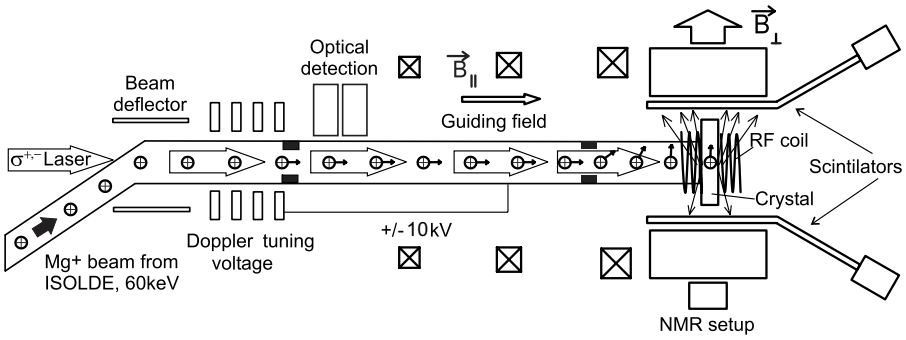

Fig. 1. Experimental setup for laser and β-NMR spectroscopy on Mg ions. For the measurements, either the optical detection or the β NMR is used.

can be measured in two detectors, placed at 0 and 180 degrees with respect to the magnetic field. The hyperfine structure of the ions can be observed in the change of this asymmetry as a function of the Doppler-tuned optical excitation frequency.

For the purpose of β-NMR measurements [9,10], the frequency is tuned to the strongest hyperfine component and the polarisation is destroyed by transitions between different nuclear Zeeman levels caused by irradiation with a tunable radio frequency. In a cubic host crystal the nuclear magnetic resonance takes place when the radio frequency corresponds to the Larmor frequency (ν_L) of the implanted nucleus. This frequency allows the determination of the nuclear g factor, since $\nu_L = \mathrm{g}\,\mu_N\,B/h$ (with B as the magnetic field). A precise g-factor measurement requires high asymmetries and narrow resonances. Both the linewidth and amplitude of the observed resonance can depend strongly on the used implantation crystal. Three cubic crystals were tested. At room temperature MgO turned out to be superior to metal hosts (it gave up to 6.7% asymmetry, compared to 3.1% for Pt and 1.8% for Au, all values taken for

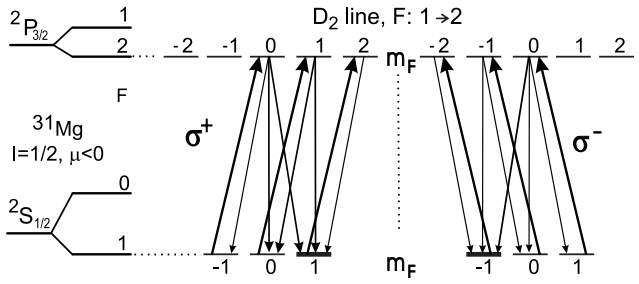

Fig. 2. Optical pumping of ^{31}Mg with an assumed spin $I = 1/2$ and a negative magnetic moment. The process is shown for $F = 1 \rightarrow F' = 2$ transitions with positive and negative laser light polarisation, which populate different m_F sublevels.

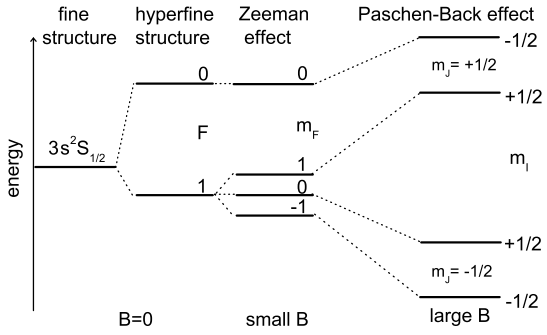

Fig. 3. Behaviour of the ground-state hyperfine structure of ^{31}Mg for weak and strong magnetic field ($I = 1/2$ and negative μ assumed).

^{31}Mg, with the linewidths comparable for all three crystals) and was therefore used for further measurements.

3 Hyperfine structure and g factor of ^{31}Mg

The transitions suitable for optical pumping of Mg ions are the excitations from the ground state to the two lowest lying excited states, $3s\ ^2S_{1/2} \rightarrow 3p\ ^2P_{1/2}$ and $3p\ ^2P_{3/2}$ (D_1 and D_2 lines). The wavelength (280 nm) is in the ultraviolet range. For better efficiency (about 5%) an external cavity was used to frequency double the 560 nm output of a ring dye laser (Pyrromethene 556 as active medium), which was in turn pumped by a multiline Ar^+ laser. The UV powers obtained in this way (about 15 mW) suffice to saturate the transitions (Fig. 4). With this setup the hyperfine structure of ^{31}Mg for both lines was recorded for σ^+ and σ^- polarised light (Fig. 5). The structures reveal 1/2 as the most probable nuclear spin, since this is the only case which can reproduce the observed three hyperfine components for both D_1 and D_2 lines, as shown in Fig. 6. For all

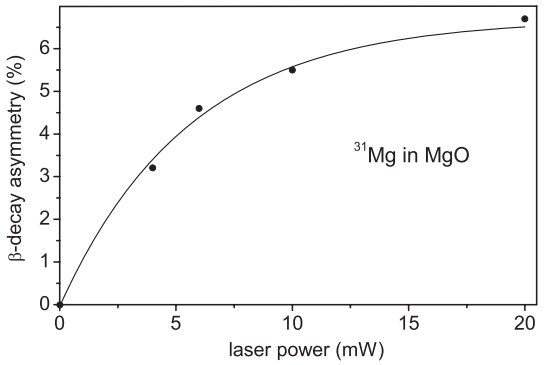

Fig. 4. β-decay asymmetry as a function of the laser power.

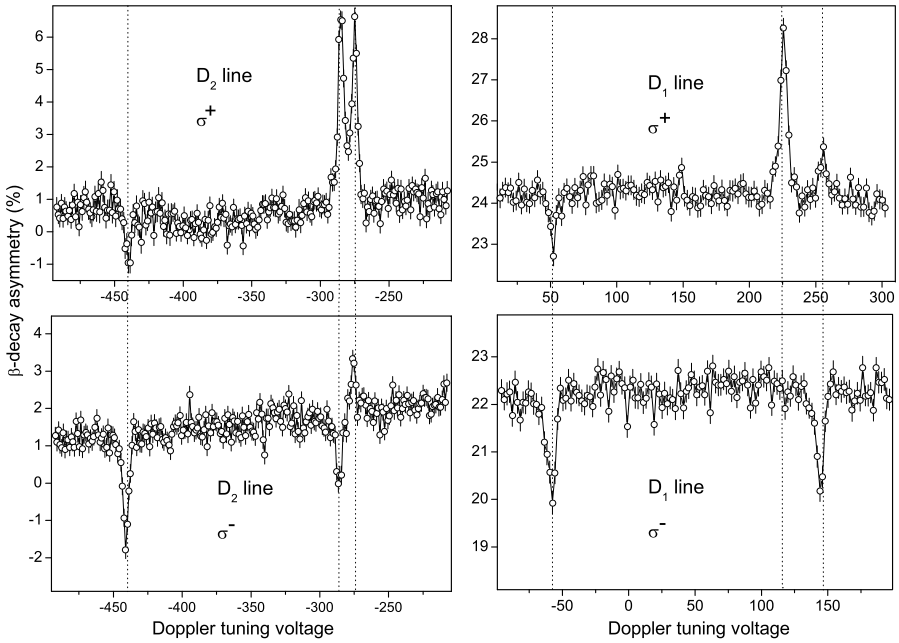

Fig. 5. Measured hyperfine structure of ^{31}Mg D_1 and D_2 lines for σ^+ and σ^- polarised light*. The experimental count rate asymmetry is shown as a function of the Doppler tuning voltage.

other spins (e.g. 3/2, 7/2) there should be 4 components in the D_1 line (fully resolved) and 6 in the D_2 line (at least partly resolved).

The positive and negative resonances in Fig. 5 reflect the sign of polarisation achieved by optical pumping on the different hyperfine-structure components for which only one example is shown in Fig. 2. For a quantitative explanation one has to take into account also the decay from the excited state to the other ground-state level (with $F = 0$ in the case of Fig. 2). The distribution of population over the different $|F, m_F\rangle$ levels can be calculated [3] by solving rate equations including the relative transition probabilities for the excitations $|F, m_F\rangle \rightarrow |F', m_F{}'\rangle$ and subsequent decays $|F', m_F{}'\rangle \rightarrow |F, m_F\rangle$. Fig. 3 shows the rearrangement of electronic and nuclear spins by the adiabatic decoupling which occurs while the ions enter the strong magnetic field region. Apparently, the effect of σ^+ and σ^- optical pumping is asymmetric in the final population of $|m_J, m_I\rangle$ levels reached in the Paschen-Back regime. Only the distribution over the nuclear Zeeman levels m_I is responsible for the β-asymmetry signals observed in the spectra. These are different in amplitude and only partly in sign under reversal of the polarization from σ^+ to σ^- light.

* There is a confusion in the original publication between $\sigma^\pm$. In Fig. 5 and everywhere in the text one must consider the opposite sign of the laser polarization.

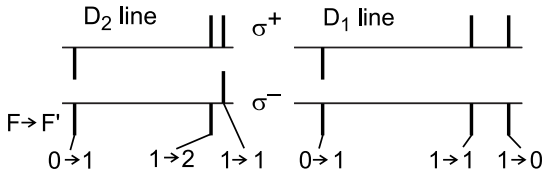

Fig. 6. Predicted hyperfine structure of ^{31}Mg D_1 and D_2 lines for $I = 1/2$ and a negative magnetic moment.

After hyperfine-structure scans, the acceleration voltage is fixed to the hyperfine component giving largest asymmetry (6.7% for D_2 line with σ^+) and β-NMR measurements follow. Several resonances in a cubic MgO lattice give the Larmor frequency $\nu_L(^{31}\mathrm{Mg})$= 3859.72(13) kHz. For the calibration of the magnetic field (within 48 hours of taking the data for ^{31}Mg) a search for Larmor resonances in the same crystal was performed on optically polarised ^{8}Li with the g factor g(^{8}Li)= 0.826780(9) [11]. This nucleus is available from the same ISOLDE target and requires changes in the optical pumping laser system (excitation wavelength around 670 nm), as well as minor modifications to the setup. The reference Larmor frequency is $\nu_L(^{8}\mathrm{Li}) = 1807.03(2)$ kHz. From the above, the deduced absolute value of the g factor of ^{31}Mg is $|g(^{31}\mathrm{Mg})|$= 1.7671(2) (corrected for diamagnetism) [12]. The final error includes a systematic uncertainty accounting for the inhomogeneities of the magnetic field and its drift between the measurements on ^{31}Mg and ^{8}Li.

4 Nuclear magnetic moment and spin of ^{31}Mg

The hyperfine splitting depends both on the nuclear spin and the g factor, *e.g.* the splitting between the ground-state hyperfine components of ^{31}Mg (the electronic spin $J = 1/2$) equals $\Delta\nu = |A|(I+1/2)$, with the hyperfine constant $A = \mathrm{g}\,\mu_N\,B_e/J$. Based on the measured g factor and the hyperfine splitting one can thus determine the spin and the absolute value of the magnetic moment ($\mu = \mathrm{g}\,I\,\mu_N$) of ^{31}Mg. A reference measurement on a different Mg isotope with a known g factor is also required, in order to calibrate for the magnetic field created by electrons at the site of the nucleus (B_e). $\Delta\nu$ can be then expressed as $\Delta\nu = (I + 1/2)\,|\mathrm{g}\,A_{\mathrm{ref}}/\mathrm{g}_{\mathrm{ref}}|$. For this purpose stable ^{25}Mg was chosen and was studied by means of classical collinear laser spectroscopy with the optical detection method (Fig. 1). To verify if our measurements are performed in the correct way, we scanned the hyperfine structure of this isotope in the D_1 line (Fig. 7). The measured hyperfine-structure constant for the ground state $A_{\mathrm{g.s.}}(^{25}\mathrm{Mg}) = -596.4(3)$ MHz is in excellent agreement with the accurate value quoted in the literature −596.254376(54) MHz [13]. This value, together with the known magnetic moment $\mu = -0.34218(3)\mu_N$ and spin $I = 5/2$ [11] of ^{25}Mg, as well as the measured value of the ground-state splitting of ^{31}Mg $\Delta\nu = 3070(50)$ MHz, reveals the spin $I = 1/2$ for ^{31}Mg. This was expected from the number of hyperfine-structure components. From the positions of the

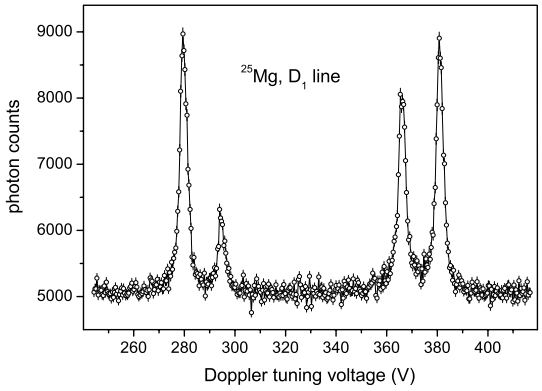

Fig. 7. Hyperfine structure of $^{25}Mg^{+}$ recorded by detecting the photons emitted during the relaxation of the ions in the optical detection part of the setup.

resonances also the sign of the magnetic moment can be deduced ($\mu < 0$). The negative value of the magnetic moment implies furthermore a positive parity of this state. It follows both from the earlier β-decay studies [5], as well as from the large scale shell-model calculations presented in Neyens *et al.* [12]. Calculations with different interactions, both in the *sd* and in the extended $sd-pf$ model spaces, predict a positive magnetic moment for the lowest $1/2^{-}$ state. Thus our observed negative sign excludes the negative parity option, in agreement with the assignment based on the β decay. Therefore we conclude that $\mu(^{31}\mathrm{Mg}) = -0.88355(10)\ \mu_N$ and $I^{\pi}(^{31}\mathrm{Mg}) = 1/2^{+}$.

Shell-model calculations in the *sd* model space using the USD interaction [14] predict the lowest $I = 1/2^{+}$ level only at 2.5 MeV excitation energy. More advanced large scale shell model calculations, including excitations of neutrons into the pf-shell, and using the interactions as described in [15] and in [16], both predict the $1/2^{+}$ level below 500 keV and with a magnetic moment close to our observed value [12]. The wave function of this $1/2^{+}$ state consists mainly of intruder configurations, which places this nucleus inside the "island of inversion".

This unambiguous spin-parity measurement allowed us also to make tentative assignments to the lowest lying excited states in ^{31}Mg [12].

Similar measurements have also been performed for ^{29}Mg. They include the nuclear g factor and the ground-state spin $I = 3/2$, which is well described in the *sd* shell model. This measurement places the ground state of ^{29}Mg outside the "island of inversion". Study of shorter-lived ^{33}Mg is planned for the future.

This work has been supported by the German Ministry for Education and Research (BMBF) under contract No. 06MZ175, by the IUAP project No. p5-07 of OSCT Belgium and by the FWO-Vlaanderen, by Grant-in-Aid for Specially Promoted Research (13002001).

References

1. C. Thibault *et al.*, Phys. Rev. C **12**, 644 (1975).
2. C. Detraz *et al.*, Phys. Rev. C **19**, 164 (1979).
3. M. Keim *et al.*, Eur. Phys. J. A **8**, 31 (2000).
4. D. Guillemaud-Mueller *et al.*, Nucl. Phys. **A426**, 37 (1984).
5. G. Klotz *et al.*, Phys. Rev. C **47**, 2502 (1993).
6. S. Nummela *et al.*, Phys. Rev. C **64**, 054313 (2001).
7. U. Köster *et al.*, Nucl. Instr. Meth. B **204**, 347 (2003).
8. R. Neugart *et al.*, Nucl. Inst. Meth. **186**, 165 (1981).
9. W. Geithner *et al.*, Phys. Rev. Lett. **83**, 3792 (1999).
10. E. Arnold *et al.*, Phys. Lett. B **197**, 311 (1987).
11. P. Raghavan, At. Data Nucl. Data Tables **42**, 189 (1989).
12. G. Neyens *et al.*, Phys. Rev. Lett. **94**, 22501 (2005).
13. W.M. Itano, D.J. Wineland, Phys. Rev. A **24**, 1364 (1981).
14. B.H. Wildenthal *et al.*, Phys. Rev. C **28**, 1343 (1983).
15. S. Nummela *et al.*, Phys. Rev. C **63**, 44316 (2001).
16. Y. Utsuno *et al.*, Phys. Rev. C **64**, 11301 (2001).